

Computational Design and Fabrication of Mechanical Metamaterials

XIAOYANG ZHENG

February 2023

Computational Design and Fabrication of Mechanical Metamaterials

XIAOYANG ZHENG

Doctoral Program in Engineering Sciences
Subprogram in Materials Science and Engineering

Submitted to the
Degree Programs in Pure and Applied Sciences of the
Graduate School of Science and Technology,
in Partial Fulfillment of the Requirements
for the Degree of Doctor of Philosophy in
Engineering

at the
University of Tsukuba

Committee Members

Name	Affiliation	Signature
Prof. Masanobu Naito (Committee chair)	University of Tsukuba, National Institute for Materials Science	
Prof. Ikumu Watanabe	University of Tsukuba, National Institute for Materials Science	
Prof. Hee Young Kim	University of Tsukuba	
Dr. Koichiro Uto	National Institute for Materials Science	

UNIVERSITY OF TSUKUBA

Abstract

Graduate School of Science and Technology

Doctor of Philosophy

Computational Design and Fabrication of Mechanical Metamaterials

by Xiaoyang ZHENG

Conventional materials possess mechanical properties dependent on their molecular or atomic composition. In contrast, mechanical metamaterials, composed of building blocks, possess properties dependent on their specific spatial arrangements. Designing the architectures paves a way for generating mechanical metamaterials with unprecedented properties, such as negative Poisson's ratio, negative mass density, negative stiffness, vanishing shear modulus, and ultra-high strength-to-density ratio. Over the last decade, extensive efforts have been paid on developing new mechanical metamaterials via designing new architectures or using new functional constitutive materials. However, some limitations are still required to address: 1) The design space is hugely limited by the design methods, that is, creating these architectures are mainly via computer-aided design (CAD) modeling, which does not guarantee optimal performances and costs a large computational resource if the geometry is too complex and elaborate. 2) mechanical metamaterials always harness zero-energy deformation modes, resulting in a fixed mechanical response after fabrication. 3) most previous design methods are forward design approach, that is, an architecture is created and its mechanical properties are investigated by experiments or simulations. This work aims to address the above-mentioned limitations.

To begin with, I propose a mathematically controlling method to simplify the conventional modeling methods. The mathematically controlling method, implemented by MATLAB codes with an implicit function, can generate a three-dimensional (3D) auxetic metamaterial with optimal performance. The 3D auxetic metamaterial was 3D printed with a rubber-like material. The compression tests, along with simulations, demonstrated that its auxetic behavior is dominated by buckling instability. A nickel layer was then plated onto the surface of 3D-printed specimens to enhance their stiffness, strength, and conductivity without loss of auxeticity and resilience. More importantly, data maps of the Young's moduli, critical buckling stresses and strains, Poisson's ratios, and conductivities provide guidance for functional applications of the material.

Further, I propose a new functionality, reprogrammability, to reprogram the mechanical responses of mechanical metamaterials. The reprogrammability was achieved by using a light-responsive shape-memory polydimethylsiloxane (SM-PDMS) that possesses shape-memory and photothermal effects. To implement the reprogrammability, I designed three different reprogrammable SM-PDMS metamaterials with different mechanical responses, namely, an auxetic SM-PDMS, a chiral SM-PDMS, and a buckling-induced SM-PDMS. Finally, a buckling-induced SM-PDMS was harnessed to make a soft actuator with a reprogrammable preferred locomotion direction. This strategy paves a way to change the mechanical responses of fabricated metamaterials. Furthermore, the designed flexible metamaterials have the potential for different applications, such as soft robots, actuation, adaptive safety, and sports equipment.

Finally, I propose a deep learning framework to convert the conventional forward design approach. The deep learning framework enables inverse design of 2D and 3D mechanical metamaterials. Based on the deep learning framework, I introduce a 2D conditional generative adversarial network (2D-CGAN) and 3D-CGAN for inversely generating 2D auxetic metamaterials and 3D architected materials, respectively, with a given target label (i.e., relative density, Young's modulus, and Poisson's ratio). The deep learning framework has potential in specific applications where architectures with desired target properties are required.

This work not only proposes novel computational design methods, architectures, and materials for mechanical metamaterials, but also has potential for specific applications. For example, catalysts made of nickel-coated auxetic metamaterials can provide dynamic catalysis; soft robots made of reprogrammable mechanical metamaterial can change their motion modes by responding to their environments (e.g., light or temperature); and scaffold implants automatically generated by CGANs can possess desired target properties for specific requirements. In addition, the inverse design approach, implemented by the deep learning framework, can be harnessed to design mechanical metamaterials with superior properties by considering architectures, constitutive materials, and the interaction to external stimulus.

Acknowledgements

I would like to express my sincere gratitude to my supervisor, Prof. Ikumu Watanabe, for his invaluable advice, kindness, and patience during my PhD study. It is his immense knowledge and continuous support that encouraged me in all the time of my academic research and daily life. I would like to thank all the members in the High Strength Materials Group in NIMS, including Prof. Takahito Ohmura, Ta-Te Chen, Viola Paul, Sachiko Taniguchi, Midori Kubota, Yuki Yamamoto, Rie Iguchi, Jiaxin Zhou, Yizhen Cao, Weikang Song, Tianwen Tan, Dayuan Liu, Fandi Akhmad, Garindra Harvianto, etc. It is their kind help, support, and companionship that have made my study and life in Tsukuba a wonderful time. I would also like to thank Dr. Koichiro Uto, Prof. Masanobu Naito, Prof. Sadaki Samitsu, Prof. Satoshi Ishii, Dr. Wei-Hsun Hu, Dr. Siqian Wang, Dr. Wei Weng, and Dr. Daiming Tang for their technical support and discussion on my study. I also appreciate all the support and understanding I received from my family and friends.

In addition, I would like to extend my sincere thanks to the financial supports of NIMS Junior fellowship, JST SPRING fellowship, and JSPS DC2 fellowship from National Institute for Materials Science (NIMS), Japan Science and Technology Agency (JST), Japan Society for the Promotion of Science (JSPS), respectively. It is these fellowships that allowed me to conduct this thesis and enjoy my life in Japan. I would like to extend my sincere thanks to Advanced Research Infrastructure for Materials and Nanotechnology in Japan (ARIM Japan) for providing me the opportunity of summer internships to Kyoto University and Cornell University.

Lastly, I would like to offer my special thanks to Japan where I have been living for unforgettable three years, for Shishitsukaoike pond where I fished crayfish and cooked them a yummy Sichuan dish, Marunuma Kogen ski resort where I learned snowboarding, Kimigahama Shiosai Park where I saw stunning sunrise, Hokkaido where I had my first kaiseki-ryōri and outdoor onsen, Nikko where I had a wonderful camping trip, Mountain Shirane where I had a 10-hour trek, Kyoto where I saw spectacular sakura and momiji, Nara where I fed super cute deers, Amabiki Kannon Temple where I saw ajisai covering on a whole pond, and Shibuya where I feasted my eyes on an array of costumes from the disturbing to the hilarious in Halloween.

Publications

This thesis is primarily based on the following publications:

- Chapter 2: **Xiaoyang Zheng**, Xiaofeng Guo, and Ikumu Watanabe. "A mathematically defined 3D auxetic metamaterial with tunable mechanical and conduction properties." *Materials & Design* 198 (2021): 109313.
- Chapter 3: **Xiaoyang Zheng**, Koichiro Uto, Wei-Hsun Hu, Ta-Te Chen, Masanobu Naito, and Ikumu Watanabe. "Reprogrammable flexible mechanical metamaterials." *Applied Materials Today* 29 (2022): 101662.
- Chapter 4: **Xiaoyang Zheng**, Ta-Te Chen, Xiaofeng Guo, Sadaki Samitsu, and Ikumu Watanabe. "Controllable inverse design of auxetic metamaterials using deep learning." *Materials & Design* 211 (2021): 110178.
Xiaoyang Zheng, Ta-Te Chen, Xiaoyu Jiang, Masanobu Naito, and Ikumu Watanabe. "Deep-learning-based inverse design of three-dimensional architected cellular materials with a target porosity and stiffness using voxelized Voronoi lattices". *Science and Technology of Advanced Materials*. 24, no. 1 (2023): 2157682.

The other works:

- Yuanjun Zhang, **Xiaoyang Zheng**, Kuan Wu, Ying Zhang, Gang Xu, Minghong Wu, Hua-Kun Liu, Shi-Xue Dou, and Chao Wu. "Nonionic Surfactant-Assisted In Situ Generation of Stable Passivation Protective Layer for Highly Stable Aqueous Zn Metal Anodes." *Nano Letters* 22, no. 21, (2022): 8574-8583.
- Ming Zhu, **Xiaoyang Zheng**, Lulu Li, Xiaolong Zhu, Zhongyi Huang, Guanyao Wang, Yuanjun Zhang et al. "Towards stable sodium metal battery with high voltage output through dual electrolyte design." *Energy Storage Materials* 48 (2022): 466–474.
- Jingjing Li, **Xiaoyang Zheng**, Jun-Li Lu, Vargas Meza Xanat, and Yoichi Ochiai. "Transformation of Plants into Polka Dot Arts: Kusama Yayoi as an Inspiration for Deep Learning." In *International Conference on Human-Computer Interaction*, pp. 270–280. Springer, Cham, 2022.
- Luonan Zhou, **Xiaoyang Zheng**, Kai Du, Xiaofeng Guo, Qiang Yin, Ai Lu, and Yong Yi. "Parametric and experiment studies of 3D auxetic lattices based on hollow shell cuboctahedron." *Smart Materials and Structures* 30, no. 2 (2021): 025042.
- Yulin Jiang, Yutao Yang, **Xiaoyang Zheng**, Yong Yi, Xianchun Chen, Yubao Li, Dan Sun, and Li Zhang. "Multifunctional load-bearing hybrid hydrogel with combined drug release and photothermal conversion functions." *NPG Asia Materials* 12, no. 1 (2020): 1-11.
- **Xiaoyang Zheng**, and Xian Zhang. "Excitons in two-dimensional materials." *Advances in Condensed-Matter and Materials Physics-Rudimentary Research to Topical Technology* (2019).

- Xiaofeng Guo, **Xiaoyang Zheng**, Yang Yang, Xinyu Yang, and Yong Yi. "Mechanical behavior of TPMS-based scaffolds: a comparison between minimal surfaces and their lattice structures." *SN Applied Sciences* 1, no. 10 (2019): 1-11.
- **Xiaoyang Zheng**, Xiaofeng Guo, Yang Yang, Zhibing Fu, Kai Du, Chaoyang Wang, and Yong Yi. "Structure-dependent analysis of nanoporous metals: clues from mechanical, conduction, and flow properties." *The Journal of Physical Chemistry C* 122, no. 29 (2018): 16803-16809.
- **Xiaoyang Zheng**, Zhibing Fu, Kai Du, Chaoyang Wang, and Yong Yi. "Minimal surface designs for porous materials: from microstructures to mechanical properties." *Journal of materials science* 53, no. 14 (2018): 10194-10208.
- Yong Yi, **Xiaoyang Zheng**, Zhibing Fu, Chaoyang Wang, Xibin Xu, and Xiulan Tan. "Multi-scale modeling for predicting the stiffness and strength of hollow-structured metal foams with structural hierarchy." *Materials* 11, no. 3 (2018): 380.
- Hao Ma, **Xiaoyang Zheng**, Xuan Luo, Yong Yi, and Fan Yang. "Simulation and analysis of mechanical properties of silica aerogels: From rationalization to prediction." *Materials* 11, no. 2 (2018): 214.
- **Xiaoyang Zheng**, Jiangshan Luo, Kai Li, Yong Yi, and Kai Du. "Simulation and Analysis of Three-Dimensional Electromagnetism, Heat Transfer, and Gas Flow for Flow-Levitation System." *IEEE Transactions on Nanotechnology* 16, no. 6 (2017): 1106-1114.

Contents

Committee Members	iii
Abstract	v
Acknowledgements	vii
Publications	ix
List of Figures	xiv
List of Tables	xv
List of Abbreviations	xvii
List of Symbols	xix
1 Introduction	1
1.1 Background of Mechanical Metamaterials	1
1.2 Design Methods	4
1.2.1 "Bottom-up" Design Strategies	4
1.2.2 "Top-down" Design Strategies	6
1.3 Fabrication Methods	7
1.3.1 3D printing	7
1.3.2 4D printing	9
1.4 Motivation and Scope	11
1.5 Outline of Thesis	11
2 Forward Design of Auxetic Metamaterials	13
2.1 Introduction	13
2.2 Materials Design Strategy by Mathematically Control	14
2.3 3D-Printed Auxetic Metamaterial	16
2.3.1 Auxetic Behavior	16
2.3.2 Influence of Relative Density	18
2.4 Metallized 3D-printed Auxetic metamaterial	20
2.4.1 Influence of Nickel Layer	20
2.4.2 Data Maps of Mechanical and Conduction Properties	23
2.5 Summary	25
2.6 Methods	25
2.6.1 Specimen Preparation	25
2.6.2 Characterization	26
2.6.3 Uniaxial Compression Tests and Current–Voltage Characteristics	26
2.6.4 Finite Element Method Simulations	27

3	Forward Design of Reprogrammable Mechanical Metamaterials	29
3.1	Introduction	29
3.2	Materials Design Strategy using Shape Memory Polymers	31
3.3	Reprogrammable Auxetic Metamaterials	36
3.4	Reprogrammable Chiral Metamaterials	39
3.5	Reprogrammable Buckling-induced Metamaterials	42
3.6	Summary	44
3.7	Methods	46
3.7.1	SM-PDMS Preparation	46
3.7.2	Mechanical Properties Investigation	47
3.7.3	Finite Element Method Simulations	47
4	Inverse Design of Mechanical Metamaterials by Deep Learning	49
4.1	Introduction	49
4.2	Materials Design Strategy by Conditional Generative Adversarial Network	51
4.3	Inverse Design of 2D Auxetic Metamaterials	53
4.3.1	Dataset Preparation	53
4.3.2	Neural Network Training	55
4.3.3	Inversely Generating 2D Auxetic Metamaterials	56
4.3.4	Validation by Experiments and Simulations	56
4.4	Inverse Design of 3D Architected Materials	58
4.4.1	Dataset Preparation	58
4.4.2	Neural Network Training	61
4.4.3	Inversely Generating 3D Architected Materials	62
4.4.4	Validation by Experiments and Simulations	64
4.5	Summary	67
4.6	Methods	67
4.6.1	Uniaxial Compression Tests	67
4.6.2	Finite Elements Method Simulations	68
5	Conclusions and Outlook	71
5.1	Conclusions	71
5.2	Outlook	72
A	MATLAB Code for Generating Auxetic Metamaterials	73
B	Buckling Analysis of a Hybrid Beam	75
C	Detail of Deep Learning Framework for 2D Auxetic Metamaterials	77
C.1	Details of 2D Conditional Generative Adversarial Network	77
C.2	Patterns Generated by 2D-CGAN	81
D	Details of Deep Learning Framework for 3D Architected Materials	83
	Bibliography	87

List of Figures

1.1	Conception of metamaterials	1
1.2	Classification of mechanical metamaterials	2
1.3	Mechanism and applications of auxetic metamaterials	3
1.4	Design methods of mechanical metamaterials	5
1.5	Typical additive manufacturing techniques and 3D-printed mechanical metamaterials	8
1.6	Comparison of representative activation mechanisms for 4D printing	10
2.1	Three common methods used to generate auxetic metamaterials	14
2.2	TPMS-based auxetic metamaterial	15
2.3	Buckling-induced auxetic behavior	16
2.4	Stress-strain curves and Poisson's ratios	17
2.5	Auxetic behavior	18
2.6	Influence of relative density on mechanical properties	19
2.7	Comparison of the proposed auxetic metamaterial with several typical auxetic metamaterials	20
2.8	Influence of nickel layer on mechanical properties	22
2.9	Influence of nickel layer on conduction properties	23
2.10	3D Contour maps of mechanical and conduction properties	24
2.11	Schematic illustrating the stress-strain and conductivity-strain curves by uniaxial compression tests	27
3.1	Reprogramming the deformation behavior of a beam using the SM effect	30
3.2	Material properties of the constituent material for mechanical metamaterials	32
3.3	Curve fitting of for SM-PDMS using the Ogden hyperelastic material model	33
3.4	DSC curves and melting and crystallization temperatures of SM-PDMS samples	33
3.5	Load-unload tensile tests of a dumbbell-type SM-PDMS sample	34
3.6	Simulation of the photothermal response of a SM-PDMS beam receiving local light	35
3.7	2D Reprogrammable auxetic metamaterial	36
3.8	Comparison between the proposed auxetic and chiral SM-PDMSs and some typical mechanical metamaterials	37
3.9	3D Reprogrammable auxetic metamaterial	38
3.10	Reprogramming a 3D auxetic metamaterial made of SM-PDMS	38
3.11	2D Reprogrammable chiral metamaterial	40
3.12	3D Reprogrammable chiral metamaterial	41
3.13	Reprogramming a 3D chiral metamaterial made of SM-PDMS	41
3.14	Reprogrammable buckling-induced metamaterial	43
3.15	Reprogramming a 2D buckling-induced metamaterial made of SM-PDMS	44
3.16	Reprogrammable buckling-induced metamaterial actuator	45

4.1	Comparison between forward design and inverse design	49
4.2	Framework of the 3D-CGAN	52
4.3	Process of structure generation for 2D auxetic metamaterials	53
4.4	Dataset of 2D auxetic metamaterials for neural network training	54
4.5	2D-CGAN architecture and training results	55
4.6	Inverse design using 2D-CGAN	57
4.7	Representative 3D-printed samples and FEM mesh for 2D auxetic meta- materials	57
4.8	Auxetic behavior of structures	58
4.9	Process of the dataset preparation for 3D architected materials	59
4.10	Assessing modeling, numerical homogenization algorithm, and FEM simulation	60
4.11	Training results of 3D-CGAN	62
4.12	Properties of 3D-CGAN-generated Voronoi lattices covering relative density– Young’s modulus relationship map	63
4.13	Computational cost and accuracy of inverse design using 3D-CGAN and forward design	63
4.14	3D-CGAN generated Voronoi lattices	65
4.15	Representative 3D-printed samples and FEM mesh for 3D architected materials	65
4.16	Deformation behavior of a 3D-CGAN generated architecture	66
B.1	Buckling analysis of a hybrid beam	76
C.1	Examples of use of circular padding and zero padding	78
C.2	Performance of the solver of 2D-CGAN	78
C.3	Patterns generated by the 2D-CGAN	81
C.4	Deformation behavior of patterns with different elastic moduli	82
D.1	Performance of the solver of 3D-CGAN	84

List of Tables

1.1	Outline of the thesis	12
4.1	Comparison of neural networks for inverse design of mechanical meta-materials	51
C.1	Neural network structure of generator for 2D-CGAN	79
C.2	Neural network structure of discriminator for 2D-CGAN	79
C.3	Neural network structure of solver for 2D-CGAN	80
D.1	Neural network structure of generator for 3D-CGAN	85
D.2	Neural network structure of discriminator for 3D-CGAN	85
D.3	Neural network structure of solver for 3D-CGAN	85

List of Abbreviations

1D	One(1)-Dimensional
2D	Two(2)-Dimensional
2PP	Two(2)-Photon Polymerization
3D	Three(3)-Dimensional
CAD	Computer-Aided Design
CGAN	Conditional Generative Adversarial Network
DIW	Direct Ink Writing
DLP	Digital Light Processing
DMA	Dynamic Mechanical Analysis
DSC	Differential Scanning Calorimetry
FDM	Fused Deposition Modeling
FEM	Finite Element Method
GAN	Generative Adversarial Network
LAPμSL	Large Area Projection Micro(μ)StereoLithography
LCE	Liquid Crystal Elastomers
MSE	Mean Squared Error
NURMS	Non-Uniform Rational Mesh Smooth
RVE	Representative Volume Element
STL	Standard Triangle Language
SLA	StereoLithography Apparatus
SLS	Selective Laser Sintering
SM	Shape-Memory
SMP	Shape-Memory Polymer
SM-PDMS	Shape-Memory PolyDiMethylSiloxane
TPMS	Triply Periodic Minimal Surface
VAE	Variational AutoEncoder

List of Symbols

c	level-set constant	
ρ	relative density (volume fraction of the solid phase)	
ϕ	porosity (volume fraction of the void phase)	
ε	strain	
ν	Poisson's ratio	
E	Young's modulus	Pa
σ	stress	Pa
t	thickness	μm
T	time	min
κ	electrical conductivities	S/m
U	voltage	V
I	electric currents	A
T_m	melting point	$^{\circ}\text{C}$
T_c	crystallization temperature	$^{\circ}\text{C}$
R_f	shape fixity of SMP	
R_r	shape recovery of SMP	
h	height	mm
w	width	mm
α	tilt angle	$^{\circ}$

Chapter 1

Introduction

1.1 Background of Mechanical Metamaterials

Conventional materials possess mechanical, electromagnetic, thermal, and optical properties that are dependent on their molecular or atomic composition. These overall properties of conventional materials are usually tailored by engineering their composition. Taking structural materials as an example, the Iron Age had been booming for hundreds of years since iron tools and weapons gradually replaced their bronze equivalents in common use. These iron tools and weapons were smithed primarily from wrought iron that is brittle. However, by controlling the level of carbon (between 0.0 and 1.7% carbon), wrought iron can be transformed into steel that is ductile, stiff, and strong, which can replace woods and ceramics in building structures.

In contrast, metamaterials, composed of building blocks (a “meta” cell), possess properties that are dependent on their specific spatial arrangements [1, 2]. The prefix “meta” comes from ancient Greeks and means “beyond,” “after,” or “behind”, which refers to the superiority that metamaterials can surpass their constituent materials and achieving unprecedented properties by carefully structuring the building blocks. Consequently, metamaterials are sometimes called architected materials as they possess architecture-dependent properties. Actually, any conventional material can be spatially arranged into a building block that is then assembled periodically into a metamaterial (Figure 1.1).

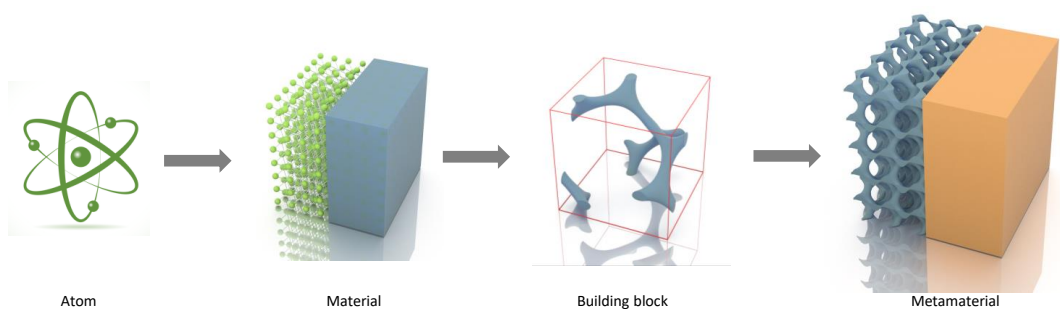


FIGURE 1.1: Conception of metamaterials: Conventional materials are composed of atoms; conventional materials can be geometrically architected into a building block, which can be rationally designed beyond the restrictions of conventional materials; multiple building blocks can be periodically assembled into a metamaterial.

Over the past several decades, metamaterials are purposely designed with unique architectures to produce properties that are not found in naturally occurring materials, including electromagnetic [3], photonic [4], acoustic [5], thermal [6], and mechanical metamaterials [7–9]. Particularly, mechanical metamaterials have drawn widespread

attention owing to the potential to obtain unprecedented properties, such as extraordinary or extreme elasticity tensors and mass-density tensors [10]. Typical mechanical metamaterials include auxetic metamaterials with negative Poisson's ratios [11, 12], light-weight lattices with ultra-high strength-to-density ratios [13–15], metamaterials with negative mass densities and negative elastic moduli [16–18], pentamode metamaterials with near zero shear moduli [19, 20], and deployable origami structures [21, 22], as shown in Figure 1.2.

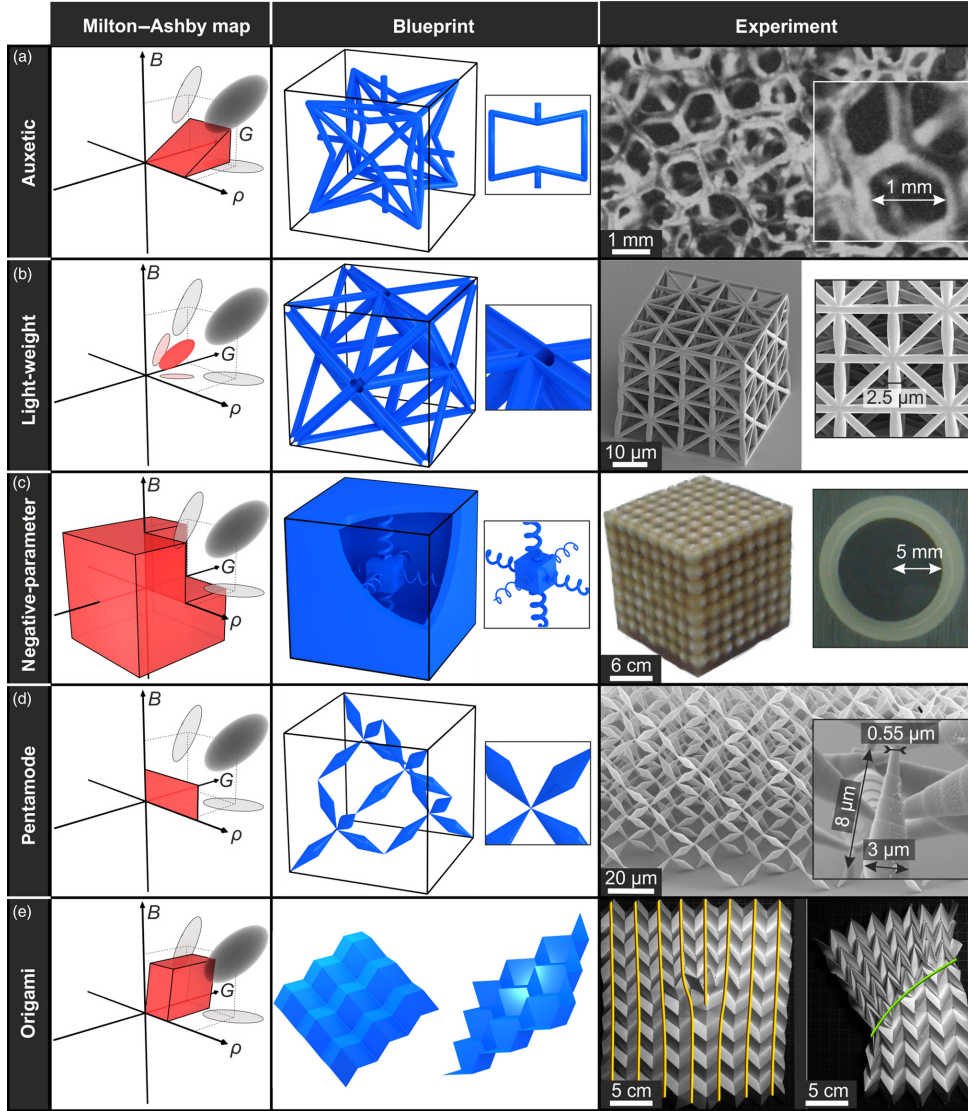


FIGURE 1.2: Classification of mechanical metamaterials: (a) auxetic, (b) light-weight, (c) negative-parameter, (d) pentamode, and (e) Origami mechanical metamaterials. The left column, Milton-Ashby map, compares the elasticity tensors and mass-density tensors of mechanical metamaterials (red) and conventional materials (gray). The center column shows the blueprints of typical mechanical metamaterials with highlights of their geometric features. The right column shows the micrographs of typical fabricated mechanical metamaterials. [10]

The design space of mechanical metamaterials paves a way to achieve unprecedented properties, making them potential candidates in specific applications. Taking auxetic metamaterials as an example, they possess negative Poisson's ratios, whereas

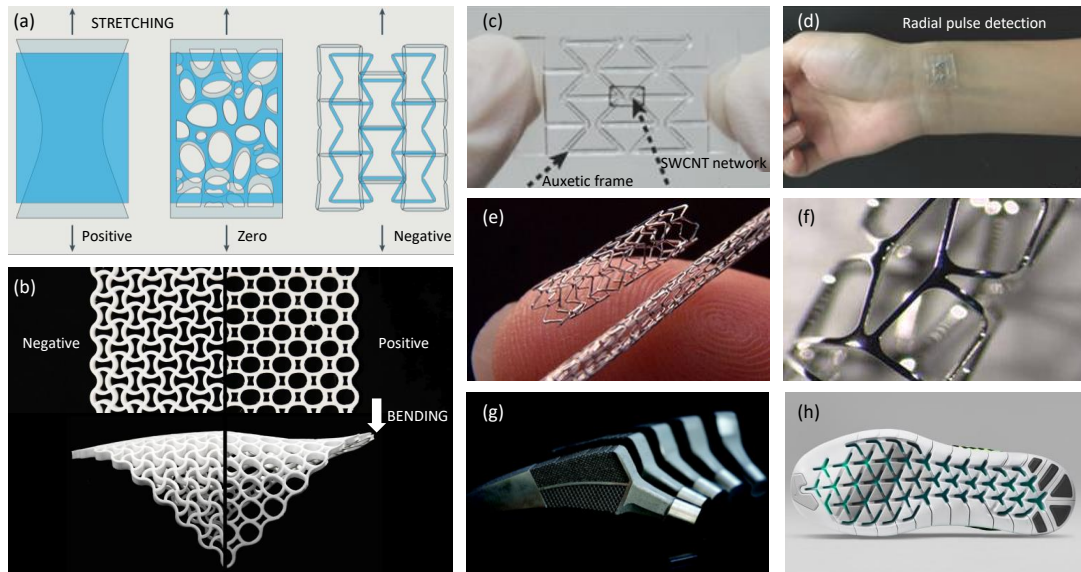


FIGURE 1.3: Mechanism and applications of auxetic metamaterials (negative Poisson's ratio materials). (a) Comparison in stretching load: applying a uniaxial stretch results in a lateral expansion in negative Poisson's ratio materials, but a lateral contraction in positive Poisson's ratio materials and no lateral deformation in zero Poisson's ratio material [8]. (b) Comparison in bending load: under a bending load, a plate with a negative Poisson's ratio material deforms into a convex shape, whereas a plate made of a positive Poisson's ratio material deforms into a saddle shape [23]. (c,d) Stretchable strain sensor cooperated with 2D auxetic structures [24]. (e,f) Coronary stent constructed by auxetic structures [25]. (g) Hybrid implant composed of negative and positive Poisson's ratio structures [26]. (h) Nike flyknit shoe with an auxetic sole.

common polymers and polycrystalline metals possess Poisson's ratios in the range of 0.25–0.35 generally. When auxetic metamaterials are uniaxially stretched, they expand in all directions, whereas common structural materials shrink in a direction perpendicular to the applied load (Figure 1.3a). Further, when bent, a plate made of an auxetic metamaterial deforms into a convex shape, whereas a plate made of a material with a positive Poisson's ratio deforms into a saddle shape (Figure 1.3b). The compression–shrinkage or tension–expansion synclastic behaviors make them promising candidates in energy adsorption [27, 28], strain sensors [24, 29], biomedicine [25, 26, 30], actuation [31, 32], sports [33–35], etc. For example, the sensitivity of stretchable strain sensors can be significantly enhanced by incorporating two-dimensional (2D) auxetic metamaterials owing to the synergistic effect of reduced geometric Poisson's ratio and strain concentration (Figures 1.3c and d) [24]. In biomedicine applications, a coronary stent is tiny wire mesh tube used support the inner wall of veins and arteries; constructing a stent with auxetic metamaterials can alleviate foreshortening effects and provide good mechanical adhesion with the arterial wall (Figures 1.3e and f) [25]. In addition, implants composed of negative and positive Poisson's ratio structures are demonstrated to improve implant–bone contact in off-axially loads (Figure 1.3g) [26]. Furthermore, taking the advantage of anomalous ability of bending-to-dome, auxetic metamaterials are also used in sportswear. This can be seen in certain Nike flyknit shoes, whose soles are made of auxetic structures to enhance the running experience

(Figure 1.3h).

Owing to their potentials in such kinds of applications, considerable efforts have been devoted to design and fabricate mechanical metamaterials. Particularly, recent advances in deep learning and additive manufacturing have opened new avenues for designing and fabricating such complicated structures, and thus promoted the unrestrained creativity in mechanical metamaterials [36–38]. The ultimate goal of this research is to develop more effective and advanced design methods for fabricating mechanical metamaterials with better performance and novel functionalities.

1.2 Design Methods

To reduce the designing complexity, mechanical metamaterials are mostly designed based on a single building block that can be periodically assembled in a nearly infinite space. After designing a building block of mechanical metamaterial, its effective mechanical properties can be investigated by either finite element method (FEM) simulations or mechanical testing. In FEM simulations, the effective properties are always investigated using a single building block with periodic conditions. Typical FEM algorithms include homogenization algorithms for calculating elastic moduli (e.g., Young's modulus, Poisson's ratio, and shear modulus) [39–42], and uniaxial compression/tension, three-point bending, and isotropic compression simulations for investigating large deformation behaviors [43–46]. The constitutive material models for FEM simulations can be either linear elastic materials or nonlinear materials with specific functions, such as hyperelastic models [11, 47], strain-rate dependent models [48], and even optical [49], magnetic [50–52], or thermal [53] responsive models. In mechanical testing, the effective properties are always investigated using 3D printed specimens composed of multiple unit cells of building blocks (always over $3 \times 3 \times 3$ unit cells) [44, 47, 54]. In addition to the approaches for investigating large deformation behaviors in FEM simulations, fatigue testing and impacting testing are also conducted in experiments for probing the fatigue resistance and energy adsorption abilities [55, 56]. The deformation behaviors of mechanical metamaterials are always *in situ* captured by high-speed cameras to analyze mechanical responses and properties (e.g., buckling, twisting, and Poisson's ratio). Mechanical testing is also an effective way for validating FEM simulation results.

The above-mentioned process is called forward-design approach: first, a structure is created, and its mechanical properties are then investigated by FEM simulations or mechanical testing. To achieve unprecedented properties, the geometric arrangement of mechanical metamaterials is always delicately designed by the experienced designers with trial-and-error method. The modeling methods can be divided into "bottom-up" and "top-down" design strategies, depending on how a structure is created. In "bottom-up" design strategies, the modeling process is an "addition operation" in which basic geometric elements are assembled into a scaffold structure, akin to constructing objects with Lego bricks. In "top-down" design strategies, the modeling process is a "subtraction operation" in which a domain (usually a square or cube) is hollowed out purposely into a cellular structure, akin to the construction of termite nests.

1.2.1 "Bottom-up" Design Strategies

Computer-aided design (CAD) modeling and Voronoi tessellation are typical "bottom-up" design strategies for constructing regular and irregular mechanical metamaterials,

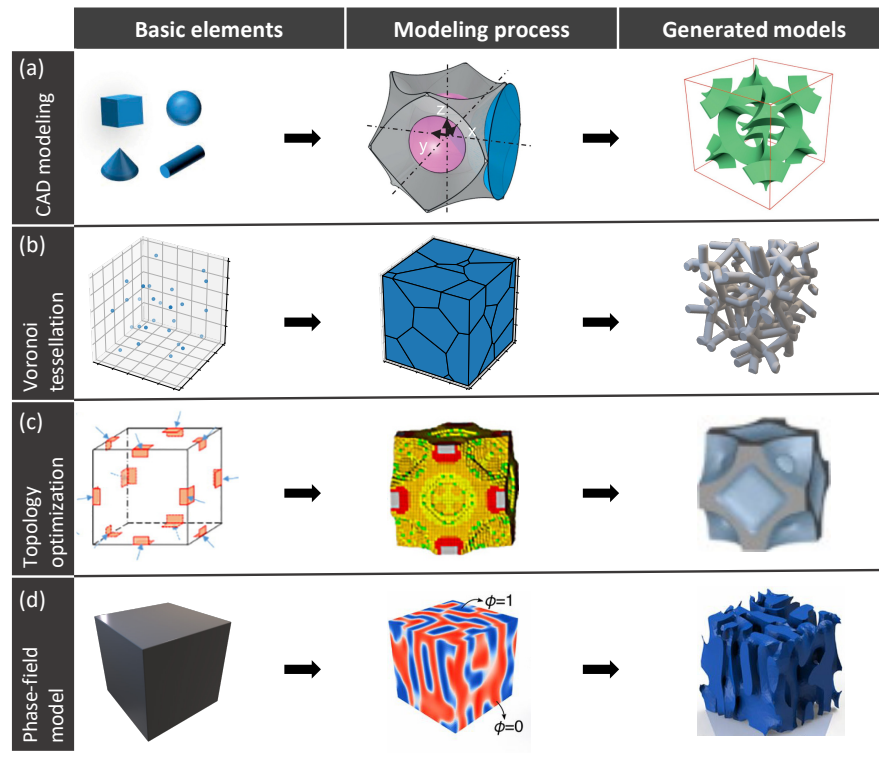


FIGURE 1.4: Design methods of mechanical metamaterials. (a) CAD modeling where a geometry is built by Boolean operations of simple geometries. (b) Voronoi tessellation where a geometry is built by extracting features (edges or faces) of a Voronoi diagram. (c) Topology optimization where a geometry is built by optimally removing redundant material for a given structure [57]. (d) Phase-field model where a geometry is built by simulating phase separation process [58].

respectively. CAD modeling is more empirical and always used to construct regular geometries in an ordered manner, whereas Voronoi tessellation is usually used to construct stochastic open- or closed-cell foams by applying Voronoi diagram using a seed (i.e., finite points) in a 2D Euclidean plane or 3D Euclidean space [59].

In CAD modeling, the geometric elements of building blocks are mainly simple geometries, such as 1D lines and curves, 2D circles, rectangles, and polygons, and 3D cubes, beams, and spheres (Figure 1.4). These simple geometries can be designed and constructed into different geometric motifs, depending on the imagination and experiences of designers or taking inspiration from glorious creatures, crystalline solids, and arts and crafts. A geometry of a building block is yielded after constructing these simple geometries via CAD modeling, such as Boolean and lofting operations. CAD modeling is always implemented in CAD design and drafting software applications with graphical user interface. Popular CAD applications include AutoCAD (Autodesk, USA), Autodesk 3ds Max (Autodesk, USA), SolidWorks (Dassault Systèmes, France), and Rhinoceros 3D (Robert McNeil & Friends, USA) with its third-party component Grasshopper. In addition, FEM software applications, such as Abaqus FEA (Dassault Systemes, France), ANSYS (Canonsburg, USA), and COMSOL Multiphysics (COMSOL, Sweden), also provide a seamless process for constructing and simulating mechanical metamaterials simultaneously. Most mechanical metamaterials are created by CAD modeling, such as auxetic metamaterials with re-entrant, chiral, rotating structures [11, 12, 24, 27, 30], light-weight lattices with bending- or stretching-dominated

behaviors [14, 15], and structured fabrics with interlocking particles [46]. However, the CAD modeling can be time-consuming and cost a huge computing resource if the geometry is too complicated.

In Voronoi tessellation, the geometric elements of created building blocks are beams or shells, depending on whether an open- or closed-cell foam is generated. The general modeling process of Voronoi tessellation follows as below: a seed consisting of finite coordinate points is initially created, followed by building a Voronoi diagram using the seed; in 2D case, a lattice is generated by applying a thickness to the edges of each polygons in the Voronoi diagram [60–62]; in 3D case, an open-cell foam is generated by applying a thickness to the edges of each polygons, and a closed-cell foam is generated by applying a thickness to the faces of each polygons [63–68]. The geometry generated by Voronoi tessellation can be either regular and irregular, depending on the regularity of the seed. The Voronoi tessellation is always implemented by computer scripts due to its complexity, such as Python [68], C++ [64, 65], MATLAB (MathWorks, USA) [60], as well as build-in modules in some CAD applications [63, 66, 67]. Consequently, the scripts enables rapidly generating a large number of geometries for the datasets of deep learning.

1.2.2 "Top-down" Design Strategies

Topology optimization and phase field are symbolic "top-down" design strategies for constructing mechanical metamaterials with optimal performance. Topology optimization is used for developing optimized structures with desired target properties by considering design parameters such as expected loads, volume fractions, and available design space. In contrast, phase-field model is used for developing structures with smooth surfaces by simulating interactions between different phases.

In topology optimization, the material layout is generally evaluated by FEM with the goal of maximizing the performance. The material layout is optimized using either gradient-based algorithms (e.g., optimality criteria algorithm) or non gradient-based algorithms (genetic algorithm). Topology optimization can be implemented by either homemade scripts or in build-in modules in FEM applications [57, 69–73]. In particular, topology optimization is capable of generating mechanical metamaterials with desired target properties, such as negative Poisson's ratio [70, 71, 73] and Hashin-Shtrikman upper bounds on isotropic elasticity [72, 74]. As different geometric patterns with similar properties can be automatically created by changing boundary conditions, topology optimization is also an effective way to make datasets for deep learning [72]. However, generating geometries is time-consuming especially for the generation of 3D geometries.

In phase-field model, the material layout is optimized by reproducing a given interfacial dynamics to simulate and predict complex microstructure developments [75]. A typical application of phase field in mechanical metamaterials is spinodal decomposition, which can generate topologies with smooth surfaces [76]. Spinodal decomposition generates spinodal topologies by simulating diffusion-driven process of a homogeneous solution that decomposes into two spatially separated uniform phases. Spinodal topologies are composed of smooth, non-intersecting surfaces, which can alleviate stress concentration [58, 77–79]. According to the post-processing way, spinodal topologies can consist of either ligaments (i.e., solid networks formed by removing one phase) or surfaces (i.e., shell networks formed by keeping only the interfaces of two phases). Compared with its analogue, triply periodic minimal surfaces (TPMSs) [44, 54], spinodal topologies can be realized as disordered, non-periodic, and

anisotropic architectures, a diversity that makes them a potential candidate for making big datasets [80]. However, generating spinodal topologies is time-consuming as it costs hours for simulating the phase separation process based on Cahn–Hilliard equation on a normal computer [77, 78].

1.3 Fabrication Methods

After computationally designing mechanical metamaterials, the most straightforward way to fabricate them is additive manufacturing [81–84]. Although some fabrication methods, such as laser cutting and wire weaving [21, 85–88], have been developed to fabricate mechanical metamaterials, the feasible structures are highly limited. For instance, laser cutting is always used to fabricate 2D mechanical metamaterials [21, 85, 86]. In addition, auxetic metamaterials manufactured by forming helical wires can achieve high energy absorption and fracture resistance capabilities; however, their basic geometries are mainly 3D truss-like cells, which do not allow fabricating complex internal shapes [87].

Additive manufacturing, including 3D printing and 4D printing, refers to the manufacturing process of creating objects by adding materials using a 3D printer and CAD software. Four-dimensional (4D) printing involves the same techniques of 3D printing, but the created 3D shape is capable of morphing into different forms in response to environmental stimulus by taking advantage of stimulus-responsive materials [89–91]. Additive manufacturing is in stark contrast to conventional manufacturing processes where a block of material or a mold is required to manufacture physical objects. Compared with conventional manufacturing processes, additive manufacturing is faster, more efficient, and capable of creating more complex geometries with an ever-expanding list of materials. In additive manufacturing, a mechanical metamaterial is firstly computationally designed and generated, and then exported as a standard triangle language (STL) file for printing. The STL file is sliced by a slicing software before sent to a 3D printer. After printing, a 3D printed specimen is finished after post processing (e.g., washing, curing, and removing supports).

1.3.1 3D printing

Since the inception of 3D printing, different additive manufacturing techniques have been introduced to manufacture mechanical metamaterials. Typical additive manufacturing techniques are listed in Figure 1.5. The minimum feature size of 3D-printed models and the type of printable materials are determined by the specific patterning and solidification process in different additive manufacturing techniques. Figure 1.5 also compares the minimum feature sizes and typical mechanical metamaterials printed using different additive manufacturing techniques. Recent advances in additive manufacturing have hugely improved the printing resolution and speed [95–98], and developed new printable materials [94, 99].

When talking about 3D printing, what firstly comes to your mind might be desktop 3D printers printing colorful toys using polymer-based filaments. These desktop 3D printers are based on fused deposition modeling (FDM) in which filaments are melted and extruded through a nozzle and fused together to create 3D objects (Figure 1.5a) [100–102]. Speaking of cost, FDM 3D printers and regular FDM filaments are by far the cheapest 3D printer and printing material, respectively. Therefore, FDM 3D printers are commonly used in schools and universities for teaching 3D printing. However,

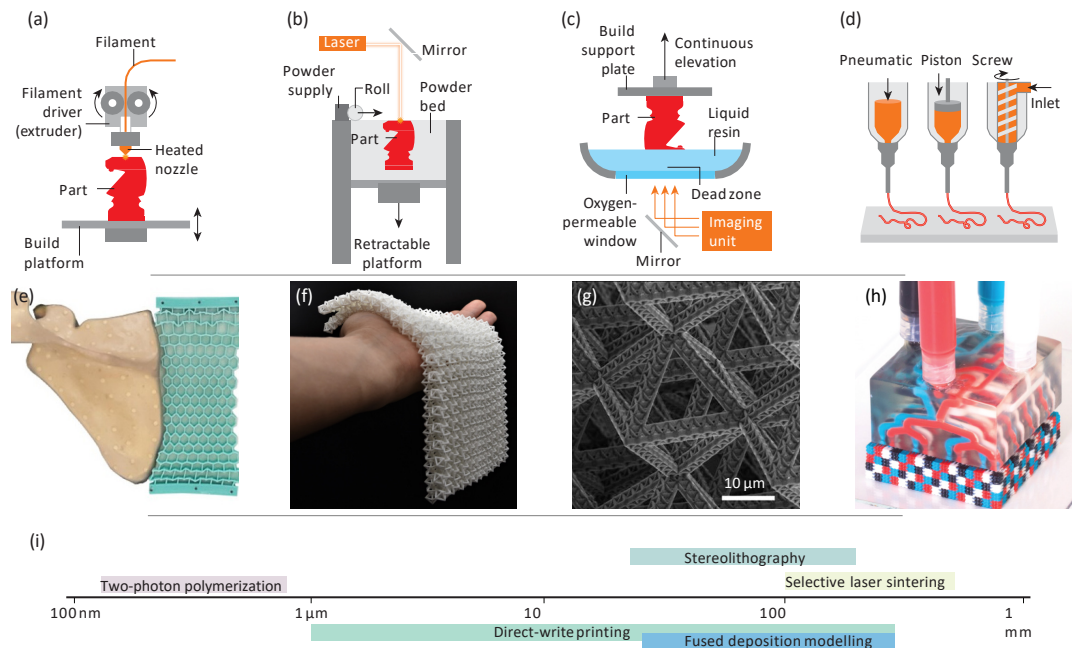


FIGURE 1.5: (a–d) Typical additive manufacturing techniques and 3D-printed mechanical metamaterials: (a) fused deposition modeling; (b) selective laser sintering; (c) resin printing (e.g., stereolithography and two-photon polymerization); (d) direct-write printing [84]. (e–h) 3D-printed mechanical metamaterials fabricated by: (e) fused deposition modeling [92], (f) selective laser sintering [46], (g) two-photon polymerization [93], and (h) direct-write printing [94]. (i) Minimum size ranges of patterned features produced by different additive manufacturing techniques [84].

as the standard nozzle size is 0.4 mm, the feature size is hugely limited. Also, additional supports are required if a geometry is too complex. As a consequence, FDM is always used to fabricate 2D mechanical metamaterials for validating their mechanical properties (Figure 1.5e) [92, 103].

To avoid additional supports, powder bed fusion 3D printing, such as selective laser sintering (SLS), is a suitable option [27, 47, 104]. In SLS, powdered materials are locally heated and sintered using a laser in a powder bed to create objects (Figure 1.5b). The quality of printed objects is highly dependent on the powder properties such as particle size and shape. To facilitate spreading, granulated powders are typical range from 10 to 100 μm in Gaussian distribution, which restricts the minimum feature size of printed objects (around 100 μm). However, the non-fused powders in the powder bed serve as supports during printing process, enabling fabricating complex architectures without additionally interior supports (Figure 1.5f) [46, 47, 104].

To improve the feature size and surface finish, resin printing is one of the most commonly used additive manufacturing techniques for fabricating mechanical metamaterials (Figure 1.5c). In resin printing, 3D objects are created by successively printing thin sliced layers using a liquid resin selectively photopolymerized by ultraviolet light. The first resin printing technique is stereolithography (SLA) 3D printing invented by Hideo Kodama in the early 1980s [105]. A desktop SLA 3D printer contains a build platform and a resin tank which serves as a container for the liquid resin to cure. SLA offers a variety of printable materials and fine surface finish, and thus

serves as a popular technique for fabricating mechanical metamaterials [44, 62]. Digital light processing (DLP) 3D printing is another common processes for resin 3D printing [14, 106]. DLP and SLA share the basic concept of printing process, but depends on different light sources—SLA a laser and DLP a projector. Thereafter, SLA relies on point-source illumination whereas DLP relies on face-source illumination, making DLP faster than SLA. In addition, another resin printing technique, two-photon polymerization (2PP), provides the highest printing resolution by utilizing two-photon absorption of near infrared light to excite the same energy transition as ultraviolet photons, making it possible to print complex hierarchical architectures (Figure 1.5g) [15, 93, 107]. However, there is an inherent trade-off between feature size, building volume, and printing speed. This means that 2PP can be used to fabricate highly complex microarchitectures, but limited within a building volume of 1 cm³. The limitation can be broken by developing new additive manufacturing technique. For example, a hierarchical metamaterial with dimension of hundreds of millimetres and feature size of sub-10 μm can be fabricated using a large-area, high-resolution additive manufacturing technique [106]. The additive manufacturing technique combines Large Area Projection Microstereolithography (LAPμSL) and an addressable spatial light modulator to print microarchitectures over a substantially larger area.

Although resin printing provides the highest feature resolution, the available materials are limited with photopolymerizable resins. In contrast, direct-write printing techniques, such as direct ink writing (DIW), can pattern myriad materials in the form of printable inks derived from a wide range of molecular, polymeric or particulate species under ambient conditions (Figure 1.5d) [94, 98, 99, 108]. Inks for this technique are composed of low-viscosity fluids, including concentrated polymer, fugitive organic, filled epoxy inks, and metallic particles, providing a wider range of printable materials than other methods. In addition, by using multiple printheads, objects can be printed with multiple materials (Figure 1.5h) [94].

1.3.2 4D printing

Unlike 3D printing that creates object with fixed shape after fabrication, 4D printing allows the printed objects to transform with response to external stimuli, earning its 4th dimension. According to stimulus-responsive materials, 4D-printed objects can possess different activation mechanisms such as heat transfer, chemo-mechanical transformation, and electromagnetic interactions [2, 89–91], as shown in Figure 1.6. Mechanical metamaterials made of thermo- and chemo- responsive materials are triggered by surrounding temperature or chemical cues [109–114]. For example, lightweight mechanical metamaterials printed using thermo-responsive shape-memory polymer (SMP) can be deformed substantially and mechanically programmed into an arbitrary geometry after receiving thermal stimulation, and recover to the original shape after further thermal stimulation [109]. Mechanical metamaterials made of electromagnetically responsive materials can respond in a short time remotely manipulated by a magnetic field, an electric field or light [50–52, 115, 116]. The remote manipulation enables mechanical metamaterials to perform remotely prescribed tasks such as delivering an object [116]. The versatile functional responsive materials, combined with delicate architectural design, provide great degree of freedom to achieve desired spatiotemporal responses.

In addition to common polymers and metals, functional responsive materials are always used for 4D printing, such as polymer-filler composites, liquid crystal elastomers (LCEs), SMPs, hydrogels, and polymers with embedded magnetic, piezoelectric, and light-absorbing particles. Among them, SMPs have attracted most attention


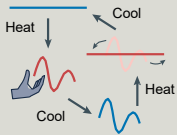
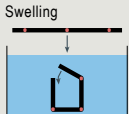
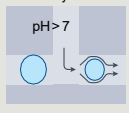
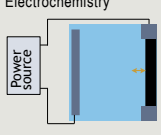
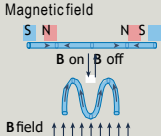

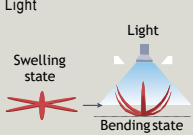
Activation mechanism	Typical materials	Fabrication methods	Response speed	Advantages	Limitations
<p>Heat transfer</p> <p>Phasechange</p>  <p>LC domain alignment 1</p> <p>LC domain alignment 2</p> <p>$T < T_{NI}$ $T > T_{NI}$</p> <p>Shapememory</p>  <p>Heat Cool</p> <p>Cool Heat</p>	Polymers, metals, polymer-filler composites, LCEs, SMPs, hydrogels	DIW, DLP, TPL, microfabrication, machining	Slow to medium	Remote activation by temperature; thermal expansion is universal and can be modelled systematically; phase-changing materials have substantial thermal expandability and programmable anisotropy; SMPs can be willfully deformed after fabrication and achieve nearly full shaperecovery	Limited to specific temperatures and environments (for example, cannot operate when temperature cannot be changed); may require large temperature change and long heating or cooling time
<p>Chemo-mechanical transformation</p> <p>Swelling</p>  <p>Chemistry</p>  <p>pH > 7</p> <p>Electrochemistry</p>  <p>Power source</p>	Hydrogels, hydrogel-filler composites, polymers, multi-material composites	DIW, DLP, microfabrication, machining	Slow to medium	Large, programmable structural changes; easy activation by wetting	Transformation speed limited by mass transport; require large environmental changes
	Hydrogels	DLP, 2PP, microfabrication, machining	Medium to fast	Chemical activation is useful for biomedical applications; autonomous feedback can be achieved via chemical reactions	Require specific reactions and relevant materials synthesis to respond to different chemical cues
	Electrochemically active materials (such as conjugated polymers, battery electrode materials)	Machining, microfabrication, 2PP	Slow to medium	Structure and property retention upon stimulus removal; continuous control of transformation; potential to simultaneously store energy	Typically require two electrodes, a liquid or gel electrolyte, and a power source; 3D structuring methods are not fully developed
<p>Electromagnetic interactions</p> <p>Magnetic field</p>  <p>S N N S</p> <p>B on B off</p> <p>B field</p> <p>Electric field</p>  <p>V on V off</p> <p>Light</p>  <p>Swelling state</p> <p>Bending state</p> <p>Light</p>	Polymers with embedded magnetic particles	DIW, 2PP, microfabrication	Fast	Fast, remote activation (typically <1s); complex, reversible, and programmable structural changes	Require strong magnetic fields (typically >0.1 T); mostly soft materials
	Ionic hydrogels, dielectric elastomers, piezoelectric composites	DLP, moulding, machining, microfabrication	Medium to fast	Dielectric elastomers integrate into electronic control circuits for autonomous devices; piezoelectric materials can measure strain	Require additional electrodes and electronic control
	Polymers with light-absorbing nanoparticles, azobenzene-containing liquid crystal polymers	DIW, microfabrication, machining	Medium to fast	Fast, remote activation and active manipulation; independent control of shape changes by different polarizations and wavelengths	Limited 3D patterning methods; cannot function without a light source and sufficient transmission

FIGURE 1.6: Comparison of representative activation mechanisms for 4D printing [2].

because they can be programmed into a temporary shape and return to their initial shape by external stimuli, such as light, heat, magnetism, and electricity [109, 110, 112–114]. The programmed temporary shape enables mechanical metamaterials to change or switch their mechanical responses. In general, SMPs are crystalline and semicrystalline polymers whose shape memory behavior is determined by the transition temperature (e.g., melting temperature, T_m , or crystallization temperature, T_c). When heated over the transition temperature, the crystalline part softens and becomes easy to manipulate. The deformed shape can be kept after cooling down to the transition temperature. However, mechanical metamaterials made of SMPs hardly undergo large deformations due to the plasticity of SMPs at room temperature (below the transition temperature) [109, 110, 117–119].

1.4 Motivation and Scope

From the brief introduction of the background of mechanical metamaterials, the research of mechanical metamaterials is still in its infancy. Current efforts have been paid on developing new mechanical metamaterials by designing new architectures or using new functional constitutive materials. Some limitations are still required to address.

First, the design space is hugely limited by the design methods. For example, auxetic metamaterials are typically classified into re-entrant, chiral, rotating, and hierarchical laminate structures according to their deformation mechanisms. Creating these geometries are mainly by CAD modeling, which does not guarantee optimal performances and costs a large computational resource if the geometry is too complex.

Second, mechanical metamaterials always harness zero-energy deformation modes, i.e., a single shape change that limits their applications, resulting in the need for changeable mechanical responses. This means that the mechanical responses of mechanical metamaterials are fixed after fabrication. For example, an auxetic metamaterial always shrinks laterally under a uniaxially compressive load.

Last and most importantly, most previous design methods are forward design approach: first, a structure is created, and its mechanical properties are then investigated by FEM simulations or mechanical testing. The mechanical properties of the designed materials are known only after time-consuming simulations or experiments. In addition, the realization of the geometric arrangements of mechanical metamaterials are highly dependent on the prior knowledge of experienced designers, resulting in a limited number of design spaces. What if we could convert this conventional forward design approach? Could we harness an inverse design approach where an architecture with desired target properties could be automatically generated by a computer?

This work focuses on harnessing state-of-the-art computational methods and functional materials to address the above-mentioned three limitations.

1.5 Outline of Thesis

The main body of the thesis consists of three chapters that correspond to the above-mentioned three limitations (Table 1.1).

TABLE 1.1: Outline of the thesis.

Chapter	Chapter 2	Chapter 3	Chapter 4
Purpose	Simplify the conventional modeling methods	Reprogram the mechanical responses	Convert the conventional forward design approach
Method	Develop a modeling method by mathematically control	Develop a new shape memory polymer	Develop a deep learning framework
Results	Design a 3D auxetic metamaterial generated by MATLAB codes using implicit function	Design three mechanical metamaterials whose mechanical responses can be switched using light stimulation	Inversely generate 2D and 3D mechanical metamaterials
Others	Enhance the stiffness, strength, and conductivity of the auxetic metamaterial using nickel plating	Fabricate a soft actuator that shows reprogrammable preferred locomotion direction	Create the datasets of mechanical metamaterials using Voronoi tessellation

Chapter 2

Forward Design of Auxetic Metamaterials by Mathematically Control

2.1 Introduction

In this chapter, I manage to simplify the conventional modeling methods by proposing a mathematically modeling method. The proposed modeling method generates an new 3D mechanical metamaterial by using implicit functions with MATLAB codes.

An auxetic metamaterial is a type of mechanical metamaterial that has a negative Poisson's ratio. Most auxetic metamaterials are truss-based or originate from Boolean operations of simple geometries. Auxetic metamaterials are typically classified into re-entrant [120–126], chiral [127–131], rotating [11, 87, 132–135], and hierarchical laminate structures [136–138] according to their deformation mechanisms. In general, the re-entrant, chiral, and rotating structures are porous and composed of a single component, whereas the hierarchical laminate structures are solid and consist of two or more components with different Poisson's ratios. The empty spaces in the interior structures of these materials are necessary for rotation, bending, and torsion of the ligaments and nodes in the former three analogies, resulting in low stiffnesses and strengths compared with their matrix materials. Most auxetic metamaterials have periodic array structures according to their design principles in terms of the components, porosities, and periodicities. These basic arrays generally comprise beams, trusses, or shells, or are generated from Boolean operations of simple geometries, such as cylinders, cones, spheres, and boxes (Figure 2.1). The modeling method greatly limits its applications, especially where optimal performances are needed.

However, TPMSs, which are a type of metamaterial, have recently gained much attention owing to their mathematically controlled and fascinating topologies [139, 140], such as their bioinspired morphology, smooth surfaces without edges and corners [141], and higher stiffness and strength than their disordered counterparts [63]. Extensive efforts have been invested to expand the design spaces of TPMS-based materials, such as skeletal, sheet, graded, and hybrid lattice structures [44, 54, 142–144]; however, thus far, only a few studies have focused on achieving negative Poisson's ratios [145, 146]. Herein, I extend the application of TPMSs to auxetic metamaterials by exploiting their particular characteristics.

3D printing or additive manufacturing is a standard method used to fabricate delicately designed auxetic metamaterials. Rubber-like materials, such as flexible resins and thermoplastic polyurethane, are the typical raw materials used for 3D-printed auxetic metamaterials, which render them resilient but result in inadequate stiffness

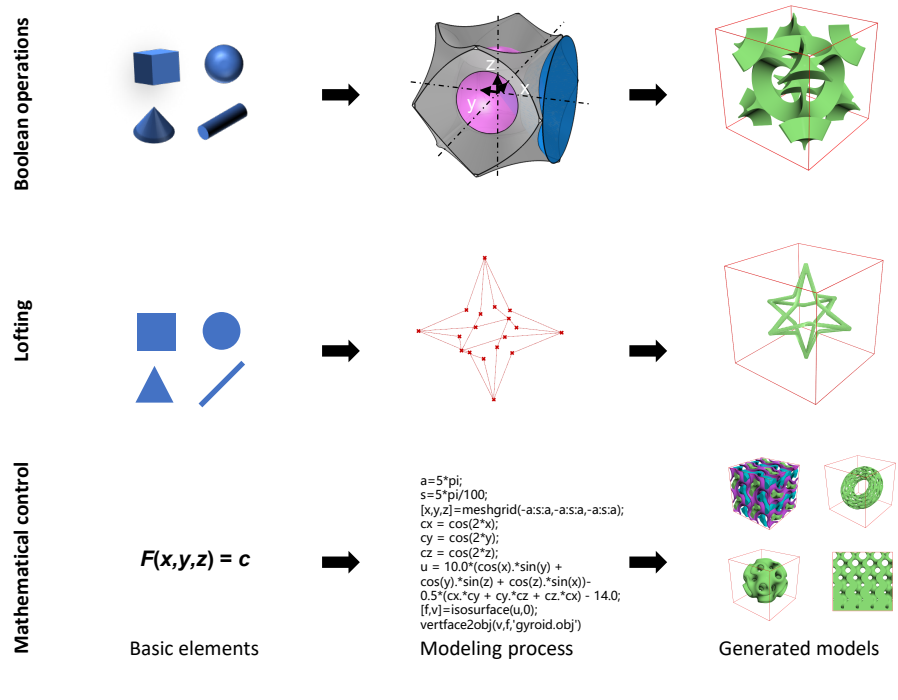


FIGURE 2.1: Three common methods used to generate auxetic metamaterials: Boolean operations, lofting, and mathematical control. Mathematical control is used in this work and could generate several complicated structures based on implicit expressions.

and strength [27, 147, 148]. Metal-based 3D printing techniques allow the fabrication of auxetic metamaterials made of metals, such as structural steel and titanium alloy [149, 150]; however, the plasticity highly restricts their application where large deformations are required. Although some fabrication methods have been developed to ensure both resilience and stiffness, the feasible structures are highly limited. For instance, wire-woven metals manufactured by forming helical wires can achieve high energy absorption and fracture resistance capabilities. However, their basic geometries are mainly 3D truss-like cells, which do not allow fabricating complex internal shapes [87, 88].

In this chapter, I propose a new auxetic metamaterial that is mathematically generated from a new type of TPMSs, and harness electroless plating to enhance the performance of the 3D-printed auxetic metamaterial. First, the geometries of the TPMS-based auxetic metamaterial are mathematically generated with an arbitrary relative density. I then investigate the auxetic behavior of the metamaterial under uniaxial compression using a 3D-printed specimen, followed by verification via FEM simulations. Next, I metalize the 3D-printed models by plating a layer of nickel on their surfaces and evaluate their performance under multiple compression tests. Finally, I quantify the effective mechanical and conduction properties and present them in the form of maps depending on the relative densities and nickel layer thicknesses.

2.2 Materials Design Strategy by Mathematically Control

A minimal surface is a smooth surface that has zero mean curvature and locally minimizes the surface area for a given boundary [151]. When a minimal surface is translationally symmetric in three dimensions, it is called a TPMS. TPMSs can be modeled

using different level-set approximation equations. In this work, the geometry of the auxetic metamaterial is derived from Schwarz Primitive minimal surface [152], and a more complicated implicit equation is used to determine the isosurface of the designed structure [63]:

$$F(x, y, z) = ((\cos(x) + \cos(y) + \cos(z)) - 0.4(\cos(x)\cos(y) + \cos(y)\cos(z) + \cos(z)\cos(x)) + c \quad (2.1)$$

Here, the level-set constant c regulates the volume fractions of the two phases separated by the isosurface. A skeletal lattice is built after capping the open borders of the isosurface. The proposed auxetic metamaterial possesses a cubic symmetry with a single unit cell within the domain $x, y, z \in [-\pi, \pi]$. Its relative density, denoted by ρ (i.e., the volume fraction of the solid phase), has an almost linear relationship with c , as shown in Figure 2.2a. In this work, each isosurface was generated on the basis of the implicit expression using MATLAB (MathWorks, USA). The MATLAB code for modeling the auxetic metamaterial is detailed in Appendix A. After capping the isosurface borders, the geometry of the TPMS-based auxetic metamaterial was exported as STL files for 3D printing and FEM simulations. Figure 2.1 compares three different methods used to generate auxetic metamaterials: Boolean operations of simple geometries, lofting operations that create 3D objects using 3D lattices as framework with arbitrary cross-sectional shapes such as cycle and square, and mathematical control. It demonstrates the flexibility of mathematical control to build complicated structures based on TPMS-based unit cells.

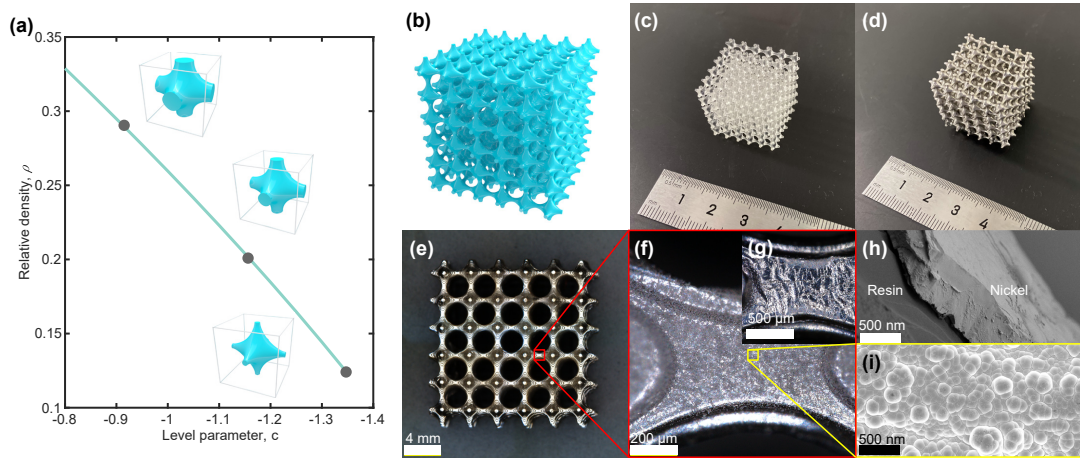


FIGURE 2.2: TPMS-based auxetic metamaterial. (a) Different relative densities determined by the level-set constant c . (b) A rendering of the auxetic metamaterial consisting of $6 \times 6 \times 6$ unit cells. (c,d) 3D-printed specimen before and after electroless nickel plating. (e,f) Optical microscope images of the nickel-coated specimen. (g) Optical microscope images of the nickel-coated specimen after multiple compression cycling. (h,i) Scanning electron micrographs showing the cross-sectional and surface morphologies of the nickel-coated specimen.

2.3 3D-Printed Auxetic Metamaterial

2.3.1 Auxetic Behavior

To evaluate the auxetic behavior and deformation mechanism, the proposed auxetic metamaterials were fabricated using 3D printing with a rubber-like material. The newly fabricated metamaterial were investigated under uniaxial compression. As can be seen from the 3D visualization of the metamaterial (Figure 2.2b), a single unit cell consists of three ligaments, which are orthogonal to the center node in 3D Euclidean space. This forms a single continuous lattice structure with smooth surfaces. I first conducted a uniaxial compression test on the 3D-printed specimen with $\rho = 0.16$ (Figure 2.2c). The high resolution of the 3D printing technique ensured a good surface finish for the 3D-printed samples.

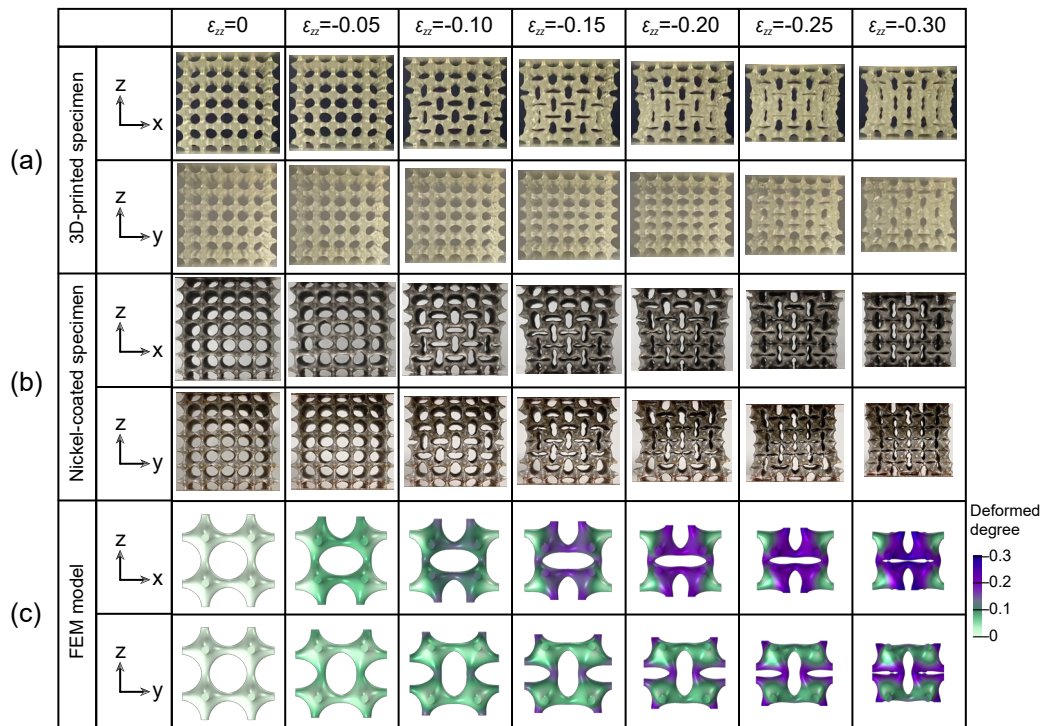


FIGURE 2.3: Buckling-induced auxetic behavior of the proposed auxetic metamaterial and a sequence of progressively deformed configurations of the (a) 3D-printed specimen, (b) nickel-coated specimen, and (c) FEM model. The deformed degree is defined as the displacement norm of each meshed element divided by the original height of the model.

Then, I performed a systematical analysis of the auxetic behavior by considering the deformed patterns, strain-stress curves, and Poisson's ratios, as shown in Figures 2.3 and 2.4. Figure 2.3a shows a sequence of progressively deformed shapes of the specimen under seven different levels of longitudinal engineering strain (i.e., change in the height of the sample divided by its original height, $\varepsilon_{zz} = (L - L_0)/L_0$). Here, the specimen witnesses a dramatic contraction in all three directions, along with changes to its interior structure (the holes are changed from circles to ellipses). The lateral shrinkage proves that it is a 3D material with negative Poisson's ratio. The structural transformation from straight to bent ligaments demonstrates that the deformation behavior is subject to buckling instability. It is noted that the periodicity of

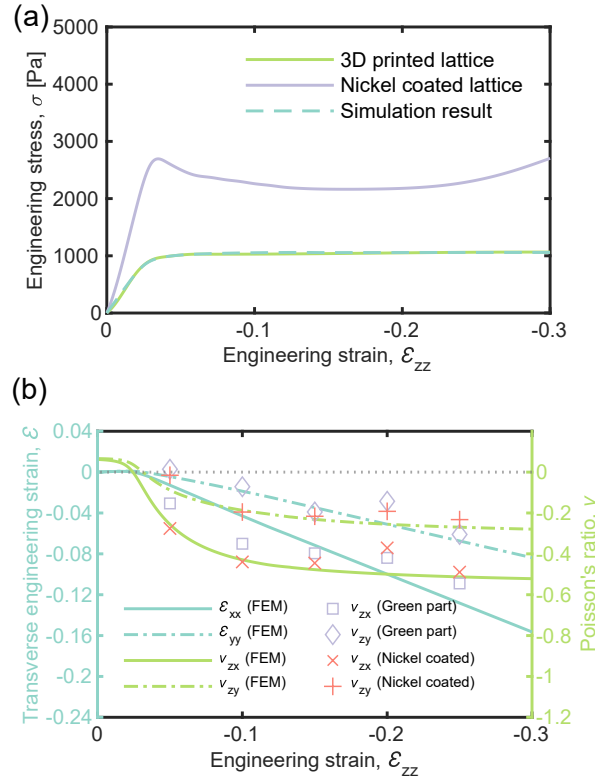


FIGURE 2.4: (a) Stress-strain curves from uniaxial compression tests and FEM simulations. (b) Evolution of the transverse engineering strains and Poisson's ratios as a function of the longitudinal strain. The FEM results are observed to be in good agreement with the experimental data.

the auxetic metamaterial can be considered as a new representative volume element (RVE) comprising $2 \times 2 \times 2$ unit cells upon buckling.

To further probe the buckling-induced auxetic behavior, I analyzed the stresses and Poisson's ratios under different compression strains. Figure 2.4a shows the stress-strain curve of the 3D-printed specimen as a function of the longitudinal strain ϵ_{zz} . It is observed that it is a typical elastic buckling curve consisting of a linear elastic regime and a stress plateau. The transition occurs at $\epsilon_{zz} \approx -0.03$ when the ligaments begin to bend, which further demonstrates the buckling-induced auxetic behavior. Because the structure is difficult to shrink when there are no empty interior spaces, I set a stop condition when the ligaments around the holes come into mutual contact. As a result, the densification region of stress-strain curves is missed, and the overall deformation strain is approximately $\epsilon_{zz} \approx -0.3$.

A more quantitative evaluation of the negative Poisson's ratios is shown in Figure 2.4b, where these ratios are calculated from the engineering strain as $\nu_{ij} = -\epsilon_{jj}/\epsilon_{ii}$, for $i, j = x, y, z$. The transverse strains ϵ_{xx} and ϵ_{yy} are obtained from the average transverse strains of the four nodes of the inner-most RVE to reduce the influence of boundary conditions, including that of the friction on the up and down surfaces and the freedom of the exterior traction-free surfaces. This is attributable to the approximation that the innermost RVE can be assumed as an infinitely periodic structure [11]. The calculated Poisson's ratios (ν_{zx} and ν_{zy}) first monotonically decrease and then reach a plateau after $\epsilon_{zz} \approx -0.1$. Each plateau lasts over a wide range from $\epsilon_{zz} \approx -0.1$ to -0.3

for $\nu_{zx} \approx -0.5$ and $\nu_{zy} \approx -0.25$.

In the next stage, I conducted FEM simulations using an RVE consisting of $2 \times 2 \times 2$ unit cells to investigate the auxetic behavior more qualitatively and quantitatively. The stress-strain curve of the FEM model shows excellent agreement with the result from the 3D-printed specimen (Figure 2.4a). Moreover, the progressively deformed configurations from the FEM simulation are substantially alike compared to the experimental results (Figure 2.3c). The geometry shrinks in all three directions accompanying the bending of ligaments and the rotation of nodes, demonstrating that the proposed auxetic metamaterial belongs to rotation structures. Figure 2.4b presents the transverse strains ε_{xx} and ε_{yy} and the Poisson's ratios plotted as a function of the longitudinal strain ε_{zz} . It is clear that the transverse strains decrease with ε_{zz} under compression, exhibiting lateral constriction behavior. The Poisson's ratios calculated from the transverse strains also fit the experimental data well. The Poisson's ratios are positive during the initial compression and become negative after the structure undergoes buckling; then, this trend gradually decreases and reaches a plateau with further loading. To clarify whether the periodic boundary condition will remove all possible size effects, I performed FEM simulations on a $6 \times 6 \times 6$ model using periodic boundary condition (Figure 2.5). It shows the same result in terms of stress-strain curve, Young's modulus, and critical buckling stress and strain compared with the $2 \times 2 \times 2$ model. Further, Figure 2.5 also reveals the deformation mechanism that leads to the auxetic effect; the compression leads to the bending of ligaments, the rotation of nodes, and the transformation of holes from circles to ellipses. Overall, the excellent agreement of the deformed patterns, stress-strain curves, and Poisson's ratios with the experimental observations demonstrate the accuracy and efficacy of our FEM model.

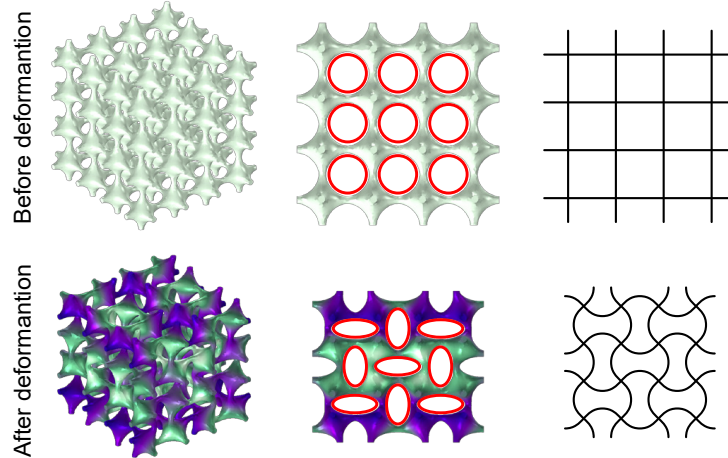


FIGURE 2.5: Auxetic behavior of a $6 \times 6 \times 6$ model showing agreement with the $2 \times 2 \times 2$ model and revealing the deformation mechanism of the proposed auxetic metamaterial.

2.3.2 Influence of Relative Density

Given the outstanding qualitative and quantitative agreement between the experiment and the FEM simulation, I further explore the influence of the relative density of the new auxetic metamaterial on the mechanical properties based on FEM models. Five different relative densities ranging from 0.12 to 0.28 are considered. The stress-strain curves from the FEM simulation results are shown in Figure 2.6a, where the

stresses are normalized using the Young's modulus of the matrix material, $E_0 = 0.6615$ MPa. This shows that both the Young's modulus (E) and critical buckling stress (σ_c) increase with the relative density. The critical buckling strain (ε_c) also rises from about 0.009 to 0.101, providing evidence that a higher relative density suppresses the buckling behavior.

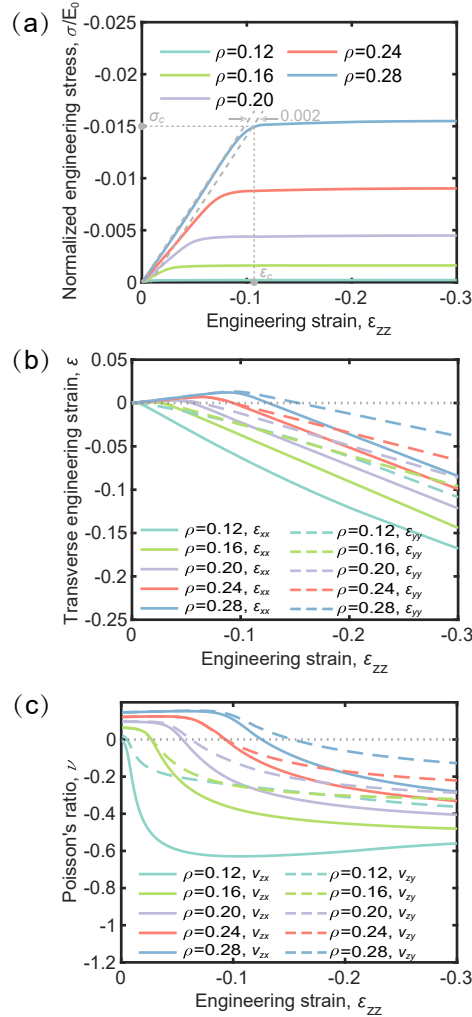


FIGURE 2.6: Influence of relative density on mechanical properties. Evolutions of the (a) normalized engineering stresses, (b) transverse engineering strains, and (c) Poisson's ratios as function of the longitudinal strain. The methods of calculating Young's moduli E , critical buckling strains ε_c , and critical buckling stresses σ_c are also illustrated in the first figure.

Figure 2.6b presents the transverse strains ε_{xx} and ε_{yy} versus the longitudinal strain ε_{zz} from the FEM simulation results. The evolution of the transverse strains displays a similar tendency: a short plateau followed by a continuous decline. It is noteworthy that the short plateaus are extended, and the ultimate transverse strains are lessened as the relative density increases. I also calculated the Poisson's ratios from the transverse strains, as shown in Figure 2.6c. Similarly, the Poisson's ratios at the same ε_{zz} increase with relative density, for example, the Poisson's ratios ν_{zx} increases from -0.58 to -0.29 at $\varepsilon_{zz} = -0.3$ when the relative density increases from 0.12 to 0.28. These results demonstrate that the proposed auxetic metamaterial is harder to shrink if it is denser.

In addition, this auxetic metamaterial displays a transversely asymmetric behavior as $\nu_{zx} \neq \nu_{zy}$.

The performance of the proposed auxetic metamaterial, including Young's modulus, critical buckling strain and stress, and Poisson's ratio, is compared with several typical auxetic metamaterials, as shown in Figure 2.7. The Young's moduli and critical stresses are normalized respectively by the Young's modulus of their constitute materials. It shows that the proposed auxetic metamaterial has higher normalized Young's modulus and critical stress than others owing to its higher relative density. Further, the structure possesses a longer buckling strain up to -0.1 at $\rho = 0.28$ and a larger negative Poisson's ratio up to -0.63 at $\rho = 0.12$. Overall, varying relative density enables to tune the mechanical properties over a broad range.

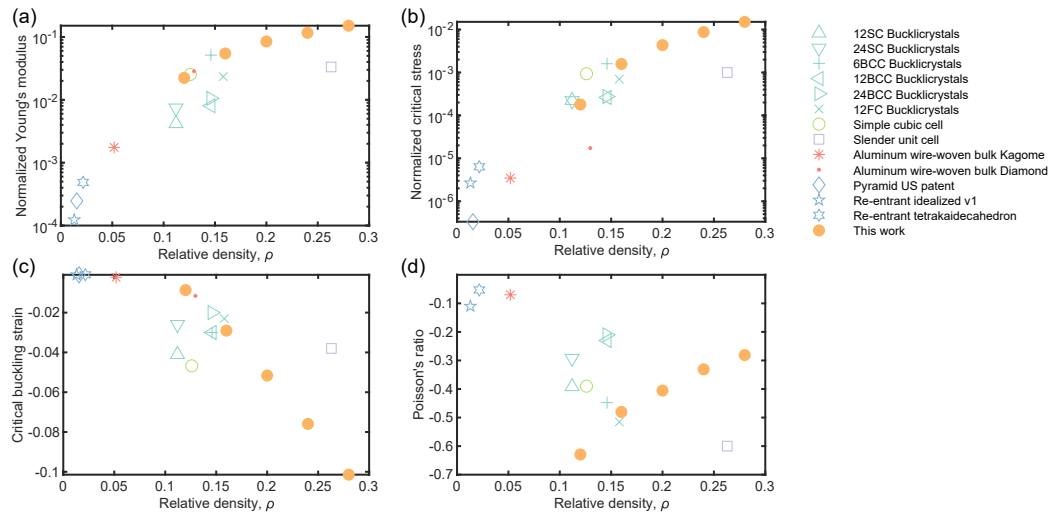


FIGURE 2.7: Comparison of the proposed auxetic metamaterial with several typical auxetic metamaterials, including Bucklicrystals [11], simple cubic cell [134], slender unit cell [135], aluminum wire-woven lattices [87], pyramid US patent, re-entrant idealized v1, and re-entrant tetrakaidecahedron [126]. (a) Normalized Young's modulus, (b) Normalized critical buckling stress, (c) Normalized critical strain, and (d) Poisson's ratio.

2.4 Metallized 3D-printed Auxetic metamaterial

2.4.1 Influence of Nickel Layer

To further functionalize the auxetic metamaterial, I coated a conformal nickel layer onto the surfaces of the 3D-printed specimen with $\rho = 0.16$ by electroless plating. After plating a nickel layer of $0.57 \mu\text{m}$ thickness, the overall structure remains unchanged without apparent volume shrinkage or expansion (Figure 2.2d). Moreover, the dense nickel layer, having a grain size of hundreds of nanometers, adheres to the resin surface well, thereby ensuring good structural stability after large deformation (Figures 2.2e–i). Note that I assumed the relative density keeps unchanged after plating as the nickel layer thickness is quite small compared to the unit cell size of 3D-printed models.

Figure 2.3b displays the continuous deformed patterns of the nickel-coated specimen under uniaxial compression, which exhibits a similar result as that of the 3D-printed specimen and FEM model. In addition, compared with the 3D-printed specimen, the nickel-coated specimen has nearly twice the values of the Young's modulus and critical buckling stress, but its critical buckling strain remains almost unchanged ($\epsilon_c \approx -0.03$), as shown in Figure 2.4a. Note that there are some decreases in the stresses after buckling owing to local plastic deformation and cracks in the nickel layers (Figure 2.2g). Interestingly, the 3D-printed and nickel-coated specimens possess almost identical Poisson's ratios under the same transverse strains (Figure 2.4b). The results prove that the nickel layer has a negligible impact on the critical buckling strain and Poisson's ratio, but significantly enhances its Young's modulus and critical buckling stress.

To investigate the resilience and stability of the specimens, I performed multicycle compression tests. Figures 2.8a and b compare the 3D printed specimen with the nickel-coated specimen with respect to their stress-strain curves during loading and unloading over multiple compression cycles. The small decreases in stresses for the nickel-coated specimen during consecutive compression cycles are a result of the local yield and crack of nickel layers. On the other hand, the Young's moduli decrease only marginally because the buckling behavior is a result of local deformation. When the load exceeds the critical buckling stress, the ligaments begin to bend, resulting in the plastic deformation and cracking of the nickel layers at the center of the ligaments where they bend. This part of the nickel layers contributes mainly to enhance the critical buckling stress. However, the Young's modulus is determined by entire nickel layer; the deformation and cracks of the nickel layers in these local regions reduce the Young's modulus only slightly. Nevertheless, both kinds of specimens reach peak stress when compressed to $\epsilon_{zz} = -0.3$, and recover their original heights after load removal. The stress-strain curves are also nearly identical even after 20 compression cycles, demonstrating excellent resilience and stability for both classes of specimens.

To explore how the mechanical and conduction properties are enhanced by increasing the thickness of the nickel layers (t), I deposited nickel layers having different thicknesses on the 3D-printed specimens with $\rho = 0.16$ by varying the electroless plating time. The thicknesses of the nickel layers are nearly linearly dependent on the plating time, and a nickel layer of about $1.71 \mu\text{m}$ thickness was formed by plating 30 min (Figure 2.8c). The stress-strain curves from the first cycle of compression tests are shown in Figure 2.8d, revealing a mechanical enhancement that the stresses increase with the thickness at the same ϵ_{zz} . Compared with the non-plated specimen, the one with the $1.71 \mu\text{m}$ nickel layer has an approximately ten-fold increase in terms of its stiffness and strength, increasing from 35 kPa to 375 kPa in terms of Young's modulus and from 0.9 kPa to 9 kPa in terms of critical buckling stress, respectively (Figures 2.8e and f). Surprisingly, the critical buckling strains are almost independent of the thickness of the nickel layer, and have a constant value of $\epsilon_{zz} \approx -0.03$.

After plating the nickel layer, these specimens become conductive. Figure 2.9a displays the conductivity-strain curves of a sample with $t = 0.57 \mu\text{m}$ and $\rho = 0.16$ during multiple compression tests. Likewise, the conductivity-strain curves also have excellent repeatability after 20 cycles of compression, without apparent losses in their conductivities. Under compression, the electrical conductivity increases linearly from 128 S/m initially to 230 S/m until the specimen suffers buckling; thereafter, it decreases immediately and then increases during further compression. After unloading, the electrical conductivity is almost restored to its original point, in pace with the recovery of the specimen. The results further prove the remarkable resilience and stability of these specimens under multiple large compressions.

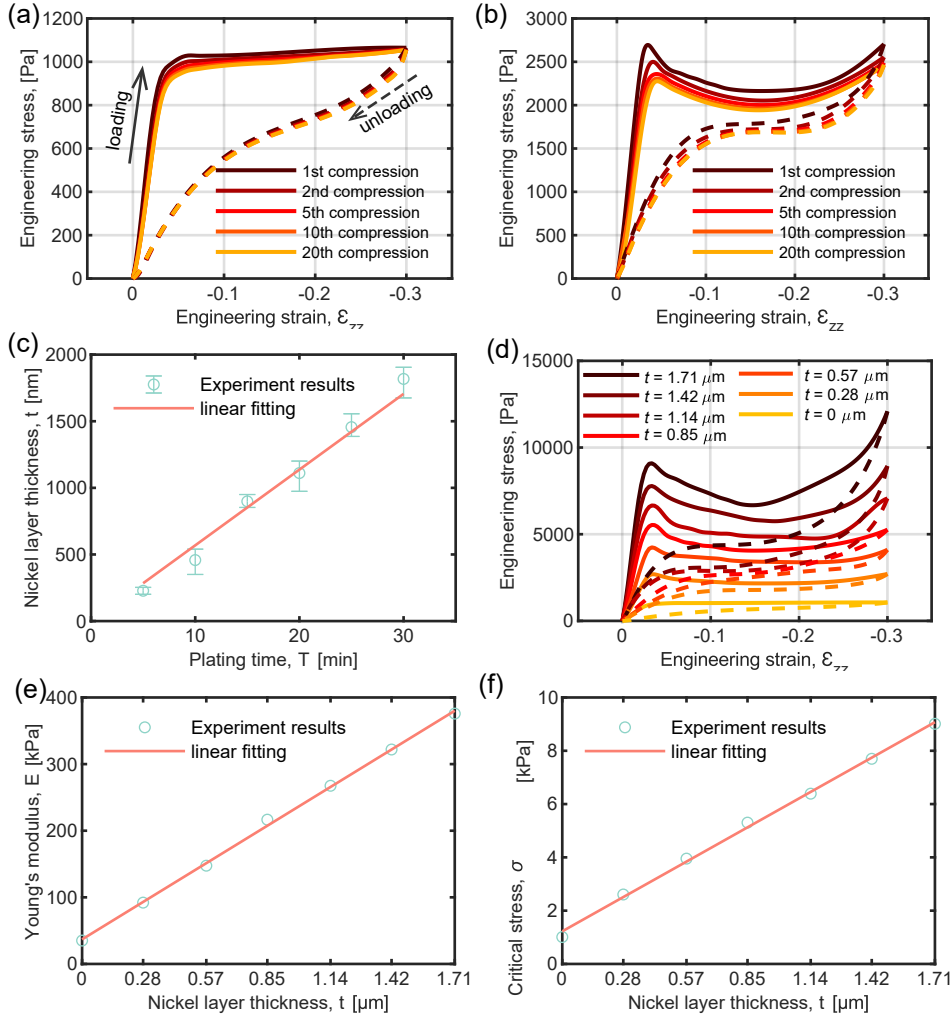


FIGURE 2.8: Influence of nickel layer thickness on mechanical properties. Stress-strain curves of (a) a 3D-printed specimen with $\rho = 0.16$ and (b) a nickel-coated specimen with $\rho = 0.16$ and $t = 0.57 \mu\text{m}$ from multiple compression tests. (c) Evaluation of the nickel layer thickness that is linearly dependent on plating time. (d) Stress-strain curves of nickel-coated specimens with different thicknesses of nickel layers from the first cycle of compression tests. Dependence of (e) the Young's modulus and (f) critical buckling stress on the nickel layer thickness. In the stress-strain curves, solid lines represent loading and dot lines represent unloading.

I also explored the influence of the nickel layers on the electrical conductivities by coating different thicknesses of the nickel layers on the 3D-printed specimens with $\rho = 0.16$. Figure 2.9b presents the conductivity-strain curves of these specimens from the first cycle of compression tests. Analogous to the stress-strain curves in Figure 2.8d, each of these conductivity-strain curves consist of three parts during loading: a steep incline followed by a drop and a gradual rise. As expected, the conduction is enhanced remarkably by plating thicker nickel layers; for example, when the thickness increases from $0.28 \mu\text{m}$ to $1.71 \mu\text{m}$, the conductivities increase from approximately 58 S/m to 371 S/m at the initial shape (Figure 2.9c).

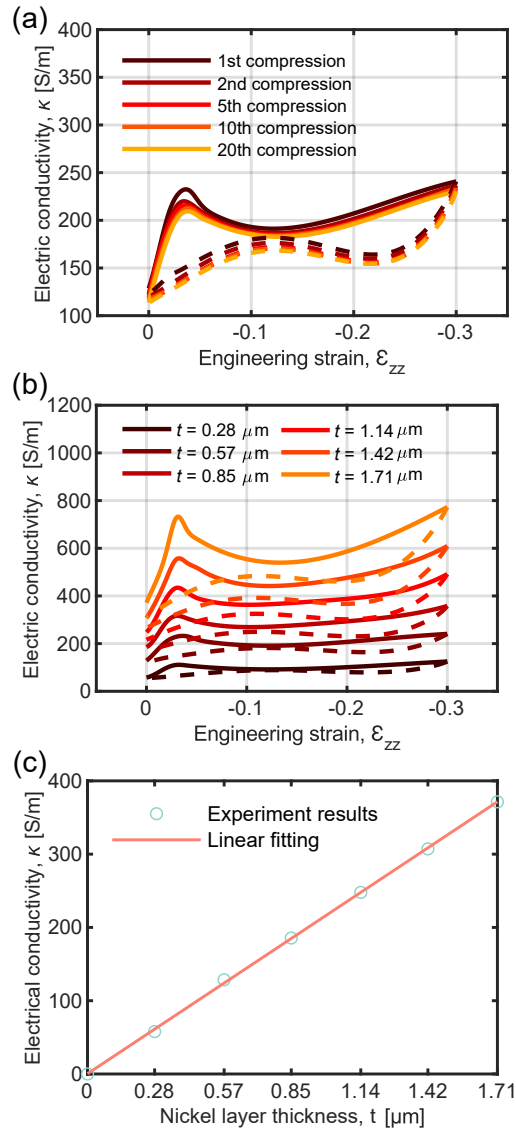


FIGURE 2.9: Influence of nickel layer thickness on conduction properties. (a) Conductivity-strain curves of the nickel-coated specimen with $\rho = 0.16$ and $t = 0.57 \mu\text{m}$ from multiple compression tests. (b) Conductivity-strain curves of nickel-coated specimens with different thicknesses of nickel layers from the first cycle of compression tests. (c) Dependence of conductivity on the nickel layer thickness at the initial shapes. In the conductivity-strain curves, solid lines represent loading and dot lines represent unloading.

2.4.2 Data Maps of Mechanical and Conduction Properties

I further conducted a more comprehensive study by investigating the mechanical and conduction properties of the material dependent on the relative density and nickel layer thickness. I fabricated a range of specimens by electroless plating of nickel layers with different thicknesses on 3D printed models with $\rho = 0.12 - 0.28$. Their effective mechanical and conduction properties, including Young's moduli, Poisson's ratios, critical buckling strains, critical buckling stresses, and electrical conductivities, were calculated from the first cycle of uniaxial compression tests. These results are

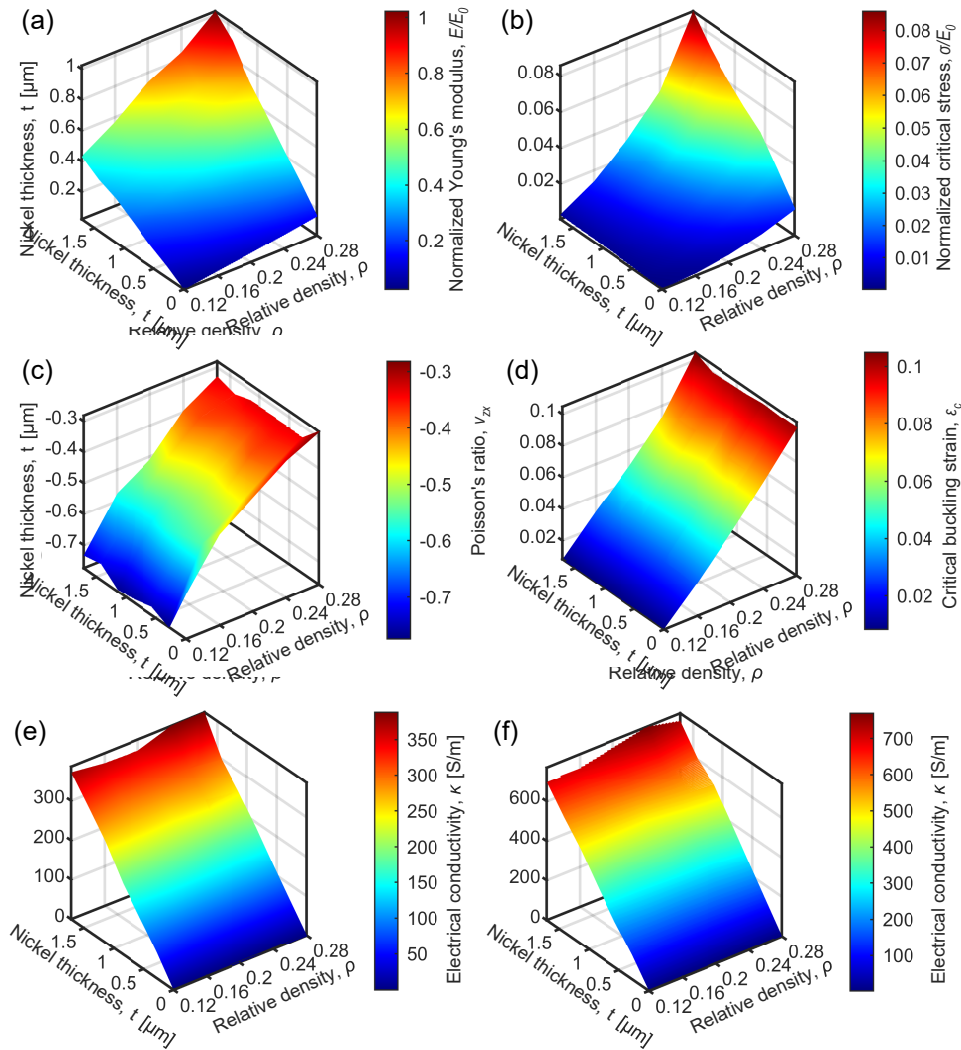


FIGURE 2.10: 3D Contour maps of mechanical and conduction properties: (a) normalized Young's modulus E/E_0 , (b) normalized critical buckling stresses σ_c/E_0 , (c) minimum Poisson's ratios ν_{zx} at $\epsilon_{zz} = -0.3$, (d) critical buckling strains ϵ_c , (e) electrical conductivities κ at the initial shapes, and (f) electrical conductivities κ at critical buckling shapes. The results are built by integration of the results obtained by plating $t = 0.28, 0.57, 0.85, 1.14, 1.42$, and $1.71 \mu\text{m}$ nickel layers onto the 3D printed specimens with $\rho = 0.12, 0.16, 0.20, 0.24$, and 0.28 , as indicated by the gray dots in the first map.

presented as contour maps in Figure 2.10, thus providing a method to tune the mechanical and conduction properties.

Figures 2.10a and b respectively present the Young's moduli and critical stresses from the experimental results, which are normalized by the Young's modulus of the 3D-printed resin, $E_0 = 0.6615 \text{ MPa}$. Increasing either the relative density or the nickel layer thickness can tremendously enhance the Young's moduli and critical stresses. After plating a $1.71 \mu\text{m}$ thick nickel layer on the 3D-printed specimen with $\rho = 0.28$, the normalized Young's modulus increases from 0.02 to 1.02 and the critical stress increases from 1.79×10^{-4} to 8.60×10^{-2} compared with the green 3D-printed specimen with $\rho = 0.12$.

Regarding the tuning of the Poisson's ratios for ν_{xy} (data were taken from the points at $\varepsilon_{zz} = -0.3$) and critical buckling strains, changing only the relative densities appears to be a suitable solution (Figures 2.10c and d). It is worth noting that the Poisson's ratios and critical buckling strains are nearly independent of the nickel layer thicknesses, but are dominated by the relative densities. The Poisson's ratios increase from approximately -0.78 to -0.29 and the critical buckling strains increase from 0.01 to 0.1 when the relative densities increase from 0.12 to 0.28.

However, the electrical conductivities are hugely determined by the nickel layer thicknesses. Figures 2.10e and f show the electrical conductivities at the initial and critical buckling shapes, respectively. This shows that the 3D-printed specimens become conductive after plating with nickel layers of hundreds of nanometers thickness on the surfaces, and a $1.71 \mu\text{m}$ nickel layer achieves a conductivity of 700 S/m. Moreover, these results also indicate that the conductivities are difficult to manipulate by varying the relative density; although, for the same nickel layer thickness, the 3D-printed specimen with a higher relative density has a larger conductivity than the one with a lower relative density at critical buckling shapes.

2.5 Summary

I presented a novel auxetic metamaterial originating from a type of TPMS structure. The mathematically defined modeling method enables the designing of more complicated systems using the metamaterial as basic unit cells. The relative density of the metamaterial is determined by varying the level-set parameter of implicit expression. The compression tests, along with the FEM simulations, demonstrated that the auxetic behavior of the new metamaterial is dominated by buckling instability and is retained over a broad range of longitudinal strain values up to 0.3. The metamaterial was 3D printed using a rubber-like material, followed by plating with nickel nanolayers; this produced a fully reversible and resilient substrate, whose mechanical and conduction properties were highly tunable by varying the relative density and nickel layer thickness. More importantly, data maps of the Young's moduli, critical buckling stresses and strains, Poisson's ratios, and conductivities provide guidance for functional applications of the material. Finally, although this work focused only on a single TPMS structure and a single plated metal, it is highly recommended that a structural gallery combining other TPMSs and electroless plating techniques (e.g., Cu, Ag, and Au) can be developed in future work, thereby paving a way towards functional applications, such as strain sensors, actuators, and electrochemical energy storage and conversion.

2.6 Methods

2.6.1 Specimen Preparation

To reduce the effects of the dimensions on the experiments, each model used in the experiments consisted of $6 \times 6 \times 6$ unit cells (Figure 2.2b). The specimens of the proposed auxetic metamaterial were fabricated using an elastic photopolymer resin (Elastic 50A resin, Formlabs, USA) and a 3D printer (Form 3, Formlabs, USA). To achieve a subtle surface finish, no additional support structures were used, and the layer thickness and length of each specimen were set to 0.05 mm and 24 mm, respectively. After washing with isopropanol for 10 min, these 3D-printed specimens were fully cured at 60°C for 20 min.

I used an electroless nickel plating method to metalize the 3D-printed specimens. First, each sample was neutrally degreased in a cleaning solution containing 50 g/L Na_2CO_3 , 35 g/L Na_2SiO_3 , and 3 g/L $\text{C}_{12}\text{H}_{25}\text{NaO}_4\text{S}$ for 5 min. After rinsing thoroughly with distilled water for 2 min, the sample was etched in a 3 M NaOH solution for 30 min, followed by rinsing again with distilled water for 2 min. In the next stage, the sample was sensitized in an aqueous solution containing 20 g/L SnCl_2 and 20 mL/L 37% HCl for 5 min, and thereafter activated in an aqueous solution containing 0.1 g/L PdCl_2 and 20 mL/L 37% HCl for 5 min. After rinsing with distilled water, nickel was deposited in an electroless manner using a nickel plating bath containing 32 g/L $\text{NiSO}_4 \cdot 6(\text{H}_2\text{O})$, 20 g/L $\text{Na}_3\text{C}_6\text{H}_5\text{O}_7$, 25 g/L NH_4Cl , and 28 g/L NaPO_2H_2 . This step was performed at 95 °C, and the plating time was varied from 5 to 30 min to achieve different nickel layer thicknesses. Finally, the nickel-coated sample was rinsed with distilled water and dried under a nitrogen stream. All chemicals used in the electroless nickel plating process were purchased from Sigma-Aldrich.

2.6.2 Characterization

Optical microscope images were obtained using a 3D digital microscope (DSX1000, OLYMPUS, Japan). Scanning electron micrographs were acquired using a scanning electron microscope (Gemini500, Zeiss, UK) with an 8 mm working distance and 5 kV accelerating voltage. The surface of nickel layer was captured under Inlens detection signal, whereas the cross-section the nickel layer and the interface of the nickel layer and resin were captured under SE2 detection signal. The nickel thickness was determined by measuring the width of the nickel layers in the SEM images.

2.6.3 Uniaxial Compression Tests and Current–Voltage Characteristics

The mechanical properties of the prepared specimens were evaluated by static compression tests using a motorized test stand (ESM303, Mark-10, USA). The specimens were uniaxially compressed between two plates at a constant displacement rate of 1 mm/min for both loading and unloading. These results were independent of the displacement rate, which is an excellent approximation to the stationary conditions in FEM simulations. The load and displacement data were recorded to produce stress-strain curves, and the deformation patterns of the specimens were captured using two cameras. With regard to the data analyses, the Poisson's ratios of each specimen were evaluated by extracting the displacements of the nodes of the deformed geometries from the recorded videos via postprocessing in MATLAB. The Young's moduli were measured by linearly fitting the initial linear portions of the stress-strain curves during loading. The critical buckling strains and stresses were defined by the 0.2% offset strain based on the shape of the stress-strain curves during loading.

The conduction properties of the specimens were also evaluated during the compression tests, as illustrated schematically in Figure 2.11. The two compression plates were covered with insulating tape on the inside and copper foil tape on the outside. The copper foil tapes were connected to a digital sourcemeter (Series 2400 SourceMeter SMU, Keithley, USA) to determine the current-voltage characteristics. A constant voltage (U) of 0.2 V was applied to obtain the electric currents (I) under different strains. Thus, the electrical conductivity (κ) is determined by the equation $\kappa = IL/UL_0^2$, where L is the height of the 3D-printed models during the compression, $L_0 = 24$ mm that is the length of the 3D-printed models, and $S = L_0^2$ that is the sectional area of the 3D-printed models

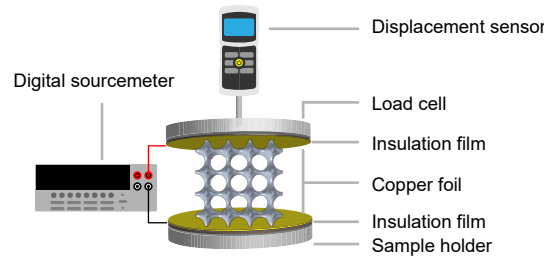


FIGURE 2.11: Schematic illustrating the stress–strain and conductivity–strain curves by uniaxial compression tests.

2.6.4 Finite Element Method Simulations

A deformation problem with a periodic microstructure, i.e., a RVE, was solved using a nonlinear FEM to simulate the deformation state at finite strain [153, 154]. The displacement field w in an RVE is divided into the uniform part \bar{u} and the periodic part \tilde{u} : $w = \bar{u} + \tilde{u}$. The uniform displacement \bar{u} is described by the macroscopic displacement gradient \bar{H} as $\bar{u} = \bar{H}Y$, where Y is the coordination system in the RVE. The boundary value problem of an RVE is formulated as a self-equilibrium problem for a periodic displacement field \tilde{u} :

$$\int_{\Omega_Y} \mathbf{P} : \nabla_Y \tilde{\eta} d\Omega_Y = 0 \quad \forall \tilde{\eta} \in W_{\text{periodic}} \quad (2.2)$$

where \mathbf{P} is first Piola–Kirchhoff stress, $\tilde{\eta}$ is the variation of the periodic displacement \tilde{u} , Ω_Y is the volume of the overall RVE, and W_{periodic} is the real solution space of the periodic function.

Based on the periodicity of the displacement field, the difference in displacements at two points A and B, which satisfy the periodicity on the corresponding surfaces of the RVE, is derived as $w_A - w_B = \bar{H}(Y_A - Y_B)$. The above node-based boundary conditions are set on the finite element model of an RVE, and the displacement field w is then controlled by the macroscopic displacement gradient \bar{H} . Following the definition of an RVE, a macroscopic variable can be calculated as the volume average of the corresponding microscopic variable. Thus, the macroscopic stress $\bar{\mathbf{P}}$ can be evaluated as

$$\bar{\mathbf{P}} := \frac{1}{\Omega_Y} \int_{\Omega_Y} \mathbf{P} d\Omega_Y \quad (2.3)$$

Based on the above equations, the deformation behavior of the new auxetic meta-material were further quantitatively investigated using an FEM simulation platform (COMSOL Multiphysics Ver. 5.4, COMSOL, Sweden). As the 3D-printed resin can be considered as a hyperelastic material, I defined the matrix material in the simulations using the incompressible neo-Hookean model for simplicity. The material model was a single parameter model with a Young’s modulus of 0.6615 MPa that was fitted from the compression tests. As the deformation behavior under compression was subject to buckling instability, a linearized buckling analysis was first performed to compute the first-order buckling mode shape, followed by a post-buckling analysis using the computed mode shape. For the linearized buckling analysis, a fixed external load was

applied along the z -axis to compute the shape of the buckling mode. For the post-buckling analysis, a parametric sweep of the displacement along the z -axis was used with a stop condition when adjacent boundaries were in contact. The post-buckling analysis helped to obtain the stress-strain curves in the three-dimensional Euclidean space. Specifically, models were built using approximately 2.5×10^5 second-order tetrahedral solid elements. All simulations were performed under periodic boundary conditions. The method applies these periodic boundary conditions to the three pairs of faces of the unit cell, which is based on a RVE technique [153, 154].

Chapter 3

Forward Design of Reprogrammable Mechanical Metamaterials using Shape Memory Polymers

3.1 Introduction

In this chapter, I propose a new functionality, reprogrammability, to make the mechanical responses changeable by developing a light-responsive shape-memory polydimethylsiloxane (SM-PDMS). The reprogrammability can address one of the limitations of mechanical metamaterials, i.e., they often harness zero-energy deformation modes and possess fixed mechanical responses. Specifically, I propose three different reprogrammable SM-PDMS metamaterials with different mechanical responses, namely, an auxetic SM-PDMS, a chiral SM-PDMS, and a buckling-induced SM-PDMS. Their mechanical responses can be switched after fabrication.

Among the gallery of mechanical metamaterials, flexible mechanical metamaterials, which can recover their original shape after large deformations, exhibit great potential for application in soft robots [94, 117, 118, 155–162], whose performance can be enhanced by the complex collective behavior of highly deformable flexible metamaterials. For example, auxetic metamaterials made of rubber-like materials can densely shrink in all three directions under a large uniaxial compressive load and recover to its original shape without fracture or failure [163]. Additionally, origami-inspired metamaterials can be designed to possess single-direction flexible motion while remaining stiff against other types of deformations [164].

Since being firstly proposed in 2014 in the electromagnetic regime [165], the concept of programmable metamaterial has been extended to acoustic, physics, thermal, and mechanics fields [166–171]. Programmability refers to the function that the properties of metamaterials can be designed and achieved via reconfigurable or digital coding approaches. Regarding mechanical metamaterials, the programmability can be harnessed to obtain a tunable stiffness [168], tailorable negative Poisson's ratio and arbitrary thermal expansion [170], and multiple deployable and reversible configurations [171], among other desirable properties. However, programmability is always achieved during the design process, and the material's mechanical responses are hardly changed after fabrication.

To have an impact on soft robots, flexible metamaterial with reprogrammability is required. This allows changing the complex motion of soft robots directly by reprogramming the architecture itself, rather than fabricating a new one. Several strategies have been harnessed to achieve reprogrammability, such as combinatorial design

[172–174], hybrid materials [48, 50, 53], association with additional physical fields [46, 116, 175, 176], and using smart materials (e.g., SMPs and LCEs) [117, 118, 177–179]. However, these previous studies have some limitations. For example, the deformation modes of hybrid mechanical metamaterials are highly dependent on the external environment (e.g., temperature and load rate). This implies that it is difficult to achieve a distinct deformation behavior under the same load condition [48, 50]. To make the reprogrammability free from the external environment, a discrete assembly has been used to construct mechanical metamaterials [173]. Similar to Lego bricks, a finite set of parts can be spatially composed to achieve different properties, including rigidity, compliance, chirality, and auxetic behavior. To make it assembly-free with a distinct mechanical response under the same load, smart materials with changeable properties (e.g., SMPs) have the potential to make continuous, monolithic structures with reprogrammability. However, mechanical metamaterials made of SMPs hardly undergo large deformations due to the plasticity of SMPs at room temperature (below the transition temperature) [109, 112, 117–119]. Therefore, it is desired to make reprogrammable mechanical metamaterials with SMPs that can undergo large deformation and have stimulus-response properties.

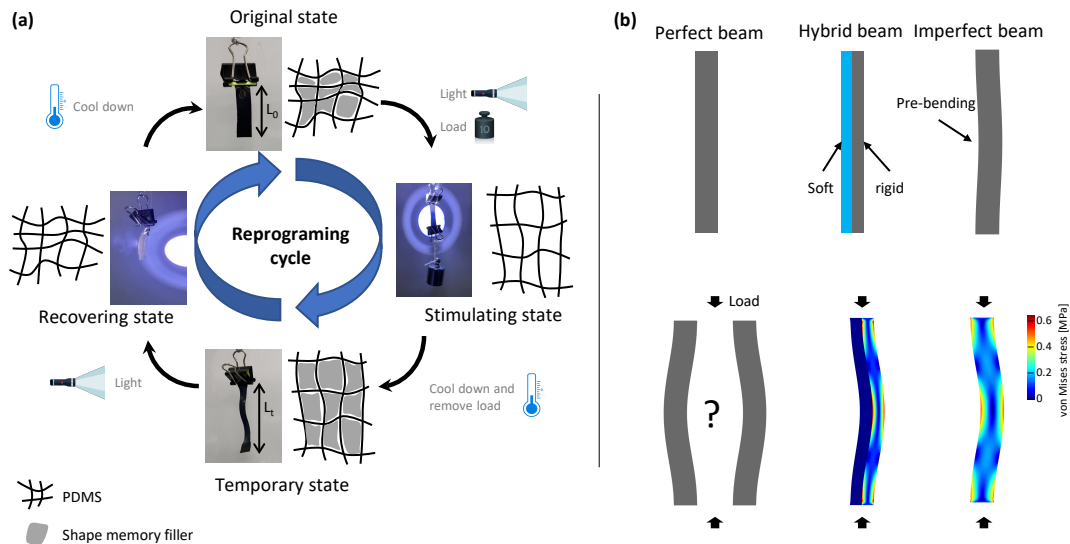


FIGURE 3.1: Reprogramming the deformation behavior of a beam using the SM effect. (a) Photothermally-induced SM effect of a SM-PDMS. The SM-PDMS has an original length (L_0) and its SM filler component was solid (top insert). During photothermal stimulation and under a load, the SM filler was melted and the SM-PDMS was gradually stretched (right insert). After keeping the load until it cooled down, the SM filler solidified and the SM-PDMS kept a stretched temporary length (L_t) (bottom insert). The SM filler was melted after receiving local photothermal stimulation again, and the SM-PDMS gradually recovered to its original length (left insert). (b) Tuning deformation modes using a hybrid beam or applying pre-bending to form a geometric imperfection. The buckling direction of a SM-PDMS beam could be manipulated by either applying local stimulation to form a hybrid beam (corresponding to the stimulating state) or applying a pre-bending to form a geometric imperfection (corresponding to the temporary state).

To address these aforementioned limitations and challenges, I propose a novel

strategy that combines imperfections with the SM effect to reprogram the deformation behavior of mechanical metamaterials. In this study, SM fillers and photothermal nanoparticles were combined with polydimethylsiloxane, a rubber-like soft material, to impart light-responsiveness and SM capabilities (Figure 3.1a). After receiving light stimulation, the proposed SM-PDMS becomes softer and reconfigurable above the melting point (T_m) because of the photothermal effect. The deformed shape remains after cooling to room temperature (below the crystallization temperature, T_c), and it recovers its original shape after further light stimulation. Guided by numerical analyses, I demonstrate the ability to harness the SM-PDMS to design three different flexible metamaterials with distinctive deformation modes, namely, an auxetic SM-PDMS, a chiral SM-PDMS, and a buckling-induced SM-PDMS, which exhibit reprogrammable expansion and shrinkage, twist, and rotation behaviors, respectively. Finally, for demonstration purpose, I show an application for manipulating the buckling-induced SM-PDMS to make an actuator capable of locomotion along a preferred direction after on-demand local stimulation. Furthermore, I expect the reprogrammability of SM-PDMS to be particularly advantageous in soft robotic applications requiring reversible, on-demand mechanical responses.

3.2 Materials Design Strategy using Shape Memory Polymers

The basic idea of this study was to harness either material or geometric imperfections to reprogram the deformation modes of flexible metamaterials (see Figure 3.1b). Considering a beam under a compressive uniaxial load as an example, it was difficult to predict the bending direction for a perfect beam. However, if the beam was hybrid and composed of laterally attached beams (made of two materials with different stiffnesses), it would predictably buckle to the stiffer side (when loaded slowly in compression). Another way to predict the bending direction was by introducing geometric imperfections. The beam would bend on its curved side if it has an initial curvature.

I found that these requirements were satisfied using SM-PDMS as a constituent material, as shown in Figure 3.1a. SM-PDMS is a rubber-like material that maintains its permanent shape at room temperature. It becomes softer and reconfigurable after heating over its T_m by receiving light due to the photothermal effect and retains the temporarily deformed shape after cooling. This process is known as the programming process. It can return to its permanent (original) shape from the temporarily deformed shape by reheating, paving the way to reprogram it. SM-PDMS was prepared by physically mixing PDMS with a SM filler (i.e., 1,10-decanediol), followed by doping with plasmonic titanium nitride (TiN) nanoparticles to enable precise photothermal stimulation. PDMS is elastic, transparent, biocompatible, and gas-permeable, and can achieve more functionalities via surface and bulk modifications. For example, its stiffness can be tuned by changing the mixing ratio and it can become electrically and thermally conductive by embedding free molecules, nanoparticles, or by altering the composition of the base elastomer before polymerization. These characteristics make it a suitable candidate for soft robotics and actuators [155–158, 162]. TiN nanoparticles, a broadband plasmonic light absorber, are responsive to sunlight and thus can locally heat their surrounding [180]. SM-PDMS was physically entrapped with solid crystalline small molecules of SM filler that induced a reversible phase transition in the permanent network (crosslinked PDMS). The permanent network was a hyperelastic network that maintained a permanent shape and recovery after a large deformation.

The entrapped SM filler, which dominates the SM effect, can fix a temporary shape by counterbalancing the load stored in the permanent network.

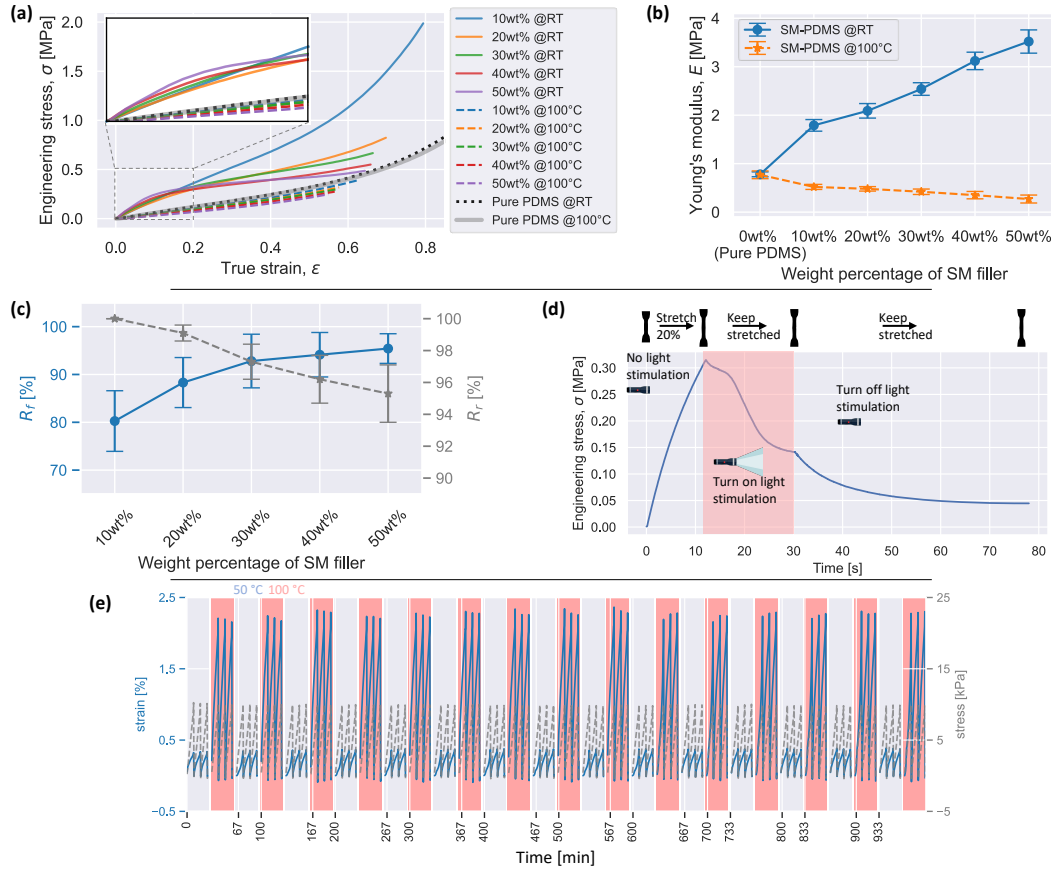


FIGURE 3.2: Material properties of the constituent material (photothermally-induced SM-PDMS) for mechanical metamaterials. (a) Stress-strain curves of SM-PDMS ($T_m \approx 76^\circ\text{C}$) at 50°C and 100°C . (b) Effective Young's modulus versus the weight percentage of SM filler. (c) Shape fixity (R_f) and recovery (R_r) versus the weight percentage of SM filler. (d) Light-response test of a dumbbell-type SM-PDMS sample with 30 wt% SM filler content. The sample was stretched 20% before given light stimulation. The light stimulation was turned off after the stress became stable. The stress did not reach to the original zero value due to the residual stress in PDMS. (e) Fatigue test of an SM-PDMS sample with 30 wt% SM filler content.

The stiffness needs to be investigated first to harness the SM-PDMS to reprogram flexible metamaterials. I demonstrated the ability to tune the stiffness of SM-PDMS over a wide range (Figures 3.2a and b). Figure 3.2a shows the stress-strain curves of dog-bone test specimens with different SM filler weight percentages. They were fitted using the Ogden hyperelastic material model to calculate the Young's modulus at a small strain ($E = \frac{3}{2} \sum_{i=1}^3 \mu_i \alpha_i$), as shown in Figure 3.3. Importantly, the SM-PDMS exhibited an elastic behavior in the low-strain region even in the hard state below the melting point. This was clearly different from the general SM polymers that exhibited plastic properties under similar conditions. As shown in Figure 3.2b, the Young's modulus at room temperature increased from 0.78 to 3.52 MPa as the SM filler increased from 0 to 50 wt%. The Young's modulus at 100°C (above T_m) decreased from

0.78 to 0.27 MPa. This indicated that increasing the weight percentage of the SM filler can increase the stiffness difference between the SM-PDMS before and after local stimulation. A stiffness difference of six times could be achieved for an SM-PDMS with 30 wt% SM filler. Note that the T_m and T_c of the SM-PDMS were barely affected by the weight percentage of the SM filler and were maintained at approximately 76 °C and 64 °C, respectively, based on the differential scanning calorimetry (DSC) thermal analysis (see Figure 3.4). The DSC thermal analysis was carried out at -50 – 150 °C, and there was no damage found on the SM-PDMS. For the sake of application, room temperature is the suitable ambient surrounding for the proposed SM-PDMS metamaterials.

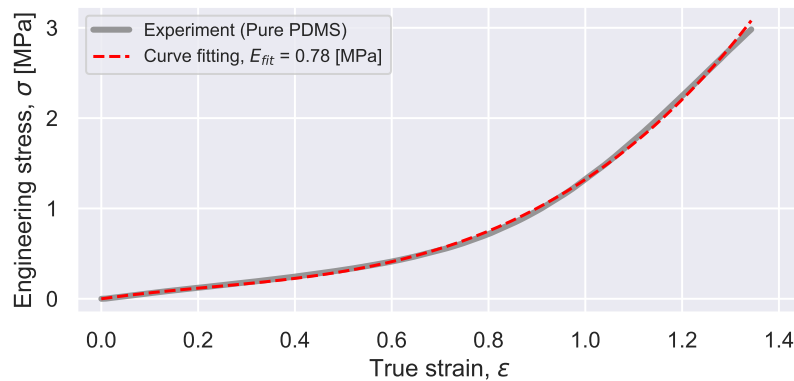


FIGURE 3.3: Curve fitting of a typical stress-strain curve for a dog-bone specimen of an SM-PDMS using the Ogden hyperelastic material model.

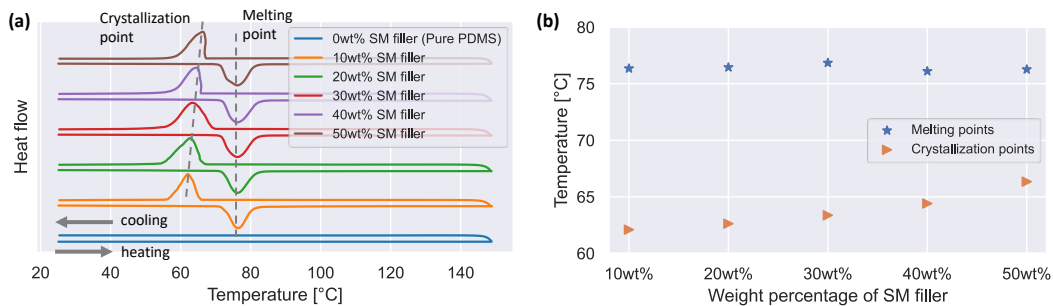


FIGURE 3.4: (a) DSC curves of SM-PDMS samples with different SM filler weight percentage. (b) Melting and crystallization temperatures versus SM filler weight percentages.

Geometric imperfections are highly associated with two SM factors: shape fixity (R_f) and recovery (R_r). R_f is the ability of SM-PDMS to fix its temporary shape during the programming process, whereas R_r is the ability of SM-PDMS to recover its permanent shape during the reprogramming process. R_f was dominated by the reversible phase (SM filler), whereas R_r was dominated by the permanent network (PDMS). Figure 3.2c shows the effect of filler weight percentage on R_f and R_r . The results showed that with an increase in the filler weight percentage, R_f increased from approximately 80% to 95%, whereas R_r remained above 95%. The SM-PDMS sample with 30 wt% SM filler had an R_f of 93% and R_r of 97%. Geometric imperfections could be achieved

by applying pre-bending to a locally stimulated beam, as shown in Figure 3.1b. That is, a compressive load was applied on a beam after local stimulation, and the beam would keep a bent status if the load was kept until cooling to room temperature. The magnitude could be controlled by applying different compressive strains on the beam.

Considering the mechanical properties and SM effect, the SM-PDMS with 30 wt% SM filler had a suitable reprogrammable performance (i.e., six-time stiffness difference before and after local stimulation; $T_m = 76^\circ\text{C}$; $T_c = 64^\circ\text{C}$; $R_f = 93\%$; and $R_r = 97\%$) and was used for fabricating mechanical metamaterials. The recovery of the material after deformation is called a deforming cycle, and changing the deformation mode is called a reprogramming cycle. To investigate the fatigue resistance of SM-PDMS, I conducted two 1000-cycle load-unload tests on a dumbbell-type SM-PDMS sample (with 30 wt% SM filler) at room temperature and 100°C , respectively. For each deforming cycle, the sample was stretched to 20% and then released to its original length. The stress was measured and the results are shown in Figure 3.5. The results show that the stress repeated well even after 1000 load-unload cycles for the test at room temperature; however, for the test at 100°C , the peak stress gradually decreased initially, which can be attributed to SM filler loss. Because the SM filler was physically mixed with the PDMS rather than via chemical bonding, some of the SM filler on the surface would flow out after melting while being driven by the repeatedly pressing, softening the SM-PDMS. However, as the proposed SM-PDMS metamaterials are actuated at room temperature and the high temperature is just used to change their deformation modes, they can keep anticipative mechanical responses for their practical applications. Furthermore, I also investigated the reprogramming cycles using via DMA. The change in strain was measured to evaluate the repeatability by maintaining a certain stress (10 kPa) and varying the temperature ($50\text{--}100^\circ\text{C}$). To demonstrate this, 15 load-unload cycles were applied to an SM-PDMS sample with 30 wt% SM filler at 50°C (below T_c). Then, the temperature was gradually increased to 100°C (above T_m), followed by the application of another load-unload cycle on the sample. After cooling to 50°C , load-unload cycles were performed again on the sample. The SM-PDMS sample could sustain 15 heating-cooling cycles without fracture (see Figure 3.2e, showing acceptable repeatability).

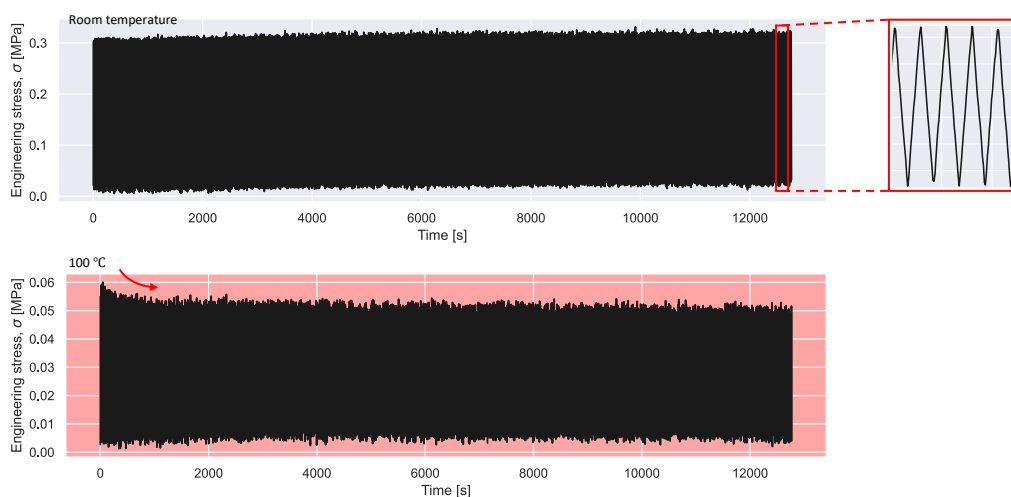


FIGURE 3.5: Load-unload tensile tests of a dumbbell-type SM-PDMS sample with 30 wt% SM filler at (a) room temperature and (b) 100°C .

To precisely measure the response time of the reprogramming process, I conducted

a photothermal response test on a pre-stretched dumbbell-type SM-PDMS sample (Figure 3.2d). The sample was pre-stretched at 20% tensile strain, and then light irradiation was applied on the sample's surface. The stress was monitored, which sharply decreased for 15 s and gradually converged under light irradiation. This is because the sample became soft when heated above its melting temperature due to the photothermal effect. The light irradiation was kept for 20 s and was turned off after the stress became stable. Afterward, the stress gently decreased because the SM-PDMS was almost fixed to the deformed shape after cooling. It is worth noting that a small residual stress remained after fixing the SM-PDMS, which further demonstrates that the SM-PDMS cannot perfectly keep its deformed shape (i.e., the fixity is less than 100%, as shown in Figure 3.2c). A demonstration of how to harness local light stimulation to create a hybrid beam with material imperfections is shown in Figure 3.1b, where a beam buckles to the right after left-side local stimulation. The preferred buckling is due to the softening of the left-side part owing to the photothermal effect by doping plasmonic nanoparticles. Figure 3.6 demonstrates the temperature and phase changes of the hybrid beam under light radiation, which makes local light stimulation possible. In our experiments, light irradiation was carried out for approximately 30 s to ensure the locally simulated parts were sufficiently heated, and the cooling process was carried out for approximately 30 s. Consequently, it takes approximately 1 min for one reprogramming process.

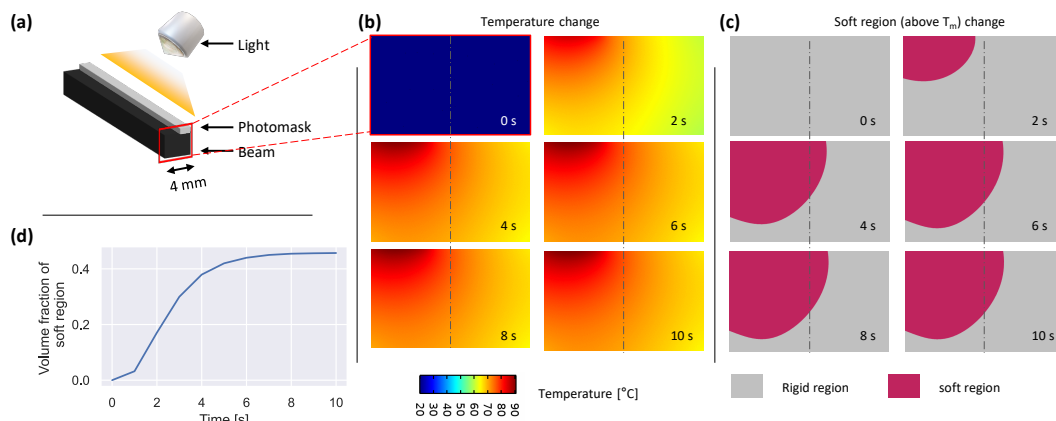


FIGURE 3.6: Simulation of the photothermal response of a SM-PDMS beam receiving local light. (a) Illustration of applying local light stimulation. (b) Progressive temperature change sequence of a beam receiving local stimulation. (c) Progressive phase change sequence of the beam receiving local stimulation. (d) Phase change of the beam receiving local stimulation. The beam becomes almost half rigid and half soft after receiving local light stimulation.

Given that the SM-PDMS had acceptable reprogrammability, I showed how to harness this to design and make three different flexible metamaterials with the desired deformation behavior in the next three sections. This was done in combination with bending, twisting, and buckling of basic elements of metamaterials that responded to a load. The deformation mode of each flexible metamaterial can be converted under ambient conditions using delicately controlled local stimulation by creating SM-PDMS metamaterials with spatially controlled arrangements of their basic elements.

3.3 Reprogrammable Auxetic Metamaterials

First, I propose an auxetic SM-PDMS whose deformation mode could be reprogrammed to switch from contraction to expansion under uniaxial compressive loading. Auxetic metamaterials are mechanical metamaterials with a negative Poisson's ratio [11, 62, 163, 181]. As the expansion or contraction can be quantitatively measured using the Poisson's ratio, the auxetic SM-PDMS shows either a positive or negative Poisson's ratio on demand. The basic element of an auxetic SM-PDMS is a beam that can bend to either the left or right, depending on the local stimulation region, as shown in Figure 3.7a. The bending direction of the beam was theoretically analyzed based on Euler's buckling theory for beams on elastic foundations (see Appendix B). According to this theory, a hybrid beam buckles to the stiffer side under a longitudinal compressive load. A hybrid SM-PDMS beam can be achieved by applying local light stimulation to the left or right region of the beam as the SM-PDMS becomes partially soft after local stimulation. The slenderness ratio of the beam (height/width, h/w) was set below 8 (Figure B.1) to prevent the beam from higher order buckling modes.

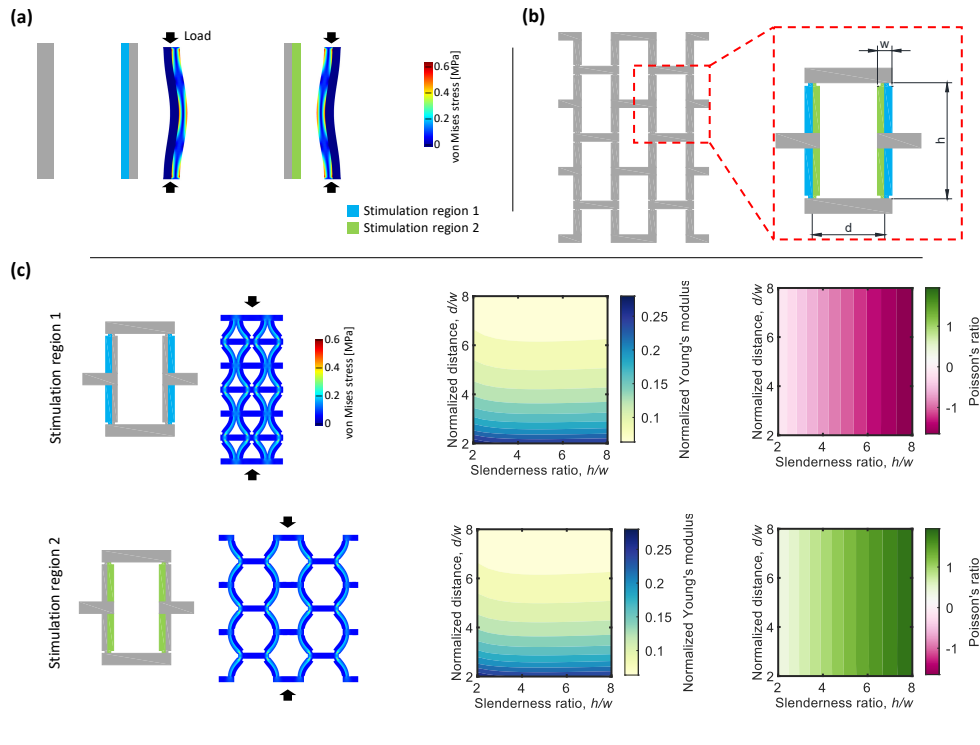


FIGURE 3.7: 2D Reprogrammable auxetic metamaterial. (a) Basic beam element. The buckling direction of the beam can be controlled using different local photothermal stimulation. (b) 2D auxetic metamaterial consisting of multiple beams with tunable geometric parameters. (c) Tunable Young's modulus and Poisson's ratio of the 2D auxetic metamaterial based on different geometric parameters and controllable deformation modes (shrinkage or expansion) based on different stimulation regions.

The 2D auxetic SM-PDMS consists of beams assembled in a stretcher bond pattern, as shown in Figure 3.7b. The brick pattern is designed to achieve a reprogrammable shrinkage and expansion behavior. Unlike re-entrant auxetic metamaterials consisting of concave polygons, the 2D auxetic SM-PDMS is composed of rectangles. The

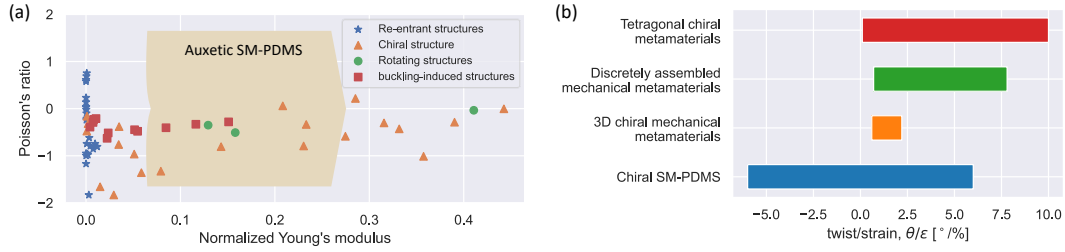


FIGURE 3.8: Comparison between the proposed auxetic and chiral SM-PDMSs and some typical mechanical metamaterials. (a) Comparison between the auxetic SM-PDMS and re-entrant, chiral, and rotating structures [11, 133, 163, 182–187]. The auxetic SM-PDMS has a Young's modulus and Poisson's ratio space covering a wide, near square region. (b) Comparison between the chiral SM-PDMS and tetragonal chiral metamaterials, discretely assembled mechanical metamaterials, and 3D chiral mechanical metamaterials [107, 173, 188]. The chiral SM-PDMS has a wider twist/strain region covering from positive to negative. The twist/strain is calculated by the twist angle divided by the applied strain.

vertical ligaments make it possible to bend right or left depending on local imperfections. Two factors were considered to realize the features of auxetic SM-PDMS: i) Mechanical properties (Young's modulus and Poisson's ratio) were tunable via three independent geometric parameters (i.e., beam width w , beam height h , and distance between adjacent beams d) before fabrication; and ii) Deformation modes (contraction and expansion) were reprogrammable using local stimulation after fabrication. I used the FEM calculations to analyze the effects of the three independent geometrical parameters on the Young's modulus and Poisson's ratio of the 2D auxetic SM-PDMS, as shown in Figure 3.7c. The 2D auxetic SM-PDMS was also compared with some typical auxetic metamaterials in terms of Young's modulus and Poisson's ratio, as shown in Figure 3.8a. It shows that the Poisson's ratios of our proposed auxetic SM-PDMS cover a square area, exhibiting both positive and negative values. For the sake of comparison with the experimental results, the beam width was set as a constant $w = 4$ mm, whereas the beam height (defined as the slenderness ratio, h/w) and the distance between adjacent beams (defined as the normalized distance, d/w) were changed based on parametric sweeping calculations. Based on the FEM simulation results, the Young's modulus of the 2D auxetic SM-PDMS was highly dependent on d/w . The Young's modulus became smaller as d/w increased. In contrast, the Poisson's ratio was less sensitive to d/w but was significantly affected by h/w ; it approached zero as h/w decreased. It is worth noting that changing the local stimulation region did not affect the Young's modulus; however, it converted the Poisson's ratio from negative to positive. This further demonstrated that local stimulation could be manipulated to reprogram the deformation modes from contraction to expansion, and vice versa, without stiffness loss.

Furthermore, I conducted an application case for making an auxetic SM-PDMS 3D hollow cylinder out of the 2D auxetic SM-PDMS, which was folded using the 2D auxetic SM-PDMS with 12×3 unit cells. The 3D cylindrical auxetic SM-PDMS exhibited imperfection-dependent deformation modes, shrinking or expanding laterally under a compressive load, depending on different local stimulation regions. Figure 3.9a shows

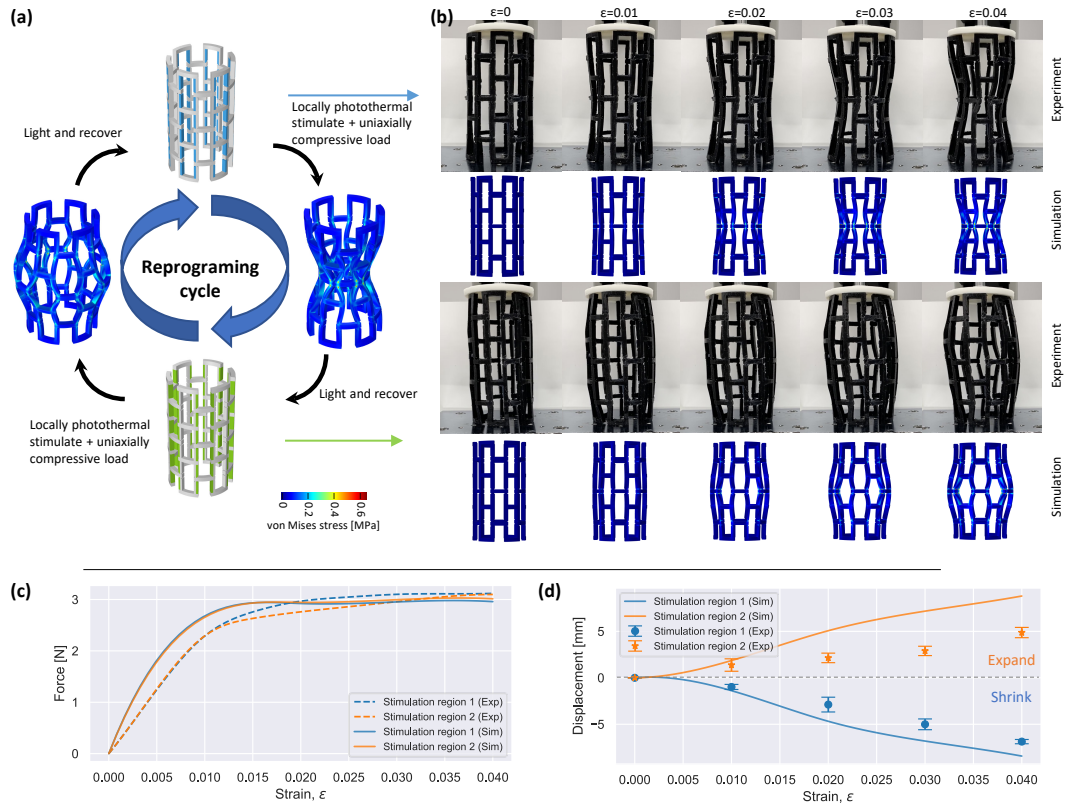


FIGURE 3.9: 3D Reprogrammable auxetic metamaterial. (a) Typical reprogrammable cycle of a 3D auxetic metamaterial that is capable of either shrinking or expanding based on different local stimulation. (b) Sequence of progressively deformed configurations of the 3D auxetic metamaterial receiving different local stimulation. (c) Stress-strain curves of the 3D auxetic metamaterial with different local stimulation under a compressive load. (d) Lateral displacement of the 3D auxetic metamaterial with different local stimulation under a compressive load.

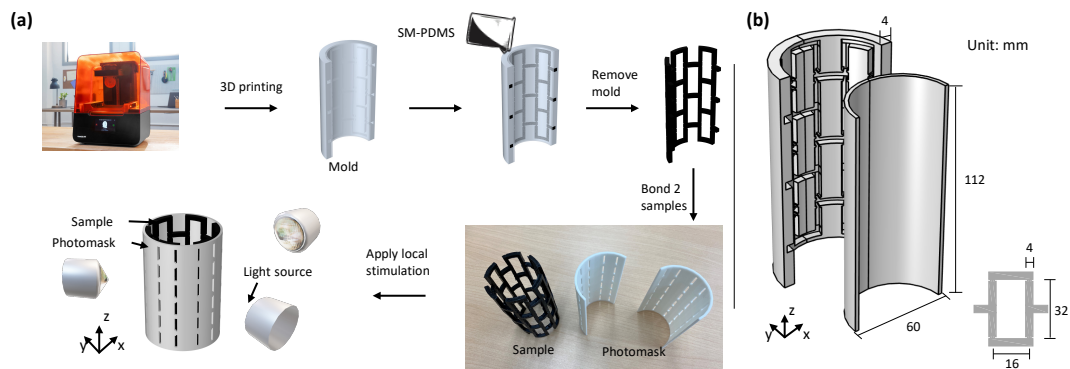


FIGURE 3.10: Reprogramming a 3D auxetic metamaterial made of SM-PDMS. (a) Process of preparing a 3D auxetic metamaterial using 3D printing to make a mold, and the illustration of applying local light stimulation. (b) Mold design of a prepared 3D auxetic metamaterial.

a typical reprogrammable cycle. However, if local stimulation was applied to the region outside a unit cell (blue region), the 3D cylindrical auxetic SM-PDMS shrunk laterally under a compressive load. After receiving global light, it recovered to the original shape. Then, it expanded laterally if local stimulation was applied to the region inside a unit cell (green region). A specimen made via 3D printing and templating is shown in Figures 3.10a and b, where a 3D auxetic SM-PDMS was made by pouring uncured SM-PDMS into 3D-printed molds and bonding the separated samples together. Local stimulation was achieved using a cylindrical photomask with specific pore arrangements, as shown in Figure 3.10a. Uniaxial compressive tests were performed on the specimens after receiving different local stimulation. Before each compressive test, the specimen recovered its original shape under global light stimulation.

Figure 3.9b shows the sequence of progressively deformed shapes of the 3D auxetic SM-PDMS specimen under five different compressive strain levels using different local stimulation. The experimental results relatively correlated with the FEM simulation results (i.e., the 3D cylindrical auxetic SM-PDMS shrunk or expanded after different local stimulation). However, it was noted that global buckling was triggered in the testing samples, which is mainly attributed to the cylinder's slenderness ratio, the wall thickness, and manufacturing error. To manufacture the SM-PDMS metamaterials, the molding method was used, where molds were 3D printed and filled with uncured SM-PDMS. These SM-PDMS metamaterials were obtained after detaching them from the molds, in which some parts would be destroyed, resulting in local nonlinear effects during deformation. When applying actuation, the overall performance and desirable functions may be degraded by these imperfections because such small dimensional errors can propagate to the entire mechanical metamaterials. To prevent such dimensional errors, it is recommended to make the mechanical metamaterials via direct 3D printing without support structures. Here, these small dimensional errors may result in global buckling. Thus, I tried to prevent global buckling by using a relatively low slenderness ratio (approximately 2) and a thick wall thickness (6 mm). Further, another efficient way to prevent this was to apply pre-bending on the hollow cylinders that had been discussed previously [189]. In addition, the imperfection-dependent deformation modes were validated by quantitatively evaluating the stress-strain curves and Poisson's ratios under different compression strains. For the same 3D SM-PDMS specimen under different local stimulation, the two stress-strain curves almost overlapped with each other and were independent of local stimulation, whereas the lateral displacements exhibited the opposite changing tendencies (Figures 3.9c and d). The difference between simulated and experimental results is attributed to laboratory errors (from devices), human force, and incomplete contact with sample holders, whereas these errors were not considered in the simulations. More importantly, the difference between the simulated and experimental displacement largely resulted from hysteresis effects due to the incomplete contact between the sample's upper and bottom surfaces with the compression plates. These results further demonstrate that the 3D cylindrical auxetic SM-PDMS has reprogrammable contraction and expansion deformation modes using local stimulation without sacrificing stiffness.

3.4 Reprogrammable Chiral Metamaterials

Next, I propose a chiral SM-PDMS whose deformation modes could be reprogrammed from twisting clockwise to counterclockwise under an uniaxial compressive load. Chiral mechanical metamaterials, which exhibit handedness out of non-centrosymmetry, produce out-of-plane deformation modes (e.g., twisting) as a result of in-plane loads

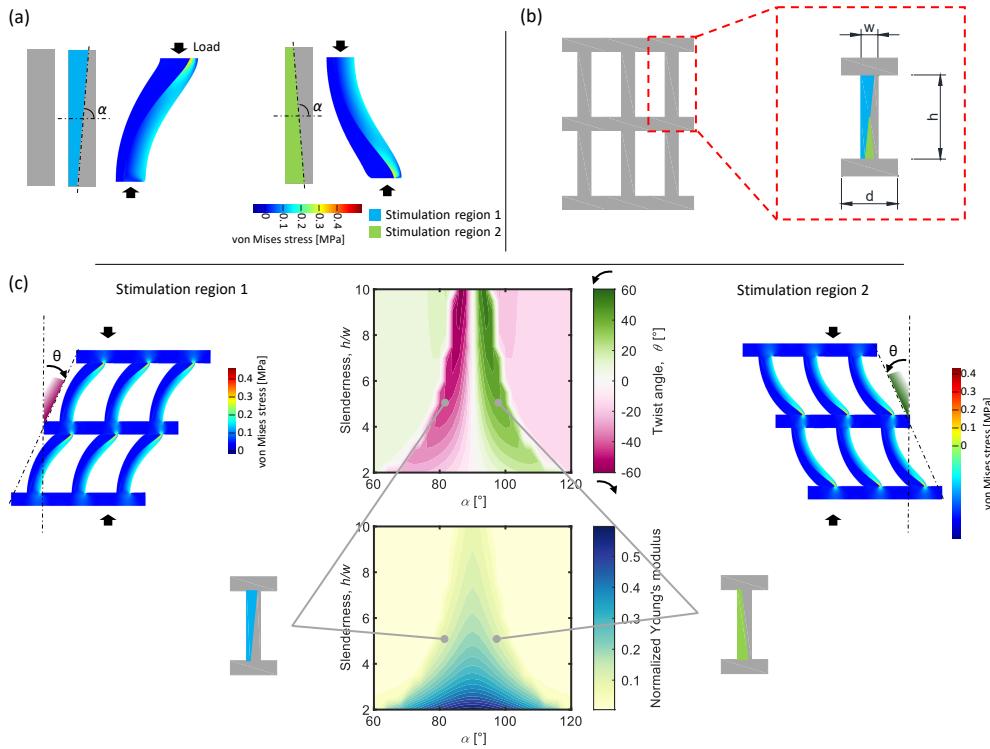


FIGURE 3.11: 2D Reprogrammable chiral metamaterial. (a) Basic beam element. The leaning direction of the beam can be controlled using different local photothermal stimulation. (b) 2D auxetic metamaterial consisting of multiple beams with tunable geometric parameters. (c) Tunable Young's modulus and twist angle of the 2D auxetic metamaterial based on different geometric parameters, and controllable deformation modes (leaning to the left or right) based on different stimulation regions. The twist angles were calculated under a 0.1 compressive strain.

[107, 190, 191]. In contrast to common chiral mechanical metamaterials, whose deformation mechanism is attributed to node rotation and ligament bending, the chiral SM-PDMS has a unique deformation mechanism that is attributed to ligament leaning. Moreover, the basic element of a chiral SM-PDMS is a beam that could lean either to the left or right, depending on the local stimulation region, as shown in Figure 3.11a. The stimulation and non-stimulation regions are rotationally symmetric, and the leaning direction can be tuned by the tilt angle α that divides the two regions.

Figure 3.11b shows the 2D chiral SM-PDMS consisting of beams assembled in a stack-bond pattern. The pattern is designed to show the possibility to achieve compression-twist deformation without geometrical chirality. Two factors were considered to determine the chiral SM-PDMS features: i) Mechanical properties (Young's modulus and twist angle) were tunable via three independent geometry parameters (i.e., w , h , and d) before fabrication; and ii) Deformation modes (lean to the left or right) were reprogrammable using local stimulation after fabrication. FEM analyses were used to investigate the effects of the three independent geometry parameters on the Young's modulus and twist angle of the 2D auxetic SM-PDMS, as shown in Figure 3.11c. The chiral SM-PDMS was also compared with some chiral mechanical metamaterials in terms of twist angle, as shown in Figure 3.8b. It shows that the twist angles of our proposed chiral SM-PDMS cover both positive and negative ranges. The beam width was set as a constant $w = 4$ mm, whereas the beam height (defined as h/w) and the

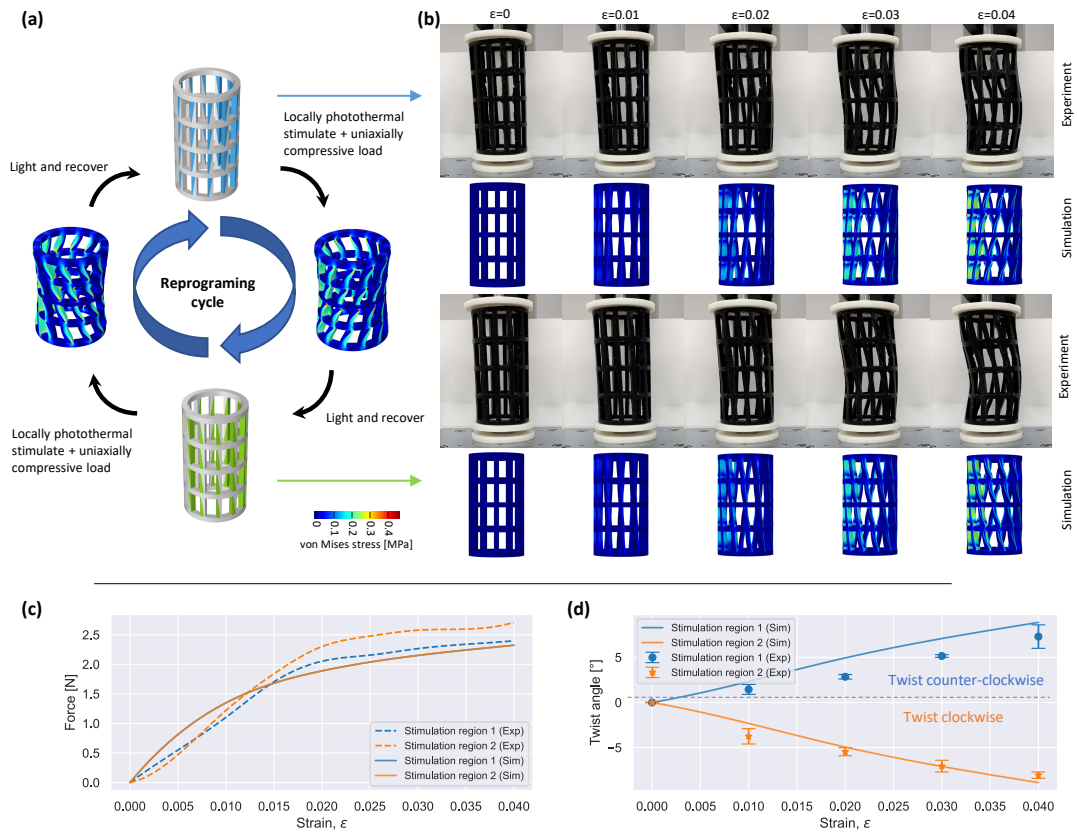


FIGURE 3.12: 3D reprogrammable chiral metamaterial. (a) Typical reprogrammable cycle of a 3D chiral metamaterial that is capable of twisting either clockwise or counterclockwise based on different local stimulation. (b) Sequence of progressively deformed configurations of the 3D chiral metamaterial receiving different local stimulation. (c) Stress-strain curves of the 3D chiral metamaterial with different local stimulation under a compressive load. (d) Twist angle of the 3D chiral metamaterial with different local stimulation under a compressive load.

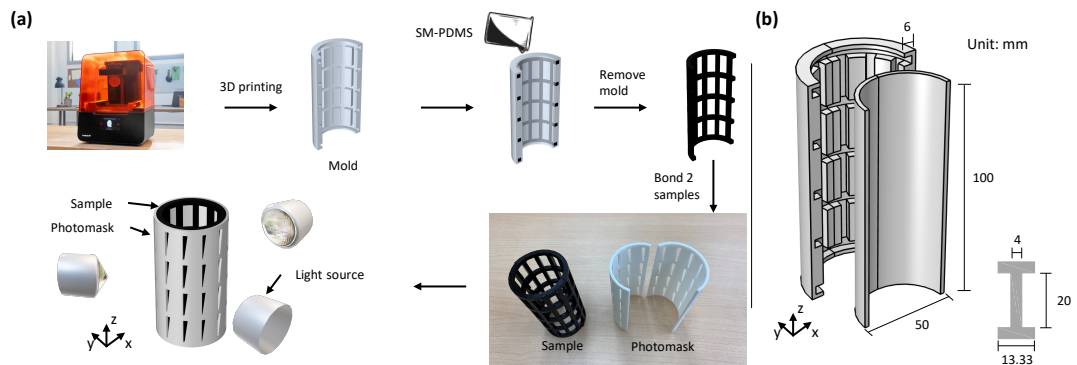


FIGURE 3.13: Reprogramming a 3D chiral metamaterial made of SM-PDMS. (a) Process of preparing a 3D chiral metamaterial using 3D printing to make a mold, and the illustration of applying local light stimulation. (b) Mold design of a prepared 3D auxetic metamaterial.

tilt angle α were changed. The normalized Young's modulus of the 2D auxetic SM-PDMS was determined by both h/w and α . The Young's modulus increased as h/w decreased or α approached 90° . Conversely, the twist angle was highly sensitive to α and had a maximum absolute value when α approached 90° . Therefore, α should be set appropriately to maximize the absolute value of the twist angle. With an increase in h/w from 2 to 8, α could either increase from 72° to 86° to reach the maximum twist angle (leaning to the right) or decrease from 108° to 94° to reach the minimum twist angle (leaning to the left). This further demonstrated that local stimulation could be manipulated to reprogram the deformation modes from leaning to the right to leaning to the left, and vice versa.

Figure 3.12a shows a chiral SM-PDMS 3D hollow cylinder folded using a 2D chiral SM-PDMS with 12×4 unit cells with w and h of 4 and 20 mm, respectively. The 3D cylindrical chiral SM-PDMS exhibited imperfection-dependent deformation modes: twisting clockwise or counterclockwise under a compressive load depending on the local stimulation region. Figure 3.12a shows a typical reprogrammable cycle: the 3D chiral SM-PDMS twisted counterclockwise under a compressive load if local stimulation was applied to the region with $\alpha = 82^\circ$; it recovered its original shape after receiving global light stimulation; thereafter, the 3D chiral SM-PDMS twisted clockwise under a compressive load if a local stimulation was applied to the region with $\alpha = 98^\circ$. Figures 3.13a and b show the preparation of a specimen via 3D printing and templating and the application of local stimulation using a photomask. Figure 3.12b shows the sequence of progressively deformed shapes of the 3D chiral SM-PDMS specimen under five different compressive strain levels and different local stimulation. The deformation patterns of the experimental results correlate with the simulated results. In addition, the imperfection-dependent deformation modes were validated by quantitatively evaluating the stress-strain curves and twist angles under different compression strains. For the same 3D SM-PDMS specimen under different local stimulation, the two stress-strain curves almost overlapped with each other and were independent of local stimulation, whereas the twist angles showed opposite changing tendencies (see Figures 3.12c and d). These results further demonstrated that the 3D cylindrical chiral SM-PDMS had reprogrammable twist deformation modes using local stimulation without sacrificing its stiffness.

3.5 Reprogrammable Buckling-induced Metamaterials

Finally, I created a buckling-induced SM-PDMS with a distinct rotational direction after different local stimulation. The buckling-induced SM-PDMS was a 2×2 array of hollow squares. The pattern is designed to allow the direction-changeable rotation and stability when placed on an uneven surface. To apply local stimulation, each square was diagonally divided into four parts, and local stimulation was applied to the two spaced parts of the four parts. Examples of applying two different local stimulations are shown in Figure 3.14a, which also shows the method of applying loads to induce an overall structural compression. Instead of the uniaxial compressive load used in the previous two structures, a pneumatic load was used to power the deformation of the buckling-induced SM-PDMS. The pillars of the buckling-induced SM-PDMS underwent buckling by applying a vacuum (evacuation) to the four chambers, resulting in its deformation into bent shapes. The bending direction was predetermined by either material imperfections introduced by local stimulation or geometric imperfections introduced via pre-deformation, which consequently causes the center area to rotate in one preferred direction. Regarding material imperfections, FEM

analyses were conducted on the structure, where the blue or green areas were set as the local stimulation regions (Figure 3.14a). The results show a preferred clockwise or counterclockwise rotation was caused if local stimulation was applied to the blue or green regions, respectively (see Figure 3.14b). Before fabrication, two geometric parameters (i.e., the width of each square w and the radius of each pore r) could be changed to tune the rotation angle and the required pressure. Figure 3.14c shows the dependence of the rotation angle on the normalized radius (r/w) and pressure, where w was set to 20 mm. These results showed that when the buckling-induced SM-PDMS was thoroughly deformed, the absolute value of the rotation angle reached a maximum of 45° when r/w approached 0.5, and gradually decreased to 30° as the r/w decreased to 0.38. In addition, the pressure required for deformation decreased as r/w increased.

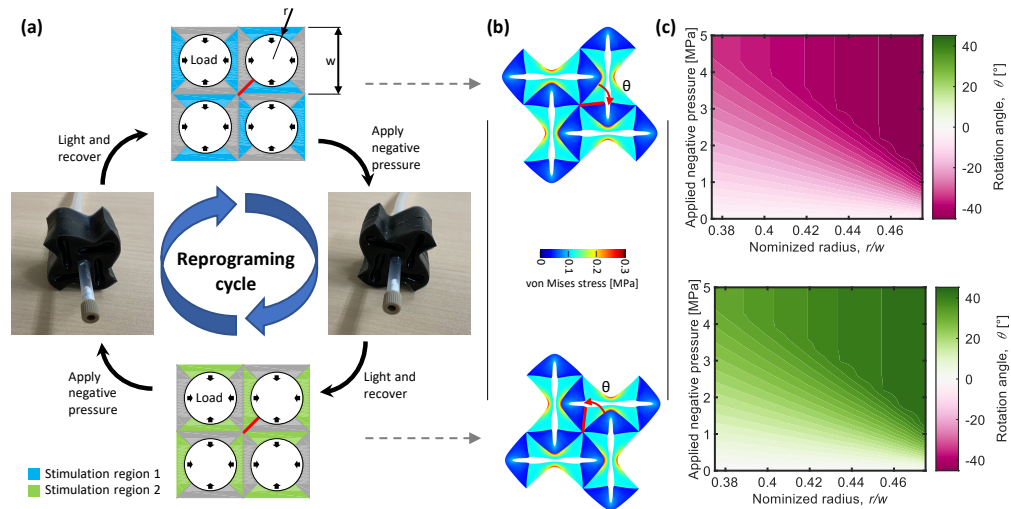


FIGURE 3.14: Reprogrammable buckling-induced metamaterial. (a) Typical reprogrammable cycle of a 2D buckling-induced metamaterial that is capable of rotating either clockwise or counter-clockwise based on different local stimulation. The basic element is hollow squares whose rotation direction can be controlled using different local photothermal stimulation. (b) FEM results of the 2D buckling-induced metamaterial after different local stimulation. They show reversed rotation direction. (c) Tunable rotation angle of the 2D buckling-induced metamaterial based on different normalized radii and stimulation regions.

We also fabricated a buckling-induced SM-PDMS prototype with w and r of 20 and 8.5 mm, respectively. Figure 3.15a and Figure 3.14b show the fabrication process and geometric size, respectively. Figure 3.15c presents the method of applying local light stimulation on the prototype assisted with a photo mask. The buckling-induced SM-PDMS prototype was a pneumatic actuator that was powered using a simple syringe. After different local stimulation, the center of the actuator could rotate in one preferred direction when a vacuum was applied (see Figure 3.14a). The center of the actuator rotated in reverse, and the actuator simultaneously recovered back to its original shape when the internal pressure was restored to ambient pressure. In addition, by taking advantage of the SM effect of the actuator, the preferred rotation could also be predetermined using geometric imperfections by applying a vacuum to a locally simulated actuator (i.e., applying a material imperfection) and then cooling to room

temperature. The geometric imperfections could be cleared by applying light stimulation to the entire actuator. A typical reprogrammable cycle is shown in Figure 3.14a.

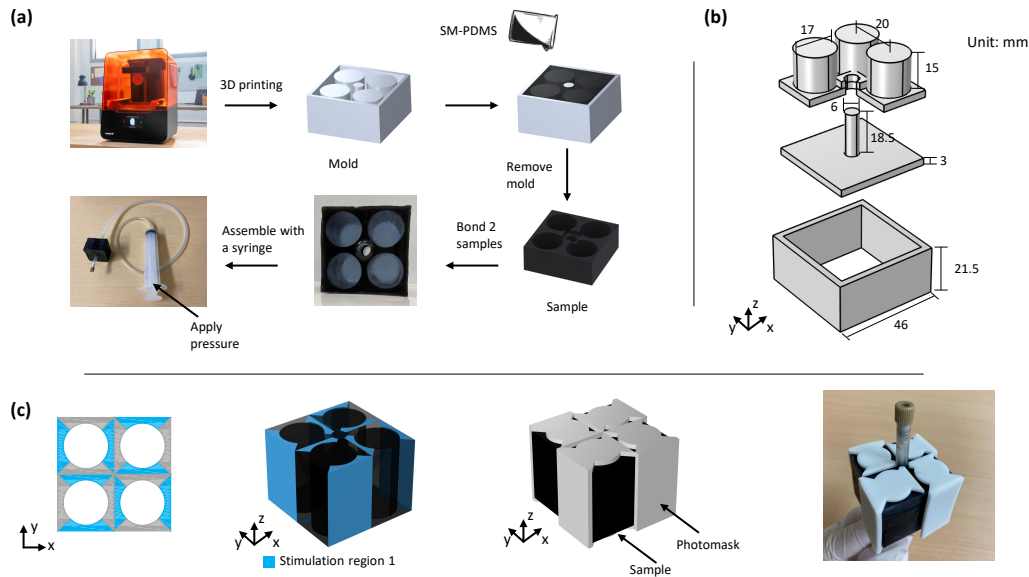


FIGURE 3.15: Reprogramming a 2D buckling-induced metamaterial made of SM-PDMS. (a) Process of preparing a 2D buckling-induced metamaterial using 3D printing to make a mold. (b) Sample size of a mold for preparing the buckling-induced metamaterial. (c) Illustration of applying local light stimulation.

A potential application of soft actuators is for the locomotion of soft robots. Figures 3.16a and b show the demonstration of carrying cargo using the actuator with the preferred rotation direction out of geometric imperfection. The actuator, which was connected to a cargo, rotated 90° and moved during a single evacuation and pressurization cycle. During evacuation, the actuator shrunk, deformed into a gear-like shape, and simultaneously rotated 45° . The actuator continued to rotate 45° owing to inertia and gravity until a force balance was reached. During pressurization, the actuator gradually recovered to its original shape. Note that in contrast to most soft robots that could only move along one direction under the same drive, the actuator can move either forward or backward depending on the on-demand geometric imperfections, exhibiting more flexibility to tune the motion mode in soft robots. In addition, the actuators could be connected in series to form a soft robotic train that provides more transportation freedom. The soft robotic train was capable of locomotion on a relatively uneven surface because each actuator unit was self-propelled similar to a four-wheel-drive vehicle (Figure 3.16c).

3.6 Summary

In summary, I showed that flexible metamaterials made of SM-PDMS can be reprogrammed into reversed deformation modes after fabrication. SM-PDMS, which is a rubber-like material with a SM effect, becomes softer after heating up to T_m and maintains a deformed shape after cooling. It can return to its original shape when

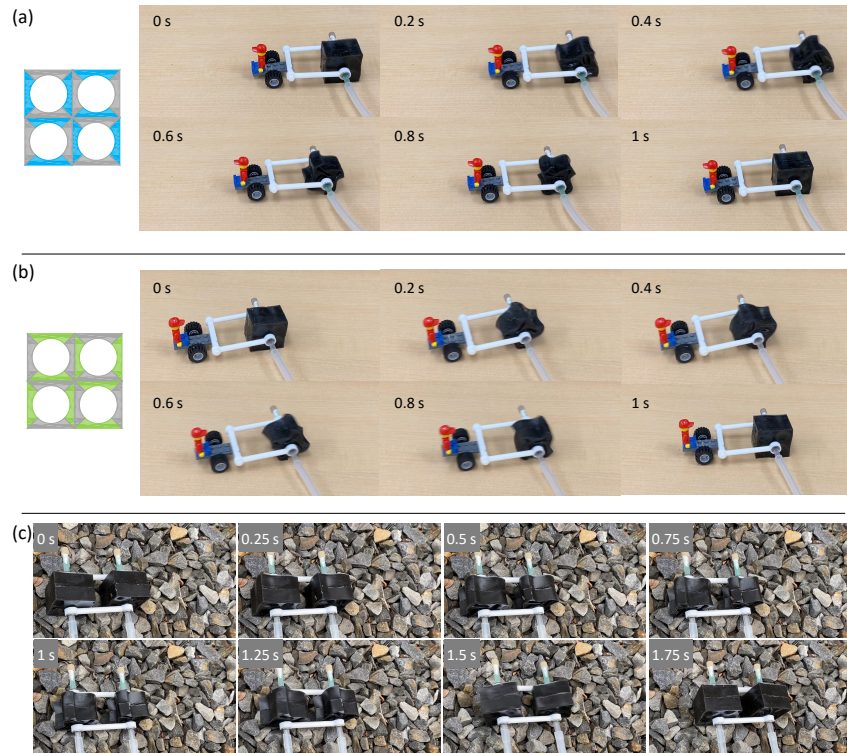


FIGURE 3.16: Reprogrammable buckling-induced metamaterial actuator. (a and b) Using different local stimulation to change the moving direction (forward or backward) of an actuator made of buckling-induced metamaterial. (c) Assembling two actuators that are capable of moving on an uneven surface (a gravel road).

heated again. Local stimulation is achieved based on the photothermal effect by doping plasmonic titanium nitride nanoparticles into the SM-PDMS. Hence, the deformation modes of an SM-PDMS metamaterial can be encoded by the stiffness difference by programming the spatial distribution of the stimulation and non-stimulation regions. After cooling and maintaining the load, the preferred deformation mode remains. The deformation mode can be reprogrammed reversibly using distinctive local stimulation as the SM-PDMS metamaterial can return to its original shape when it receives global light stimulation. Specifically, I proposed three different SM-PDMS metamaterials with different mechanical responses: an auxetic SM-PDMS that can be reprogrammed from lateral contraction to lateral expansion under a uniaxial compressive load, a chiral SM-PDMS that can twist clockwise to counterclockwise under a uniaxial compressive load, and a buckling-induced SM-PDMS that can rotate clockwise to counterclockwise under a pneumatic load. In addition, I demonstrated an application using a buckling-induced SM-PDMS actuator. The soft actuator was capable of locomotion along a preferred direction after on-demand local stimulation. The actuator can be connected in series with a soft robotic train, and its distinctive deformation mode (shrinkage into a gear shape while rotating) makes it capable of moving on uneven surfaces.

The most significant feature of our designed mechanical metamaterials is their reprogrammability, which paves the way for their application in soft robots and other structural engineering fields. The changeable mechanical response rises additional

deformation freedom and enhances their functionality. For example, the tubular auxetic SM-PDMS is a compliant structure that allows robots to overcome environmental challenges by deforming and conforming their bodies. Compared with the general auxetic compliant structures that only exhibit auxetic behavior, our designed tubular auxetic SM-PDMS exhibits both shrinkage (auxetic behavior) and expansion mechanical responses under compression, which thereby functions for exploration through unpredictable terrain [192]. Regarding the tubular chiral SM-PDMS, it can convert linear compressive motion into rotation, which is a rather unique feature of a machine. This unique actuation can be used for harnessing the interaction between materials and machines, and thus it is useful for placing them at the boundary acting as an actuator [193, 194].

Furthermore, although I only focus on mechanical metamaterials with three different mechanical responses, our approach can be extended to arbitrary 2D and 3D structures to achieve more complicated deformation modes under different loads. Reprogramming the deformation modes requires manually placing different photomasks for the sake of local light stimulation, which, however, brings about limitations in real applications where an automatic workflow is required. This limitation could be addressed by using other stimuli-responsive mechanical properties (e.g., magnetic response) which can also be accomplished by doping with other smart nanoparticles or using other smart polymeric materials [116, 178, 195].

3.7 Methods

3.7.1 SM-PDMS Preparation

The SM-PDMS was prepared by mixing the PDMS (10:1 mix ratio, Sylgard 184, The Dow Chemical Company, USA) with a SM filler (1,10-decanediol, TCI AMERICA, USA). Before mixing with the PDMS, the SM filler was milled into powder using a mortar and pestle mixing grinding bowl. Then, the photothermal effect was introduced by doping with 0.2 wt% TiN nanoparticles (Nisshin Engineering Inc., Japan). A Thinky PDMS Mixer (Thinky Mixer ARE-310, THINKY, USA) was used to efficiently mix, disperse, and deaerate the SM fillers, TiN nanoparticle, and PDMS mixture for 5 min. Thereafter, the well-mixed SM-PDMS was degassed in a polycarbonate desiccator under high-vacuum conditions for 30 min.

The SM-PDMS metamaterials and specimens used for the mechanical tests were fabricated using the molding method, as shown in Figures 3.10, 3.13, and 3.15. These molds were designed using a computer-aided design software (3Ds max, Autodesk, USA), and their dimensions are shown in Figures 3.10b, 3.13b, and 3.15b, respectively. The designed molds were printed using a stereolithography three-dimensional (3D) printer (Form 3, Formlabs, USA) with a light-reactive thermoset resin (Clear Resin, Formlabs, USA). The molds were washed with isopropyl alcohol for 10 min, followed by curing at 60 °C for 30 min. A hydrophobic layer was coated on the surface of the molds using 1H, 1H, 2H, 2H-perfluorodecyltrichlorosilane ($C_{10}H_4Cl_3F_{17}Si$, TCI AMERICA, USA) via chemical vapor deposition in a desiccator for 30 min to easily detach the SM-PDMS from the molds. Subsequently, each mold was filled with uncured SM-PDMS, and was then baked for 24 h at 60 °C. The specimens were finished by detaching them from the molds.

3.7.2 Mechanical Properties Investigation

Uniaxial tensile tests were performed using a motorized test stand (AG-Xplus-10kN, Shimadzu, Japan) at a constant displacement rate of 10 mm/min to evaluate the stress-strain curves and Young's moduli of the SM-PDMS specimens. ASTM D 412-06 (A) was used to assess the tensile properties of dog-bone (dumbbell)-type samples produced using 3D-printed dog-bone molds [196]. High-temperature tests were conducted in a thermostatic chamber (TCE-N300, Shimadzu, Japan).

In addition, the SM effect of SM-PDMS was evaluated using the fixity and recovery of the SM-PDMS dog-bone samples. First, an SM-PDMS dog-bone sample of the original length (L_0) was placed in a temperature-controlled motorized test stand. After heating to 100 °C for 10 min, the sample was slowly extended to 40% strain (the length after stretching, L_s). Then, the sample was removed from the test stand after cooling to room temperature. The sample would slightly shrink and maintain a temporary length (L_t) owing to internal stress after releasing the load. Subsequently, the samples were placed in an oven at 100 °C for 10 min. The samples almost recovered their initial shape and maintained a permanent length (L_p). The process was repeated five times for each sample to obtain the average fixity and recovery values. The strain of the SM-PDMS samples at each step was calculated as $\varepsilon_i = \ln(L_i/L_0)$, for $i = s, t, p$. The fixity (R_f) and recovery (R_r) are then given by $R_f = \varepsilon_t/\varepsilon_s$ and $R_r = (\varepsilon_s - \varepsilon_p)/(\varepsilon_s - \varepsilon_0)$, respectively.

The fatigue test of the SM-PDMS samples was performed via dynamic mechanical analysis (DMA, DMA-242E, Netzsch, Germany) according to ASTM E1640–18. The DMA tests were conducted on cylindrical specimens with a radius of 3 mm and height of 5 mm, a heating rate of 1 °C/min, and frequency of 5 Hz. The DMA chamber was heated and cooled to 100 °C for 20 min and then further cooled to 50 °C for 20 min. This process was repeated nine times. During each hold time, three load-unload cycles with a maximum stress of 10 kPa were applied to the samples.

The melting point (T_m) of the SM-PDMS samples with different weight ratios of the SM filler was monitored via differential scanning calorimetry (DSC-60, Shimadzu, Japan). Approximately 10 mg of each SM-PDMS sample was placed inside an aluminum pan with a pierced lid. The sample was heated to 150 °C and held for 10 min at a scanning rate of 10 °C/min under a nitrogen flow of 100 mL/min.

Compression tests were conducted using a motorized test stand (JSV-H1000-10N, JISC, Japan) at a constant displacement rate of 10 mm/min. Before the tests, local light stimulation was applied to each specimen using a high-brightness lighting box (LLBGR-A-15 × 20 – 25 × 15, AITEC SYSTEM, Japan) with an irradiance of 800 W/(m² · sr) for 30 s. During light irradiation, the surface of each specimen was covered with a delicately designed photomask printed using a non-transparent resin (White Resin, Formlabs, USA). During the compression tests, the deformation processes of the specimens were observed using a high-speed camera.

3.7.3 Finite Element Method Simulations

FEM simulations were conducted to investigate the mechanical response of SM-PDMS metamaterials using a FEM simulation platform (COMSOL Multiphysics Ver. 5.6, COMSOL, Sweden). The constitutive material model of SM-PDMS was fitted to the tensile tests using a six-parameter hyperelastic material model (i.e., the Ogden material model) [197–200]. For the SM-PDMS with 30 wt% SM filler, the material parameters were set as $[\mu_1, \mu_2, \mu_3] = [-0.79, -3.96, 3.37]$ MPa and $[\alpha_1, \alpha_2, \alpha_3] = [1.83, -3.25, -2.8]$ at room temperature (i.e., non-stimulated region), and $[\mu_1, \mu_2, \mu_3] = [0.01, -5.12, 14.43]$

MPa and $[\alpha_1, \alpha_2, \alpha_3] = [4.00, -0.36, 0.11]$ above T_m (stimulated region), respectively. The models were meshed using approximately $1 \times 10^5 - 3 \times 10^5$ second-order triangular solid elements for the two-dimensional (2D) geometries and second-order tetrahedral solid elements for the 3D geometries. Specifically, simulations of the 2D auxetic SM-PDMS and chiral SM-PDMS were performed under periodic boundary conditions as the 2D auxetic SM-PDMS and chiral SM-PDMS metamaterials were periodic. The method applied periodic boundary conditions to pairs of faces of the unit cell based on a representative volume element technique [153, 154].

A multiphysics coupling (heat transfer with radiation in absorbing scattering media) simulation was performed using COMSOL to simulate the photothermal response of an SM-PDMS beam receiving local light. In particular, it allowed heating to be computed because of radiation absorption. A 2D model (rectangle) was used with a thermal conductivity of 0.16 W/m/K, heat capacity of 2005 J/kg/K, absorption coefficient of 293 cm^{-1} , and scattering coefficient of 1.4 m^{-1} [201, 202]. The top right surface of the rectangle was radiated with an incident intensity of $800 \text{ W}/(\text{m}^2 \cdot \text{sr})$. The P1 approximation discretization method was applied to the simulation because the model was based on linear anisotropic scattering [203].

Chapter 4

Inverse Design of Mechanical Metamaterials by Deep Learning

4.1 Introduction

In this chapter, I convert the conventional forward design approach by developing a deep learning framework. The deep learning framework, taking advantage of conditional generative adversarial networks (CGANs), enables inverse design of 2D and 3D mechanical metamaterials. It admits variational sampling to generate multiple distinct architectures with the target properties (e.g., Young's modulus E , Poisson's ratio ν , and relative density ρ). Figure 4.1 shows the comparison between forward design and inverse design approaches.

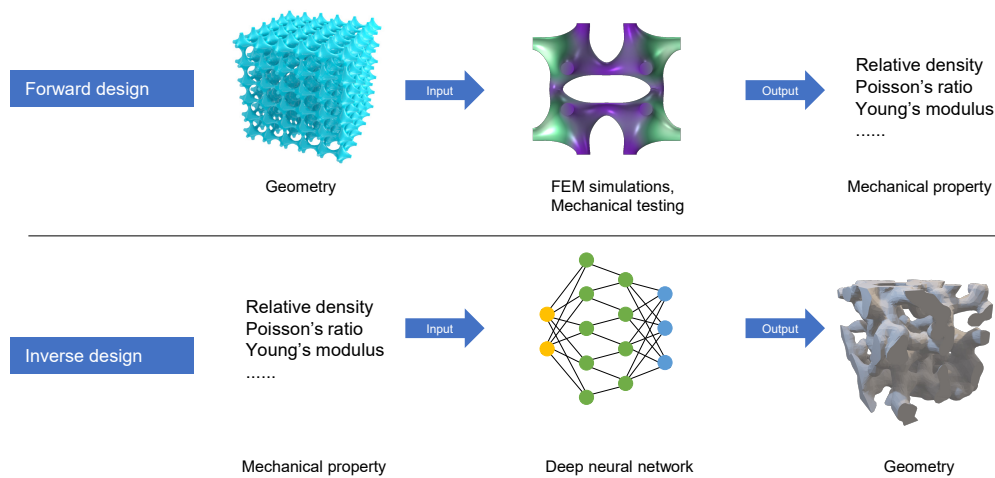


FIGURE 4.1: Comparison between forward design and inverse design.

Over the last few decades, extensive efforts have been made to design new mechanical metamaterials to achieve changeable mechanical response [8, 46, 53], novel deformation mechanisms [107, 204–206], theoretical stiffness and strength limits [14, 15, 106, 207], amongst others. Most of these studies have followed the forward design approach, that is, a structure is designed by computational modeling methods, and its effective properties are then explored using time-consuming simulations and/or experiments. Using such forward design methods, models can be generated via mathematical modeling [163, 208, 209], Boolean and lofting operations [14, 15, 106, 204, 205], and topology optimization [210, 211]. This requires experienced designers and extensive trial-and-error efforts to achieve the desired properties. Consequently, the

forward design approach hinders practical applications to some extent. Considering tissue engineering as an example, bone implants should be chosen to mimic damaged bones in terms of biocompatibility, relative density, and stiffness [26, 208, 209, 212, 213]. In such situations, the desired approach is the inverse design method, by which implants are designed and generated based on target properties and specific requirements.

Recent advances in deep learning have facilitated the inverse design of new materials using various artificial neural networks [36, 214–222]. Regarding auxetic metamaterials, however, to the best of the authors' knowledge, deep learning has not yet been successfully harnessed to create novel auxetic metamaterials and rather has been used only to predict the mechanical behavior of specific auxetic configurations [217]. One important reason for this situation is that the properties of an auxetic metamaterial are almost completely determined by the geometry and assembly of periodic unit cells. The realization of a negative Poisson's ratio requires a delicate arrangement and design of the unit cells; therefore, it is very difficult to build a large dataset consisting of thousands of geometries of auxetic metamaterials and their corresponding properties. For example, success has been achieved in previous studies only in the property prediction and pattern design of simple square-shaped cellular materials [214] or in the realization of isotropic elastic stiffness based on randomly generated architectures [216].

Regarding 3D architected materials, although the inverse design of 3D geometries has been successfully implemented in some studies, these neural networks are always combined with additional modeling process [80, 223, 224]. For example, in a recent study of the inverse design of truss metamaterials, the neural network outputs elementary lattices from existing datasets and their tessellations, which can be used to generate new truss metamaterials by geometric transformations [224]. In another study on the inverse design of spinodoid metamaterials, the neural network outputs the design parameters that can then be used to generate a topology via the linear Cahn–Hilliard model [80]. Notably, these studies adopted an indirect approach to generate such complex geometries: the trained neural networks generated modeling parameters that could be used to create geometries based on additional modeling procedures. Here, by contrast, we employ the GAN to directly generate 3D voxel-based representative volume elements (RVEs) (i.e., voxelized Voronoi lattices) without the need for an additional modeling process. Voronoi lattices are disordered architected materials; the irregularity not only makes their morphology similar to that of bones but also broadens their diversity in terms of the stiffness and strength for a given relative density.

In this chapter, I devised a deep learning framework by taking advantage of CGANs. Based on the deep learning framework, a 2D-CGAN and 3D-CGAN are harnessed for generating 2D auxetic metamaterials and 3D architected materials, respectively. Two datasets were prepared to train CGANs for inversely generating 2D auxetic metamaterials and 3D architected materials, respectively. Each datapoint in the datasets consists of a geometry and its corresponding mechanical properties. The geometries were created using Voronoi tessellation, and their mechanical properties were calculated using homogenization algorithms. After the CGANs had been well trained, it could rapidly generate new mechanical metamaterials with user-defined properties. Finally, the mechanical properties of the generated metamaterials were verified by FEM simulations and uniaxial compression tests.

TABLE 4.1: Comparison of neural networks for inverse design of mechanical metamaterials.

Input	Output	Geometry type	Neural network type	Number of training data-points	R-square	Relative error	MSE	Reference
Stiffness tensor	Modeling parameters	3D spinodoid metamaterials	Multi-layer perceptron	19,170	0.999			[80]
Stiffness tensor	Modeling parameters	3D truss metamaterials	Multi-layer perceptron	3,000,000	0.986			[224]
Elastic modulus and relative density	Modeling parameters	2D honeycomb, square, and re-entrant star-shaped lattices	Multi-layer perceptron	53,000		0.05%		[227]
Stress-strain curve	16 binary representation of geometric infills	2D checkerboard-shape non-uniform cellular materials	Multi-layer perceptron	16,576			0.00031	[214]
Filter radius, volume fraction, and a design objective (maximum bulk modulus, maximum shear modulus, or minimum Poisson's ratio).	128 × 128 pixels	2D metamaterials	Variational autoencoders	25,000			0.009	[72]
Young's modulus and Poisson's ratio	256 × 256 pixels	2D auxetic metamaterials	Generative adversarial network	100,000			0.014	This work [62]
Relative density and Young's modulus	64 × 64 × 64 voxels	3D disordered voxelized lattices	3D Generative adversarial network	10,000			0.01	[zheng2022deep]

4.2 Materials Design Strategy by Conditional Generative Adversarial Network

The neural network architecture yields two main outputs, which are necessary for the inverse design of mechanical metamaterials: the modeling parameters, which can be used to generate geometries with additional modeling processes [80, 223, 224], and the geometries in the form of pixels or voxels [62, 72, 216, 225, 226]. The straightforward generation of geometries can speed up the inverse design process and help visualize geometries directly. The variational autoencoder (VAE) and GANs are the most commonly used neural network architectures for straightforward generation [216, 225, 226]. In the VAE, an encoder learns to represent input data (e.g., geometry or modeling parameters) efficiently, and a decoder tries to reconstruct the data using the internal representations and the learned weights, making it an ideal data compression engine. By contrast, the GAN is trained in an adversarial feedback loop to generate realistic geometries, wherein variational sampling is adopted to generate distinct geometries [62, 216]. Consequently, the GAN may be superior to the VAE in terms of the generation performance. We compare relevant studies using different network architectures for the inverse design of mechanical metamaterials in Table 4.1.

In this study, the inverse design of mechanical metamaterials was implemented using a novel deep learning framework, CGAN. A GAN, which consists of two models (a generator and discriminator), is a type of deep learning network for data generation [228–230]. The generator and discriminator are trained simultaneously by an adversarial process, in which the generator learns to produce data with characteristics similar to those of the training data, whereas the discriminator learns to distinguish between real data and the generated data. A CGAN is a type of GAN in which conditional generation is realized by taking advantage of labels during the training process. However, with regard to precise data generation, the conventional CGANs can hardly provide good guidance for training the generator because the discriminator always suffers from overfitting [231]. I addressed this problem by employing an independent module (solver). The solver is a linear regression network that acts as a linear elasticity solver to predict the Young's modulus and Poisson's ratio of a given pattern

(obtained from the dataset or generated by a CGAN). In this work, two CGANs (i.e., 2D-CGAN and 3D-CGAN) are harnessed for the inverse design of mechanical metamaterials. 2D-CGAN and 3D-CGAN share the similar network architecture; however, 2D-CGAN includes convolutional neural networks whereas 3D-CGAN includes volumetric convolutional neural networks.

The CGANs were trained to generate mechanical metamaterials from a probabilistic space with a given label (i.e., ν and E for 2D auxetic metamaterials, and ϕ and E for 3D architected materials in this work) by leveraging recent advances in GANs and convolutional neural network [230–233]. A CGAN comprised three modules, that is, a generator, discriminator, and solver, which were trained by an adversarial process. The generator learns to generate architectures that mimic the real architectures in the dataset. The discriminator learns to tell real architectures apart from fakes (generated by the generator), and thus helps the generator generate realistic architectures. The solver learns to predict the labels of the given architectures, and thus helps the generator spawn architectures with the desired target properties. A three-player game was conducted in which the generator deceived the discriminator in terms of geometry and simultaneously deceived the solver in terms of elastic moduli.

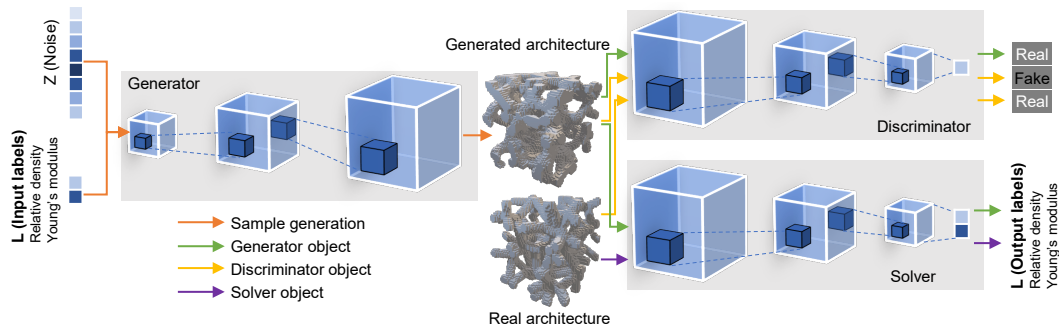


FIGURE 4.2: (a) Framework of 3D-CGAN comprising three modules: a generator, discriminator, and solver.

Figure 4.2 shows the framework of a CGAN — it is called 3D-CGAN used for the inverse design of 3D architected materials. The training process is based on supervised learning. While training, the generator progressively becomes better at creating architectures that look real and exhibit the desired target properties, whereas the discriminator becomes better at distinguishing real and fake architectures. The process attains equilibrium when the generator can perfectly deceive discriminator. The CGANs are capable of generating a batch of mechanical metamaterials for a given label (i.e., ν and E for 2D auxetic metamaterials, and ϕ and E for 3D architected materials in this work) after being trained using enough datapoints. Overall, the three primary advantages of the CGANs are as follows: first, compared with traditional heuristic criteria (e.g., the genetic algorithm), the use of an adversarial criterion speeds up the inverse design process and enables the generator to capture the object structure implicitly; second, the generator establishes the modeling process from a 1D probabilistic space to the 2D/3D space of objects, without the use of an additional modeling process; and third, the solver serves as an independent module that helps the discriminator avoid overfitting.

4.3 Inverse Design of 2D Auxetic Metamaterials

4.3.1 Dataset Preparation

As illustrated in Figure 4.3, 2D topology patterns were created using Voronoi tessellation, which is a robust method that is capable of creating various porous materials [63–68]. To ensure the periodicity of these 2D patterns, periodic boundary conditions were applied in the Voronoi tessellation. Briefly, a seed consisting of 64 coordinate points was initially created according to Mitchell’s best candidate algorithm [234]. A 2D Voronoi diagram was created based on the seed. To mimic the nature of actual auxetic foams, which have both convex and concave cells [235], the 2D Voronoi diagram was modified by merging two adjacent polygons. Finally, a new pattern was formed after smoothing the edges of the polygons using Chaikin’s algorithm because smooth surfaces have more homogeneous stress responses than sharp surfaces [141, 236]. Note that the relative density of a pattern can be tuned easily by changing the width of the edges. Here, the width was fixed for simplicity. The relative density of the patterns was approximately 0.154. By repeating this process, an infinite number of different patterns can be created to facilitate big-data-driven material design.

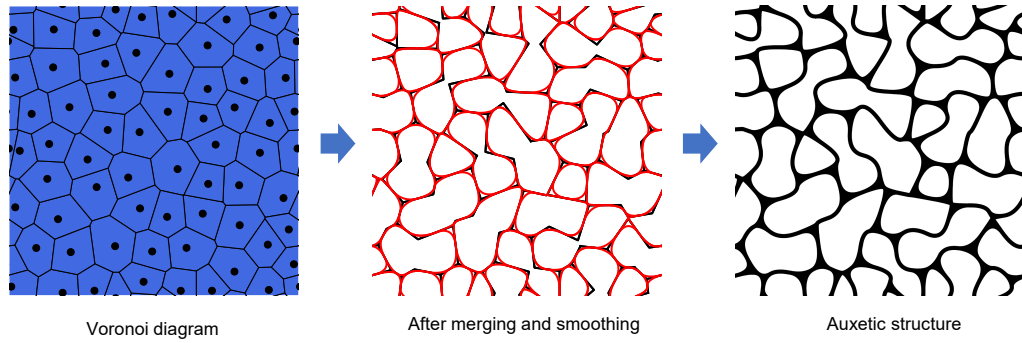


FIGURE 4.3: Process of structure generation for 2D auxetic metamaterials using Voronoi tessellation.

The elastic moduli (Young’s modulus and Poisson’s ratio) were calculated according to the theory of homogenization, which has been used extensively to probe the equivalent linear elasticity of periodic composites [39–41]. According to the theory of homogenization, the effective elasticity tensor \tilde{C}_{ijkl} of a periodic pattern can be computed as:

$$\tilde{C}_{ijkl} = \frac{1}{|V|} \int_V C_{pqrs} (\varepsilon_{pq}^{0(ij)} - \varepsilon_{pq}^{(ij)}) (\varepsilon_{rs}^{0(kl)} - \varepsilon_{rs}^{(kl)}) dV \quad (4.1)$$

where $|V|$ is the area of a square domain, C_{pqrs} is the locally varying stiffness tensor, $\varepsilon_{pq}^{0(ij)}$ represents the prescribed macroscopic strain fields (three strain fields in the case of two dimensions: horizontal, vertical, and shear strains), and $\varepsilon_{pq}^{(ij)}$ represents the locally varying strain fields and is defined as:

$$\varepsilon_{pq}^{(ij)} = \varepsilon_{pq}(\chi^{ij}) = \frac{1}{2} (\chi_{p,q}^{ij} + \chi_{q,p}^{ij}) \quad (4.2)$$

The locally varying strain fields are based on the displacement fields χ^{ij} , which can be determined using a prescribed macroscopic strain:

$$\int_V C_{ijpq} \varepsilon_{ij}(v) \varepsilon_{ij}(\chi^{kl}) dV = \int_V C_{ijpq} \varepsilon_{ij}(v) \varepsilon_{pq}^{0(kl)} dV, \forall v \in V \quad (4.3)$$

where v denotes the virtual displacement field. The numerical homogenization procedure is discussed in more detail in the literature [39–41]. After obtaining the effective elasticity tensor \tilde{C}_{ijkl} , the effective elastic moduli (i.e., Young’s modulus, Poisson’s ratio, shear modulus, and bulk modulus) can be calculated.

In this work, each pattern was first converted into a 256×256 element matrix consisting of 0 and 1, where 0 represents void regions and 1 represents solid regions. Subsequently, trial strain fields were applied to the element matrix to determine the reaction forces and stored elastic energy. Then, a homogenized elasticity tensor was obtained after the homogenization calculation. Finally, the effective elastic moduli of the patterns were calculated according to the elasticity tensor. The material model used in the homogenization was a linear elastic material with a Young’s modulus of 0.6615 MPa and a Poisson’s ratio of 0.49; these values were chosen to fit the equivalent elastic moduli of an incompressible neo-Hookean solid under a small deformation.

After topology creation and elastic modulus calculation, a large dataset was obtained, in which each datapoint consisted of a pattern and its corresponding labels (Poisson’s ratio and Young’s modulus). The training dataset was composed of 100,000 datapoints. Figure 4.4a shows the 100,000 randomly created geometric patterns in the property space with the axes representing the Poisson’s ratio (ν) and Young’s modulus (E). The randomly created patterns scattered in the material property space form a nearly triangular shape, with $2.1 \text{ kPa} < E < 13.7 \text{ kPa}$ and $-0.28 < \nu < 0.38$. I refer to the triangular region as the available E - ν space, in which random labels were sampled to train the neural network. Figure 4.4b shows the distributions of the Poisson’s ratios of these randomly created patterns. The distributions indicate that less than 3% of the randomly created patterns have negative Poisson’s ratios.

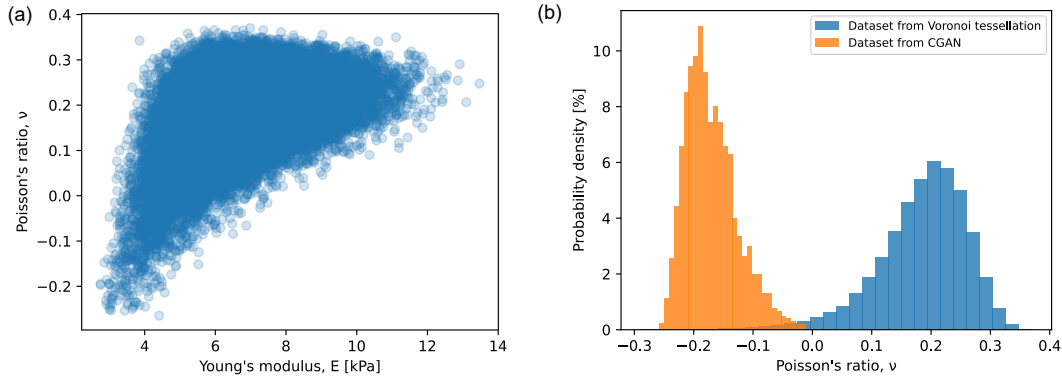


FIGURE 4.4: Dataset of 2D auxetic metamaterials for neural network training. (a) Young’s moduli and Poisson’s ratios of 100,000 randomly created patterns from Voronoi tessellation. (b) Distributions of Poisson’s ratios for randomly created patterns and for 2D-CGAN-outputted patterns with input condition of $\nu = -0.28$.

4.3.2 Neural Network Training

Figure 4.5a illustrates the architecture of the proposed 2D-CGAN. After the 2D-CGAN had been well trained using 100,000 datapoints, it could generate a batch of patterns for a given label (Young's modulus and Poisson's ratio). More details on the 2D-CGAN are discussed in Appendix C.1.

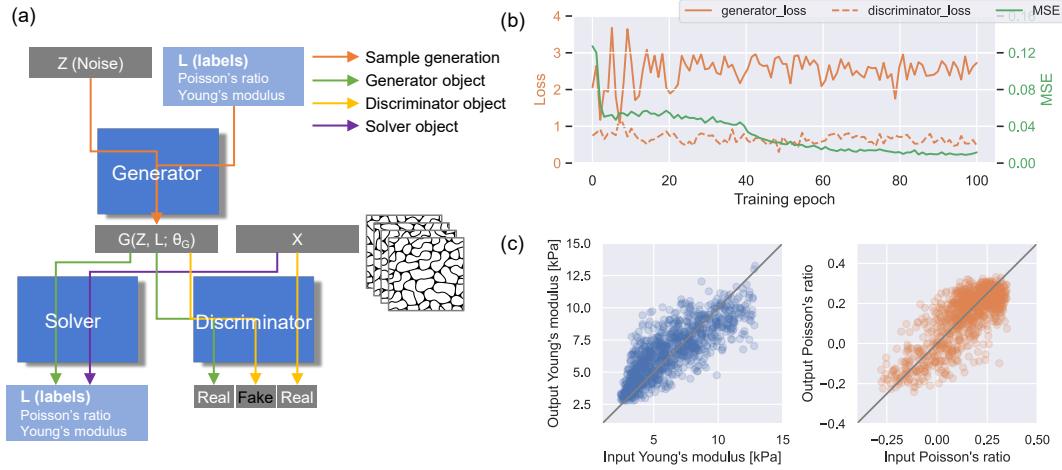


FIGURE 4.5: (a) 2D-CGAN architecture. (b) 2D-CGAN performance for different training datapoints. (c) Comparison between user-input and 2D-CGAN-output real elastic moduli.

I tested the performance of the 2D-CGAN model during each epoch by generating 1024 patterns with labels that were randomly sampled from the available E - ν space. The performance was evaluated in terms of the mean squared error (MSE) of the sum of E and ν :

$$\text{MSE} = \frac{1}{n} \sum_{k=1}^n ((E_k - \hat{E}_k)^2 + (\nu_k - \hat{\nu}_k)^2) \quad (4.4)$$

where $n = 1024$ is the number of labels sampled from the available E - ν space, E is the normalized input Young's modulus, \hat{E} is the normalized output Young's modulus, ν is the normalized input Poisson's ratio, and $\hat{\nu}$ is the normalized output Poisson's ratio. To facilitate deep learning, both the Young's modulus and Poisson's ratio were normalized to the range from 0 to 1 based on the maximum and minimum values of the E - ν space shown in Figure 4.4a. A smaller MSE indicates better performance. Figure 4.5b shows the change in the MSE during the training epoch. Two convergence stages are observed in the MSE curve. The first one is before epoch 5, where the solver learns very rapidly to generate patterns similar to the real patterns. The next stage is $5 < \text{epoch} < 50$, where the solver learns relatively slowly to generate patterns with the corresponding input elastic moduli. Initially, the MSE decreases rapidly; then, it decreases gradually, finally reaching a minimum approximately 0.014 after epoch 60. The low MSE indicates that the 2D-CGAN is capable of generating patterns with a user-defined Young's modulus and Poisson's ratio. In addition, the line plots for the loss (see Appendix C.1 for the definition) of the generator and discriminator are shown in Figure 4.5b. The plots represent typical loss-epoch graphs of a stable GAN training process: the losses of the generator and discriminator begin erratically and gradually

converge to a stable equilibrium after epoch 20. This finding further demonstrates the stability of the 2D-CGAN.

4.3.3 Inversely Generating 2D Auxetic Metamaterials

After the 2D-CGAN had been well trained using appropriate parameters, it could invert the design of auxetic metamaterials: a label (Young's modulus and Poisson's ratio) was input, and the 2D-CGAN generated a batch of geometrical patterns with the corresponding Young's modulus and Poisson's ratio. The performance of the trained 2D-CGAN was evaluated by comparing each input value and its output values (i.e., the Young's modulus and Poisson's ratio of the generated pattern). Figure 4.5c compares 1024 samples with input labels sampled from the available E - ν space. The coordinates of each point correspond to the input Young's modulus or Poisson's ratio (x coordinate) and the output Young's modulus or Poisson's ratio (y coordinate). A position closer to the bisection line ($y = x$) represents better performance of the 2D-CGAN. The narrow bandwidth of the scatter distributions indicates the good performance of the trained 2D-CGAN, demonstrating that the 2D-CGAN can generate a batch of geometries with user-desired Young's moduli and Poisson's ratios. These results also show that the 2D-CGAN can effectively perform extrapolation from the training data to provide a controllable inverse design, in contrast to the random generation obtained by Voronoi tessellation.

We further demonstrated that the trained 2D-CGAN facilitates the inverse design of auxetic metamaterials with very low negative Poisson's ratios. Considering that the lower boundary of the Poisson's ratio in the available E - ν space had $\nu = -0.28$ and $E = 3$ kPa, I input the label with these values and the 2D-CGAN generated a batch of auxetic metamaterials (Figure 4.6). In this figure, the input and output values are also compared below each pattern and show good agreement. Figure 4.4b compares the distribution of Poisson's ratios between the 2D-CGAN-generated patterns and randomly created patterns. The comparison shows that it is very easy to generate auxetic metamaterials with very low negative Poisson's ratios using the 2D-CGAN, in contrast to the random generation method, in which only a few metamaterials have negative Poisson's ratios. More importantly, this inverse design method does not require delicate arrangement of the shapes, distributions, and combinations of geometrical elements. This method is independent of prior knowledge about the design of auxetic metamaterials. More patterns generated by the 2D-CGAN with different elastic moduli are shown in Figures C.3 and C.4 in Appendix C.2.

4.3.4 Validation by Experiments and Simulations

To probe the auxetic behavior of the generated metamaterials under large deformation, I conducted a systematic analysis by performing uniaxial compression tests and FEM simulations. Figure 4.7 shows a typical 3D printed-sample and an example of meshing in FEM simulations. Figure 4.8a shows a sequence of progressively deformed shapes of the generated auxetic metamaterials under four different levels of compressive engineering strain. The experimental and simulation results show a consistent deformation tendency wherein the metamaterial gradually contracts when compressed uniaxially along with the shrinkage of its interior holes. The overall shrinkage phenomenon proves that the metamaterial is an auxetic metamaterial with a negative Poisson's ratio. The progressively deformed shapes of other patterns with Poisson's ratios ranging from -0.2 to 0.3 are shown in Figures C.4; the patterns with a positive Poisson's ratio expand laterally when compressed uniaxially.

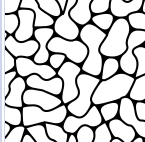

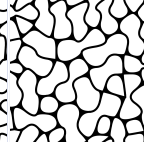


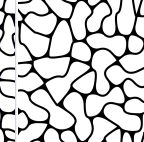
Patterns generated by CGAN						
ν_x (input)	-0.28	-0.28	-0.28	-0.28	-0.28	-0.28
ν_x (output)	-0.2455	-0.2064	-0.2368	-0.2308	-0.2531	-0.2612
ν_{xy} (FEM)	-0.2081	-0.2314	-0.2754	-0.2145	-0.2364	-0.2117
ν_{yz} (FEM)	-0.2294	-0.2501	-0.2138	-0.1622	-0.1801	-0.2293
E_x (input), [kPa]	3.0	3.0	3.0	3.0	3.0	3.0
E_x (output), [kPa]	3.2401	3.7556	2.9045	3.0699	3.4789	3.0145
E_{yy} (FEM), [kPa]	2.939	3.6765	4.7929	3.5423	3.6860	3.7501
E_{xx} (FEM), [kPa]	3.1494	3.9991	3.5593	4.3061	2.7287	4.0958

FIGURE 4.6: Inverse design using 2D-CGAN: Auxetic metamaterials generated using the 2D-CGAN with input labels of $E = 3$ kPa and $\nu = -0.28$.

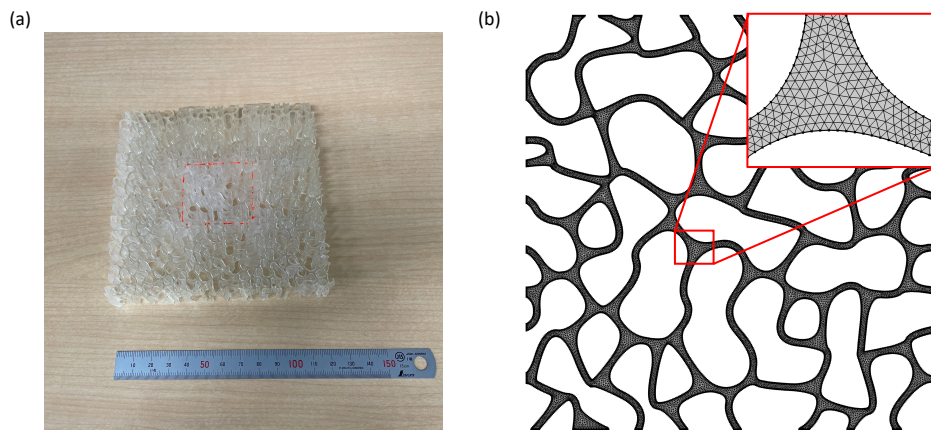


FIGURE 4.7: (a) A typical 3D printed-sample, and (b) an example of meshing in FEM simulations

Figure 4.8b presents a quantitative evaluation of Poisson's ratios under different compression strains. The engineering strains were determined from the average engineering strains of the innermost unit cell to reduce the influence of the boundary conditions. The figure shows that the calculated Poisson's ratios monotonically decrease with increasing strain ($\epsilon \leq 0.2$). A more detailed Poisson's ratio-strain curve obtained from the simulation results was also compared with the curve obtained from the experimental results. Initially, the Poisson's ratio decreases; then, it gradually increases during compression because the empty space is insufficient, which causes the ligaments to bend when they are in contact with each other. Overall, the experimental and simulation results demonstrate that the negative Poisson's ratio can maintain a wide range of compressive strain ($\epsilon = 0.2$). It is noteworthy that the limitation of maintaining a wider range of negative Poisson's ratio is a result of the training dataset, because the training structures used in this study are totally generated randomly. Therefore, to generate auxetic metamaterials that maintain stable Poisson's ratio throughout the large deformation process, a new dataset consisting of optimized structures is required in terms of deep learning.

I also analyzed the stresses of the auxetic metamaterials during deformation. As

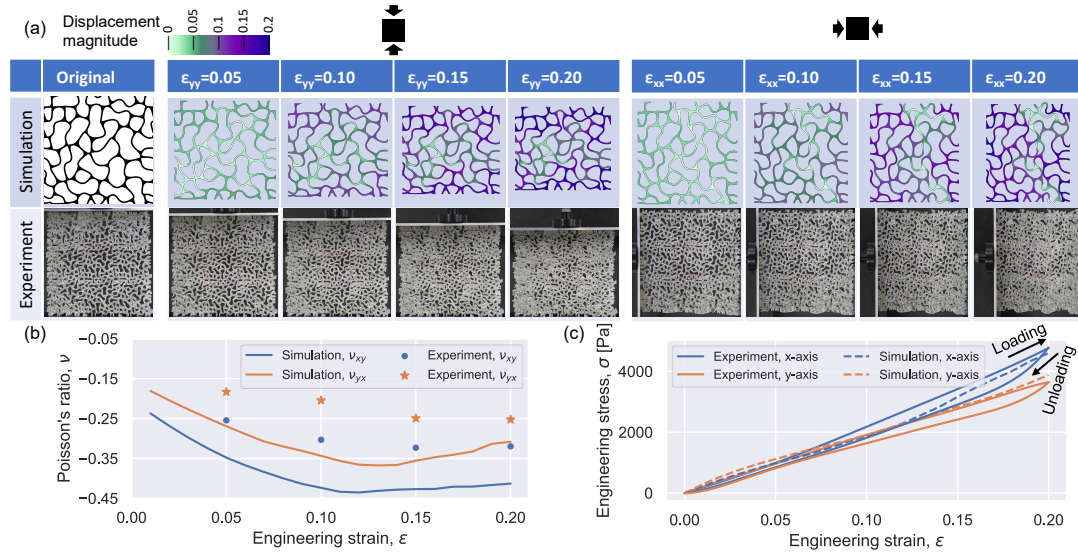


FIGURE 4.8: Auxetic behavior of structures. (a) Progressively deformed configurations of FEM model and 3D-printed sample under uniaxial compressive load. (b) Poisson's ratio-strain curves and (c) stress-strain curves from FEM simulations and uniaxial compression tests.

shown in Figure 4.8c, the stress-strain curves exhibit good linearity. The lack of transformation from the linear elastic region to the plateau region indicates that the auxetic behavior of the designed metamaterials is a result not of buckling, but rather of ligament bending. It is noteworthy that the designed auxetic metamaterials are considerably different from typical buckling-induced auxetic metamaterials, whose stress-strain curves have an additional plateau region between the linear elastic and densification regions [11, 47, 133, 163, 237–239].

4.4 Inverse Design of 3D Architected Materials

4.4.1 Dataset Preparation

Figure 4.9a shows the process of generating 3D Voronoi lattices for dataset preparation. First, a random seed of 27 3D coordinate points was created using Mitchell's best-candidate algorithm [234]. Note that the algorithm generates coordinate points with a regular distribution. Thereafter, a Voronoi diagram was plotted using Laguerre-Voronoi tessellation with a 3D periodic boundary condition. The periodic condition was implemented; the seeds were generated in $3 \times 3 \times 3$ unit cells, and the center unit cell was defined as an RVE. The same approach was employed for 2D design in our previous study [240]. The Voronoi skeleton was derived from the polyhedral meshes of the Voronoi diagram. It should be noted that nodal connectivity, which refers to the total number of ligaments connected to a node, has a considerable impact on the stiffness of architected materials [44]. For instance, ordered architected materials with nodal connectivities of 3, 4, 6, and 8 are significantly different in terms of their Young's modulus, yield strength, and Poisson's ratio [44]. A change in the nodal connectivity may result in an increase in the diversity of the Young's modulus for Voronoi lattices with the same relative density. Therefore, to extend the border of the available data space, 0–30% of the edges in the polyhedral meshes were deleted randomly to change

the nodal connectivity. Consequently, 30% was chosen to maintain the isotropy of the Voronoi lattices while extending the boundary of the available data space. It should be noted that if this value is too large, the Voronoi lattices will become anisotropic. Further, we ensured that the appearance frequency of each node was always greater than one to prevent single element connectivity when randomly deleting edges. Additionally, a periodic boundary condition was applied in this process to ensure the periodicity of the generated Voronoi lattices. Finally, a triply periodic Voronoi lattice was generated after a specific thickness was assigned to the edges of the polyhedral meshes. For deep learning, each Voronoi lattice was voxelized into a 3D voxel array (A_v) with a shape of $[64, 64, 64]$. To investigate the lower volume fraction applicability limit, the relative density of a Voronoi skeleton was reduced. The Voronoi skeleton was voxelized with decreasing relative densities, and the results revealed that the voxelized Voronoi lattice was discretized if the relative density was less than 0.045 (Figure 4.10a). The minimum relative density of the Voronoi lattices was set to 0.1. The modeling process was implemented using a Python code, and the Laguerre–Voronoi tessellation was based on the Python package MicroStructPy [241].

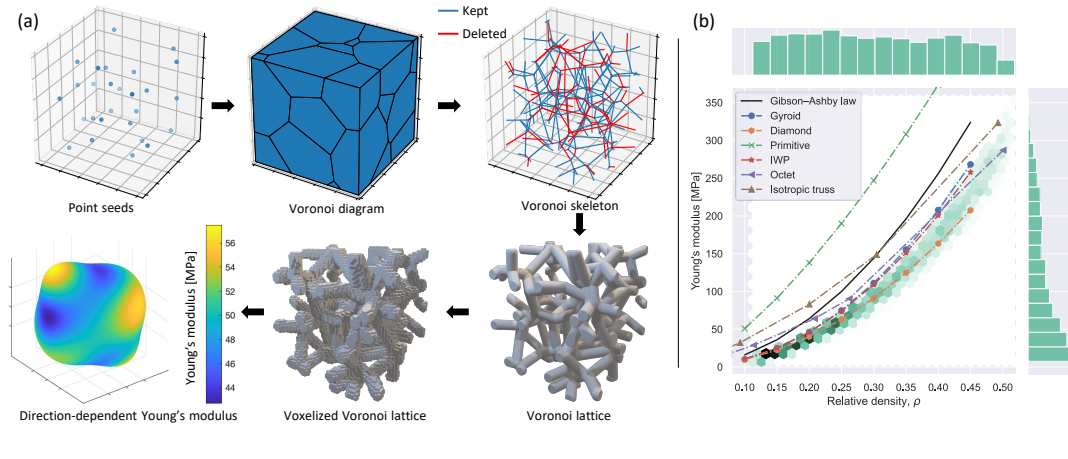


FIGURE 4.9: (a) Process of the dataset preparation: the geometry of a voxelized Voronoi lattice was generated by Voronoi tessellation and its Young's modulus was calculated using the homogenization method. (b) A dataset consisting of 10,000 datapoints where each datapoint was composed of a geometry (a 3D voxel array with a shape of $[64, 64, 64]$), its porosity, and Young's modulus. The dataspace was compared with several typical architected materials, including Gyroid, Schwarz Diamond, Schwarz Primitive, and Schoen IWP lattices, and octet and isotropic trusses [44, 207].

The Young's moduli of the generated 3D Voronoi lattices were calculated using a numerical homogenization method, as detailed in previous studies [40–42]. That is, the input argument was a 3D voxel array consisting of 0 and 1, where 1 indicates a solid, and 0 indicates a void. The Young's modulus and Poisson's ratio of the constitutive materials were set as 1.6 GPa and 0.23, respectively, corresponding to the material parameters of a 3D-printed resin. Periodic boundary conditions were then applied during the homogenization process. The homogenized constitutive matrix C^H could be solved by obtaining the element displacements and global displacement field, as follows:

$$C_{ij}^H = \frac{1}{|V|} \sum_{(e)} \int_{V^{(e)}} \left(\chi_{(e)}^{0(i)} - \chi_{(e)}^{(i)} \right)^T k_e \left(\chi_{(e)}^{0(j)} - \chi_{(e)}^{(j)} \right) dV^{(e)} \quad (4.5)$$

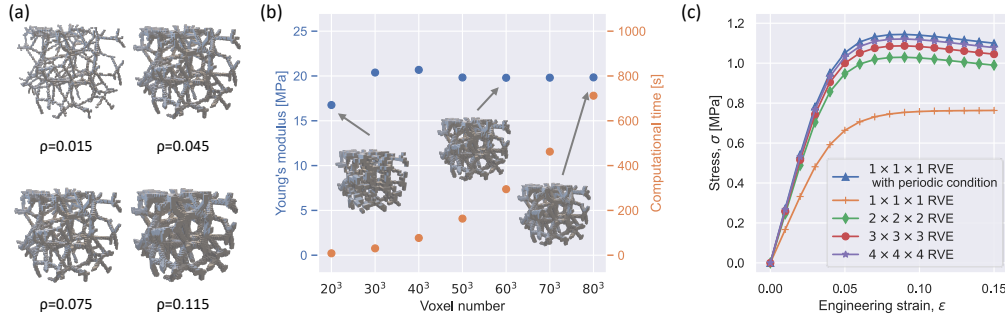


FIGURE 4.10: Assessing modeling, numerical homogenization algorithm, and FEM simulation. (a) Voxelizing Voronoi lattice with different relative densities. (b) Computational accuracy and cost of numerical homogenization algorithm. Voronoi lattice was voxelized into 3D voxel arrays with different shapes. (c) Impact of RVE size on the computational accuracy of FEM simulations. The Voronoi lattice was modeled with different RVE sizes, where $n \times n \times n$ RVE indicates an RVE consisting of $n \times n \times n$ unit cell numbers.

where $|V|$ denotes the total volume of the cube domain, $\chi_{(e)}^{0(i)}$ denotes the element displacement, $\chi_{(e)}^{(i)}$ denotes the displacement field obtained from the global stiffness equation, and k_e denotes the element stiffness matrix. Following iterations for all six load cases (three compressions along the x , y , and z axes, and three shearing loads), the effective 6×6 elasticity matrix C^H was obtained. The directional dependence of the Young's modulus of a typical Voronoi lattice is shown in Figure 4.9a, where the shape of the surface contour is close to a sphere, thus indicating the approximate isotropic stiffness of the Voronoi lattice. Consequently, the effective Young's modulus can be obtained using isotropic approximation, where the complete 6×6 elasticity matrix is matched with the matrix for the isotropic symmetry class. It should be noted that the effective Poisson's ratio can also be calculated using the elasticity matrix. The accuracy of the Poisson's ratio is computed using the numerical homogenization method adopted in our previous study [10]. Because the Voronoi lattices were approximated as voxel arrays rather than beam-based architected materials, we conducted a convergence study according to the number of voxels and computational cost. A Voronoi lattice ($\rho = 0.115$) was voxelized into 3D voxel arrays with different shape from $[20, 20, 20]$ to $[80, 80, 80]$. The Young's moduli of such 3D voxel arrays were calculated using the numerical homogenization method. A comparison of the calculated Young's moduli and computational cost is presented in Figure 4.10b. From the figure, it can be observed that the Young's modulus converges with an increase in the number of voxels, and the value remains constant when the number of voxels is greater than $[50, 50, 50]$. Further, the computational cost (code execution time on a MacBook with M1 chip) increases exponentially with an increase in the number of voxels. Therefore, with regard to the computational accuracy and cost, Voronoi lattices were voxelized into 3D voxel arrays with a shape of $[64, 64, 64]$, which corresponds to 64^3 eight-node hexahedral elements in the numerical homogenization method.

The relative density (ρ) refers to the proportion of the solid part in a Voronoi lattice and can be calculated as follows:

$$\rho = \frac{\sum A_v}{64^3} \quad (4.6)$$

Figure 4.9b shows the data space of material properties for 10,000 generated Voronoi lattices in terms of the ρ – E relationship, where the darker region indicates a higher concentration of datapoints. The material property space was compared with that of typical architected materials [44, 207]. Notably, the relationship between ρ – E does not follow the classical scaling laws of the Gibson–Ashby model ($E^*/E_0 = a\rho^b$, where E^* denotes the effective Young’s modulus, E_0 denotes the Young’s modulus of the constituent material, and a and b are constants) [41]. By contrast, the data space of ρ and E covers a wider range, exhibiting a ribbon pattern. This implies that neural networks can be trained to generate Voronoi lattices with corresponding properties inside the ribbon-shaped data space. Overall, the training dataset comprises 10,000 datapoints, where each datapoint consists of a Voronoi lattice and its corresponding ρ and E .

In the numerical homogenization method, numerous unit cells are considered based on a mathematical operation [153]. However, the number of unit cells is limited in an experimental validation. Therefore, the impact of the number of RVE units on the stress–strain curve at finite strain was investigated for a detailed comparison with the corresponding experiment, as shown in Figure 4.10c. The results are discussed in Section 4.6.2.

4.4.2 Neural Network Training

The detailed information of the 3D-CGAN is discussed in Appendix D. Here, similarity refers to the agreement between input labels (targets ρ and E) and output labels (ρ and E of the generated structures). We evaluated the similarity using a risk function, that is, the mean squared error (MSE) of the sum of ρ and E :

$$\text{MSE} = \frac{1}{n} \sum_{i=1}^n \left((\rho_i - \hat{\rho}_i)^2 + (E_i - \hat{E}_i)^2 \right) \quad (4.7)$$

where n denotes the total number of labels sampled from the available ρ – E data space. To reduce the error, n was set to 1024 at each generation. ρ denotes the input relative density, $\hat{\rho}$ denotes the output relative density, E denotes the input Young’s modulus, and \hat{E} denotes the output Young’s modulus. To stabilize the training process, the relative density and Young’s modulus were normalized to the range 0–1. A smaller MSE indicates better similarity between the input and output labels, as well as better performance of the 3D-GAN.

The stability refers to a stable training process. In the 3D-CGAN, the generator and discriminator models were trained simultaneously, with the goal of finding a Nash equilibrium between the two models. Consequently, the training process aims to find an equilibrium between two forces rather than a minimum. The stability can be quantitatively evaluated in terms of the discriminator and generator losses (see Appendix A for the definition).

Figure 4.11a displays the MSE and loss versus the training epoch using 10,000 datapoints. The MSE curve consists of two stages: the MSE decreases initially before gradually converging and finally attains a minimum at approximately 0.01 after epoch 50. This shows that the 3D-CGAN can be trained to converge after finite epochs. The low value of the MSE shows that the trained 3D-CGAN has learned to generate Voronoi lattices with a target ρ and E . The loss curves show the typical pattern of a reliable GAN training procedure, that is, both losses are slightly erratic early in the run before stabilizing after approximately 50 epochs. The losses converge to a stable equilibrium,

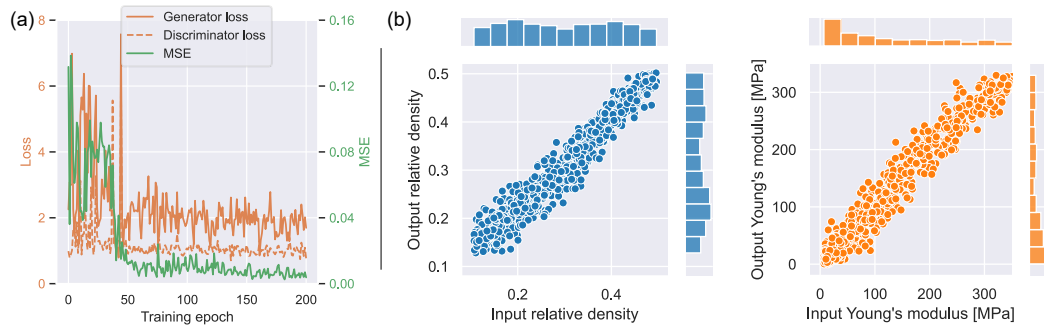


FIGURE 4.11: Training results of 3D-CGAN: (a) Generator loss, discriminator loss, and mean square error against training epoch. (c) User-input against 3D-CGAN-output values in terms of relative density and Young's modulus.

proving the stability of the training process. The convergence of the MSE and losses demonstrates the robustness of the 3D-CGAN and the stability of the training process.

4.4.3 Inversely Generating 3D Architected Materials

Given that the training results were robust and stable, we managed to exploit the trained 3D-CGAN for the controllable generation of Voronoi lattices. The inverse design adhered to the following procedure: the 3D-CGAN received a label (ρ and E) and then yielded several voxelized Voronoi lattices with the target ρ and E . To demonstrate the flexibility of the trained 3D-CGAN, Voronoi lattices were generated with target labels randomly selected from the ρ - E data space. Figure 4.11b compares the input labels (targets ρ and E) and output labels (ρ and E of the generated structures) of 1024 randomly generated Voronoi lattices. Each coordinate of the scatter corresponds to an input ρ or E and the output ρ or E . The difference between the input and output labels can be evaluated by linearly fitting these scatters ($X = Y$). As shown in Figure 4.11b, these scatters converge to the bisection line, forming a narrow region. A comparison of the distributions for the user-input and 3D-CGAN-output values is presented in Figure 4.11b. The mean values of the user-input and 3D-CGAN-output relative densities are 0.3068 and 0.3165, and the variances of the user-input and 3D-CGAN-output relative densities are 0.0132 and 0.0123, respectively. The mean values of the user-input and CGAN-output Young's moduli are 125.1 and 123.5 MPa, and the variances of the user-input and CGAN-output Young's moduli are 10332 and 10117 MPa, respectively. This indicates that the trained 3D-CGAN has learned to generate Voronoi lattices with the target ρ and E . In addition, these results also prove the successful implementation of controllable inverse design, making it different from the forward design method, where Voronoi lattices are generated by Voronoi tessellation without assigned ρ and E .

To explore the capability and applicability of the 3D-CGAN, we compared the data spaces of the real Voronoi lattices with those of the 3D-CGAN-generated Voronoi lattices in the relative density-Young's modulus relationship map in Figure 4.12. We first input the target properties inside the data space of the real Voronoi lattices to the 3D-CGAN, and we then plotted the properties of the 3D-CGAN-generated Voronoi lattices in Figure 4.12. The data space of the real Voronoi lattices refers to the ribbon region in the relative density-Young's modulus relationship map in Figure 4.9b. It can

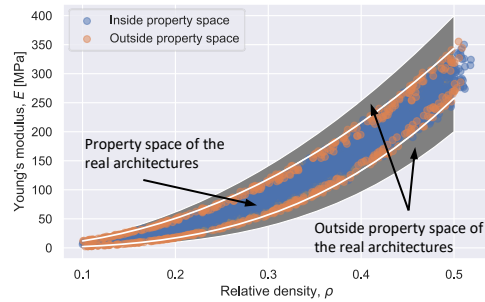


FIGURE 4.12: Properties of 3D-CGAN-generated Voronoi lattices covering relative density–Young’s modulus relationship map. Blue dots represent properties of 3D-CGAN-generated Voronoi lattices that were generated by inputting target properties within the data space, and orange dots represent those generated by inputting target properties outside data space.

be observed that the properties of the 3D-CGAN-generated Voronoi lattices may occupy a considerable data space, further demonstrating that the 3D-CGAN possesses the ability to generate Voronoi lattices with properties akin to the dataset. To explore the capability of generating Voronoi lattices with properties outside the dataset, we tried to input target properties outside the data space of the real Voronoi lattices. The results revealed that the trained 3D-CGAN could barely generate Voronoi lattices with properties outside the data space but approaching the border of the property space, as shown in Figure 4.12. This can be attributed to the training target of the 3D-CGAN: the 3D-CGAN was trained to ensure that it can learn to generate Voronoi lattices that not only look real but also possess the target properties. To achieve the target properties, the 3D-CGAN learned to deceive the solver that was initially trained with the data space of the real Voronoi lattices. Consequently, it was difficult for the 3D-CGAN to generate Voronoi lattices in the whitespace beyond the data space.

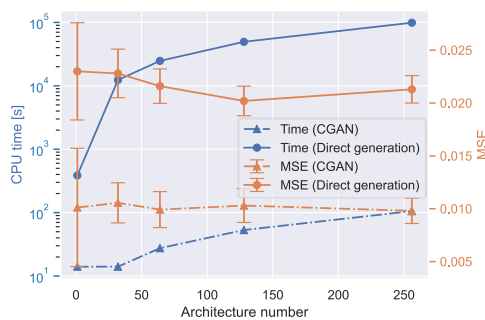


FIGURE 4.13: Computational cost and accuracy of inverse design using 3D-CGAN and forward design. The computational cost was determined using CPU time of code execution, and accuracy was measured using the MSE based on target property and the property of generated geometries

To demonstrate the benefits of the 3D-CGAN in terms of the computational cost and accuracy, we compared the generation processes of the inverse and forward designs. The inverse design was implemented using the trained 3D-CGAN to generate

a given number of geometries with a target property ($\rho = 0.3$ and $E = 90$ MPa). The code execution time was recorded according to the computational cost. For the forward design, it is clear that one can directly generate a large number of geometries using Voronoi tessellation and obtain their properties, after which they can select the desired geometries with target properties. The computational cost of the forward design was determined using the code execution time required to run the Voronoi tessellation and numerical homogenization. All codes were run on a MacBook with an M1 chip. Figure 4.13 provides a comparison of the computational costs between the inverse and forward designs. The results indicate that the time required to execute the forward design on a central processing unit (CPU) is greater than that required for an inverse design based on the trained 3D-CGAN by a factor of 1000. For example, approximately 5×10^4 s are required to generate 128 Voronoi lattices 3D-CGAN using the forward design but only 53 s using the 3D-CGAN, which is significantly faster than that required to generate optimized 3D geometries using solid isotropic material with penalization topology optimization [242, 243]. It is clear that topology optimization can generate an optimized 2D geometry in a short time. However, a longer time is required to generate a batch of optimized 3D geometries using topology optimization than that required by the 3D-CGAN [244]. In addition, when multiple constraints (e.g., Young's modulus, Poisson's ratio, yield strength, and relative density) are required in topology optimization, the computational cost may be rapidly increased. However, the time barely changes for the 3D-CGAN because only the labels of the training dataset are to be replaced. We also calculated the MSE using the target property and the property of the generated geometries. The results show that the MSE of the 3D-CGAN-generated lattices is approximately 0.1, which is better than that for the forward design of randomly direct generation (around 0.21) (Figure 4.13).

To visualize the training results clearly, we provide a comparison of several real Voronoi lattices (generated using Voronoi tessellation) and 3D-CGAN-generated Voronoi lattices in Figure 4.14. Similar to real Voronoi lattices, these voxelized Voronoi lattices have a ligament-channel bicontinuous network. Additionally, the input and output relative densities and Young's moduli are in good agreement, further demonstrating that the 3D-CGAN can generate Voronoi lattices with the target ρ and E . It should be noted that a few isolated voxel clusters may be found in some 3D-CGAN-generated Voronoi lattices, owing to the transposed convolution layers in the generator that are provided with random noise as an input. These isolated voxel clusters can be removed by filtering the isolated voxels after generation. The 3D-CGAN is trained in an adversarial feedback loop to generate realistic geometries, which indicates that the 3D-CGAN-generated Voronoi lattices appear realistic. As the 3D-CGAN-generated Voronoi lattices are generated from random noise, these Voronoi lattices are similar but distinct from the real geometries and themselves. In addition, for bone implant application, we smoothed the surface of the generated Voronoi lattices using the non-uniform rational mesh smooth (NURMS) method (Figure 4.14).

4.4.4 Validation by Experiments and Simulations

I further validated the mechanical properties and deformation behaviors of the 3D-CGAN generated architectures using uniaxial compression tests. Figure 4.15 shows a gallery of 3D-printed samples and a representative mesh used in FEM simulations. Figure 4.16a displays a generated architecture after surface smoothing, showing a gradual deformation under progressive compression strain. This suggests that some local fractures appeared under compressive loading (the red circles in Figure 4.16a). The ligament crack can be attributed to the local stress concentration owing to the

Real Voronoi lattices (from dataset)					
3D-CGAN-generated Voronoi lattices (voxelized)					
After NURMS process (smoothed)					
Relative density (input)	0.1	0.2	0.3	0.4	0.5
Relative density (output)	0.1109	0.2097	0.3043	0.4052	0.4899
Young's modulus (input), [MPa]	5	30	70	160	250
Young's modulus (output), [MPa]	5.438	31.32	73.12	167.3	246.8
Young's modulus (voxelized samples of experiments), [MPa]	5.912	23.13	83.12	176.1	283.6
Young's modulus (smoothed samples of experiments), [MPa]	6.351	25.31	84.13	177.8	284.1
Young's modulus (simulation), [MPa]	4.555	26.47	68.34	163.0	242.0

FIGURE 4.14: 3D-CGAN generated Voronoi lattices with different relative densities and Young's moduli before and after surface smoothing. The relative densities and Young's moduli were validated through experiments and simulations.

geometrical irregularity and brittleness of the 3D-printed resin. These local fractures contribute to the sudden drop in the stress–strain curve from the experimental compressive test (Figure 4.16b). This result suggests that the 3D-printed resin is not a suitable material for applications in scaffolds because of its brittleness, which is one of the reasons why many bone implants are fabricated with alloys [26, 209, 245, 246].

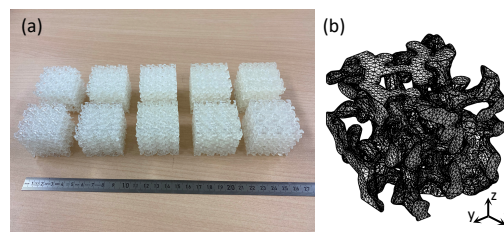


FIGURE 4.15: (a) Representative 3D-printed samples before (top) and after (bottom) surface smoothing. (b) A representative mesh used in FEM simulations.

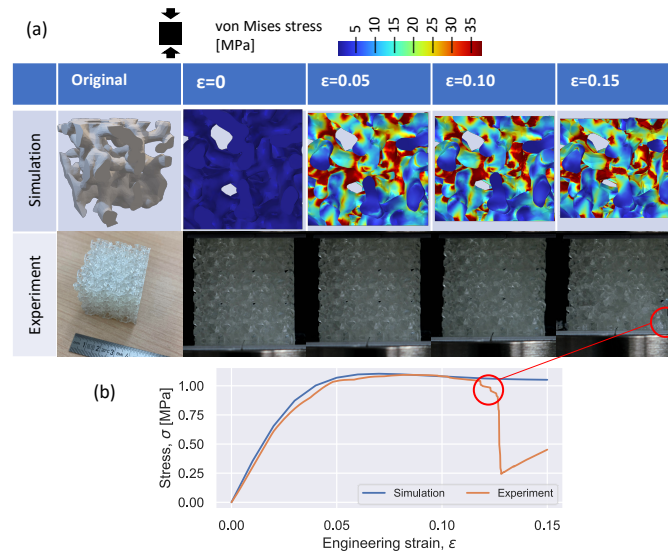


FIGURE 4.16: Deformation behavior of a 3D-CGAN generated architecture. (a) FEM simulation and experimental results of the architecture deforming under increasing compressive strain. (b) stress–strain curves from FEM simulations and uniaxial compression tests. The sudden drop of stress during compression attributes to the local fractures appearing in the 3D-printed sample.

However, the aim of using 3D-printed resin in this study was to validate the stiffness. Consequently, the Young’s modulus of each sample was calculated from the linear elastic region of the stress–strain curves. The 3D-CGAN generated architectures before and after the NURMS smoothing process were prepared and evaluated using compression tests. The calculated Young’s moduli of these samples are compared in Figure 4.14. Although the sample becomes slightly stiffer after surface smoothing (no more than 10%), the Young’s moduli calculated from the linear elastic regions showed a significant agreement with the target values, demonstrating the accuracy of the trained 3D-CGAN (Figure 4.14). The results prove that the NURMS method can be combined with deep learning to generate smoothed geometries with target stiffness.

The mechanical properties were validated using FEM simulations. Compared with a 3D-printed sample consisting of $3 \times 3 \times 3$ unit cells, the geometry in the FEM simulation possessed only one unit cell because of the application of periodic conditions. Figure 4.16a shows the progressively deformed configurations of the smoothed architecture. This demonstrates that the stress is concentrated in the middle regions of the ligaments, as well as the contact region of the surfaces. Moreover, based on a comparison between the experimental and simulation results, the stress–strain curves in the linear elastic region showed a significant agreement, demonstrating that the use of FEM simulations was a robust approach to predict the stiffness of such architectures. Additionally, it is striking that the Young’s moduli from the experimental and simulation results were close to the target values, further proving that the trained 3D-CGAN possesses a powerful capacity for the inverse design of architected cellular materials.

4.5 Summary

I developed a deep learning framework for the inverse design of 2D auxetic metamaterials and 3D architected cellular materials, respectively. Two neural networks (2D-CGAN for 2D auxetic metamaterials, and 3D-CGAN for 3D architected cellular materials) were trained using architectures generated by Voronoi tessellation and their labels, based on supervised learning. The trained neural networks were capable of rapidly generating mechanical metamaterials with the desired target relative density, Young's modulus, and Poisson's ratio. This study opens new avenues to harness deep learning in the realization of user-desired properties for applications in which specific material properties are required (e.g., actuator fabrication, sensor manufacturing, and catalysis). In addition, this study demonstrates the potential application of architecture cellular materials toward tissue engineering, where artificial scaffolds can be inversely generated using a given target relative density and Young's modulus. I expect this work to be extended to the inverse design of mechanical metamaterials with other target properties by replacing the labels—for example, diffusivity, permeability, and conductivity—for the sake of energy storage and conservation [63, 247, 248]. Finally, although I only focused on a typical geometry (irregular geometries created by Voronoi tessellation) in this work, it has the potential to combine other geometries created using other methods, such as triply periodic minimal surfaces, spinodal architectures, and foams [66, 208, 212], to enable the inverse design of architected cellular materials inside and outside the material property space [249].

4.6 Methods

4.6.1 Uniaxial Compression Tests

The auxetic behaviors of the generated metamaterials were first investigated using a set of 3D-printed samples in uniaxial compression tests. Each sample consisted of 3×3 unit cells and had overall dimensions of $120 \text{ mm} \times 120 \text{ mm} \times 15 \text{ mm}$. The unit cell number and size are sufficient to represent a periodic porous material [44]. To ensure that the specimens underwent large deformation without cracks, they were fabricated using an elastic photopolymer resin (Elastic 50A resin, Formlabs, USA) by employing a 3D printer (Form 3, Formlabs, USA). A subtle surface finish was achieved without the use of support structures. The printing parameters were as follows: a layer thickness of 0.05 mm and an operation temperature of $33 \text{ }^\circ\text{C}$. All the specimens were fully cured at $60 \text{ }^\circ\text{C}$ for 20 min after washing with isopropanol. A typical 3D-printed sample is shown in Figure 4.7a.

The mechanical properties of the 3D-printed specimens were investigated by performing static compression tests using a motorized test stand (EMX-500N, IMADA, Japan). A constant displacement rate of 10 mm/min was set during the tests, in which the samples were uniaxially compressed between two plates. The deformation process was captured using a high-speed camera, and the stress–strain curves were plotted using the recorded load–displacement data. The Hencky (logarithmic) strain components of the longitudinal (compression) and transverse directions were calculated using

$$\epsilon_i = \ln \left[1 + \frac{\bar{u}_i}{L_i} \right] = \ln [1 + \epsilon_i] \quad \text{for } i \in \{l, t\}, \quad (4.8)$$

where \bar{u}_i is the average boundary displacement between the top and bottom or the left and right of the red-marked interior unit cell, and L_i is the initial length of the interior unit cell. In this study, $L_l = L_t = 40$ mm. The average boundary displacements of the interior unit cell were measured by post-processing the recorded movies. Using the Hencky strain, Poisson's ratio at finite strain was defined as $\nu_{lt} = -\epsilon_t/\epsilon_l$.

The Young's modulus E_l for the longitudinal (compression) direction was calculated by linear fitting of the initial linear portions of the stress–strain curves. Least-squares approach was used to find the suitable value of E_l , in which the optimization problem was defined as

$$\min \left[\sum_{k=1}^N \left(\frac{F^{(k)}}{A} - \epsilon^{(k)} E_l \right)^2 \right], \quad (4.9)$$

where N is number of data, F is the applied load, and A is the initial contact area between the sample and the measuring instrument. In this study, the initial contact area was calculated as $A = 1,800 \text{ mm}^2$ ($120 \text{ mm} \times 15 \text{ mm}$). Compression tests were carried out on the structure in two directions, namely, x and y , as shown in Figure 4.7b; that is, ν_{xy} , ν_{yx} , E_x , and E_y were evaluated.

The mechanical properties of 3D-CGAN generated architected materials were also investigated using uniaxial compression tests. To obtain the stiffness of these generated architected materials, 3D printing technology is ideal, which allows the fabrication of such complex models. To print models without supporting components, while providing a smooth surface finishing, I used a stereolithography 3D printer (Form 3, Formlabs, USA) with a photopolymer resin (Clear Resin, Formlabs, USA). The photopolymer resin is a typical plastic material with a Young's modulus, Poisson's ratio, and yield strength of 1.6 GPa, 0.23, and 38 MPa, respectively [250]. The 3D-printed models were of dimensions $40 \text{ mm} \times 40 \text{ mm} \times 40 \text{ mm}$ and comprised a representative volume element (RVE) of 3×3 unit cells, which were selected to represent such types of periodic porous materials in terms of mechanical testing [44]. These models were exported as standard tessellation language (STL) format files and then sliced through PreForm before being sent for 3D printing. The printing parameters were set as follows: layer thickness of 0.05 mm, operating temperature of $33 \text{ }^\circ\text{C}$, and without the use of support structures. To remove residual resin on the surface, these samples were washed with isopropanol after 3D printing. Thereafter, post-curing process was implemented on these samples at $60 \text{ }^\circ\text{C}$ for 30 min using Form Cure (Formlabs, USA). Figure 4.12a shows representative 3D-printed samples before and after surface smoothing.

After 3D-printing fabrication, the mechanical properties of these samples were examined through uniaxial compression tests using a motorized test stand (AGXplus-10kN, Shimadzu, Japan). The static compression tests were performed at a vertically constant speed of 10 mm/min , following the ASTM standard D695-15. The compression strain was set to 0.15, which is sufficient to obtain the elastic deformation of these samples. The deformation processes were recorded by a high-speed camera in front of the samples. The effective Young's moduli were calculated by linearly fitting the initial linear region of the recorded stress–strain curves.

4.6.2 Finite Elements Method Simulations

The mechanical properties of the proposed patterns were further validated using an FEM simulation platform (COMSOL Multiphysics Ver. 5.4, COMSOL, Sweden). A 2D

plane strain model was utilized under periodic boundary conditions for the simulations of 2D auxetic metamaterials. To mimic the properties of the 3D-printed material, the material model in the simulations was defined as an incompressible neo-Hookean model with a Young's modulus of 0.6615 MPa that was fitted from the compression tests. All the model geometries were meshed using approximately 2.5×10^5 second-order triangular solid elements. An example of meshing is shown in Figure 4.7b. A contact condition based on an augmented Lagrangian method was set in the finite element model. For the large deformation, a parametric sweep of the longitudinal displacement was used with a stop condition of $\varepsilon_l = 0.2$. The Poisson's ratios and Young's moduli in the simulation results were calculated using the same method that was employed to obtain the experimental results.

For the simulations of 3D architected materials, A 3D strain model was utilized under periodic boundary conditions. The constitutive model was a plastic material model with a Young's modulus, Poisson's ratio, and yield strength of 1.6 GPa, 0.23, and 38 MPa, respectively, corresponding to the mechanical properties of the clear resin used in the experiments. Nonlinear uniaxial compression simulations were performed with periodic boundary conditions, accompanied by a parametric sweep in the z-axis displacement. The stop condition was set when the compression strain attained 0.15. The models were built using approximately 3×10^5 second-order tetrahedral solid elements, and a typical meshed model is shown in Figure 4.12b. The effective Young's moduli were also extracted from the stress-strain curves.

In the experiments, uniaxial compression deformation was imposed onto the 3D-printed samples composed of $3 \times 3 \times 3$ RVE units. To verify the feasibility of the experiments, the impact of the number of RVE units was investigated. Here, we computed the large deformation behavior of a Voronoi lattice (the same Voronoi lattice in Figure 4.10b with a voxel array of [64, 64, 64]) in the uniaxial compression test according to different number of RVE units using FEM simulations. The stress-strain curves derived from the FEM simulations are shown in Figure 4.10c. The figure shows that the stress-strain curves converge as the size of the RVE increases. It should be noted that the stress-strain curve of a $1 \times 1 \times 1$ RVE with periodic condition fits with those for larger RVE sizes (e.g., $3 \times 3 \times 3$), demonstrating that the experiments correspond to numerical simulations of an RVE with periodic conditions.

Chapter 5

Conclusions and Outlook

5.1 Conclusions

In conclusion, the state-of-the-art computational design methods have been harnessed to design mechanical metamaterials in this thesis. Additive manufacturing, along with post-processing and a synthesized functional material, has been utilized to fabricate the designed mechanical metamaterials with enhanced properties and novel functionality.

In Chapter 2, a mathematical modeling method was proposed to simplify the conventional modeling methods. The mathematical modeling method was implemented using MATLAB codes that can generate a 3D auxetic metamaterial with optimal mechanical properties using an implicit function. The 3D auxetic metamaterial was fabricated using 3D printing with a rubber-like material. The compression tests, along with the FEM simulations, demonstrate that the auxetic behavior of the new metamaterial is dominated by buckling instability and is retained over a broad range of longitudinal strain values up to 0.3. Furthermore, a nickel layer was then plated onto the surface of 3D-printed specimens to enhance its stiffness, strength, and conductivity without loss of auxeticity and resilience. The integration of 3D printing and electroless plating enabled accurate control over the mechanical and conduction properties of the auxetic metamaterial; these properties are presented as contour maps for guidance in functional applications.

In Chapter 3, a new functionality, reprogrammability, was proposed to make the mechanical responses of mechanical metamaterials changeable. The reprogrammability was achieved by developing a SM-PDMS, a rubber-like functional material with shape-memory and photothermal effects. The reprogrammability was implemented on three mechanical metamaterials made of SM-PDMS, whose mechanical responses can be switched using local light stimulation. An application was demonstrated using a soft actuator that shows reprogrammable preferred locomotion direction. The SM-PDMS has a potential to be applied in DIW 3D printing techniques to enable fabricate more complex architectures.

In Chapter 4, inverse design was proposed to convert the conventional forward design approach. The inverse design was implemented with a deep learning framework using CGANs, i.e., 2D-CGAN and 3D-CGAN. The 2D-CGAN and 3D-CGAN are capable of inversely generating 2D auxetic metamaterials and 3D architected materials, respectively, with a given target label (i.e., the properties of desired architectures). The deep learning frameworks have a potential for the inverse design of other mechanical metamaterials with other target properties by replacing the labels, for example, diffusivity, permeability, and conductivity.

5.2 Outlook

From the aspect of design, inverse design has gained great attention because it converts the conventional forward design approach and gets rid of the experienced designers and extensive trial-and-error efforts. Recent advances in artificial intelligence enable the inverse design of mechanical metamaterials with target properties. It is encouraged to prepare datasets composed of different architectures and their corresponding properties to extend the inverse design space of mechanical metamaterials. Further, the booming artificial intelligence techniques, along with bigger and better datasets, pave an way to achieve self learning of mechanical metamaterials: a artificial intelligence can recognize patterns of mechanical metamaterials, learn from data, become more intelligent over time, and finally generate novel mechanical metamaterial by itself. This is similar to the formation of natural microstructures in creatures.

Regarding fabrication, the straightforward way is additive manufacturing. In particular, 4D printing, combining 3D printing and smart materials, enables designing mechanical metamaterials from not only architectures but also constitutive materials. The properties of stimulus-responsive materials have a potential to enhance and even change the deformation mechanism, actuation method, shape-shifting speed, etc. of 4D-printed mechanical metamaterials. Therefore, the additional degree of freedom opens a door to design mechanical metamaterials with unprecedented properties.

As mechanical metamaterials become more sophisticated and autonomous, could they display any degree of materials intelligence? Recently, several unconventional computing approaches have been realized using mechanical metamaterials to augment traditional electronic computing by interacting with and adapting to their environment [251]. For example, mechanical metamaterials with mechanical logic gates can perform logic operations by encoding mechanical [252, 253], chemical [254], electrical [255], and pneumatic [256] inputs. Beyond binary abstraction, what if mechanical metamaterials eventually evolve to be neuromorphic to mimic neuro-biological architectures present in the nervous system. Mechanical metamaterials are conducive to neuromorphism in terms of three features: hierarchical connectivity, weighted coupling of every nodal pair, and response to their environment [257, 258]. For example, a 3D-waveguide architecture of photonic interconnects made of 2PP have been demonstrated with an unreported size hosting 225 input and 529 output channels within a footprint area of only $0.46 \times 0.46 \text{ mm}^2$ [259]. The 3D-waveguide architecture can implement nine spatial filters with a Haar convolution kernel of stride and width three, which represents a fundamental operation of deep convolutional neural network. Thereafter, the combination of 4D printing and artificial intelligence could potentially provide an idealized framework to create mechanical metamaterials systems for neuromorphic computing.

Appendix B

Buckling Analysis of a Hybrid Beam

A nonlinear buckling analysis was proposed to determine a suitable beam slenderness ratio (height to width ratio, h/w). The entire beam can be considered as a soft-rigid hybrid beam consisting of two bonded beams because half of the beam becomes softer after local stimulation. The theory of a beam on an elastic foundation can be used to study the buckling behavior of a hybrid beam, where the softer beam acts as the elastic foundation of the other beam [260–262]. For a simply supported hybrid beam subjected to a uniaxial compressive load, the critical compressive force N_{cr} can be expressed as [260]:

$$\frac{N_{cr}}{Dk^2} \approx \left(\frac{n\pi}{h_e k} \right)^2 + \left(\frac{n\pi}{h_e k} \right)^{-2} \quad (\text{B.1})$$

where $D = E_r w_r^3 / 12(1 - \nu_r^2)$ is the flexural rigidity of the rigid beam with Young's modulus E_r , width w_r , and Poisson's ratio ν_r . $k^{-1} = (2Dw_s(1 + \nu_s)/3E_s)^{1/4}$ is the characteristic delay distance of the rigid beam on a soft Winkler foundation beam, with its spring stiffness determined by the width w_s , Poisson's ratio ν_s , and Young's modulus E_s of the soft beam. h_e is the equivalent height of the hybrid beam and is the beam height (h) for a simply supported beam. n is a positive integer that determines the buckling shape of a hybrid beam.

In this study, each beam can be assumed to be a fixed-fixed beam suffering from a uniaxial compressive load as the hybrid beams are assembled into a metamaterial. The equivalent height of a fixed-fixed beam was half its height ($h_e = h/2$). Assuming $w_r = w_s$, $E_r = 500E_s$, and $\nu_r = \nu_s$ for incompressibility, Equation B.1 can be solved using its slenderness ratio (h/w) as follows:

$$\frac{N_{cr}}{Dk^2} \approx \left(\left(\frac{500}{9} \right)^{1/4} \frac{n\pi}{h/w} \right)^2 + \left(\left(\frac{500}{9} \right)^{1/4} \frac{n\pi}{h/w} \right)^{-2}. \quad (\text{B.2})$$

Clearly, the critical buckling force N_{cr} for a hybrid structure is not always minimized at the first order buckling shape with $n = 1$. Figure B.1 shows plots of the dimensionless buckling force as a function of h/w . Note that the critical buckling force fluctuates with h/w , and the beam tends to buckle in a high-order shape when $\frac{h}{w} > 12$. The slenderness ratio was set to 8, which corresponds to first order buckling (half-wave of a sinusoidal curve), to ensure that the beam deformed in the bending direction. In addition, the hybrid beam tended to bend in the direction of the rigid beam.

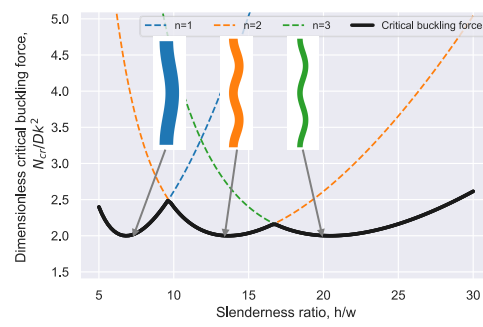


FIGURE B.1: Buckling analysis of a hybrid beam. The beam tends to buckle with higher-order model if the slenderness ratio is over 12.

Appendix C

Detail of Deep Learning Framework for 2D Auxetic Metamaterials

C.1 Details of 2D Conditional Generative Adversarial Network

The 2D-CGAN used in this study was composed of three neural network structures: a generator, discriminator, and solver. The generator was trained to produce patterns of auxetic metamaterials from latent variables (multivariate normal distribution) and user-defined labels (Young's modulus and Poisson's ratio) and simultaneously aimed to deceive the discriminator and solver. The discriminator was trained to distinguish between the patterns produced by the generator and those from the real dataset. The solver was trained to predict the Young's modulus and Poisson's ratio of a given pattern. The 2D-CGAN was optimized by a minimax game using the following equations:

$$\hat{\theta}_D = \arg \min_{\theta_D} \{L_D(t_D, D(\mathbf{X}; \theta_D)) + L_D(u_D, D(G(\mathbf{Z}, \mathbf{L}; \theta_G); \theta_D))\} \quad (\text{C.1})$$

$$\hat{\theta}_G = \arg \max_{\theta_G} \{L_D(u_D, D(G(\mathbf{Z}, \mathbf{L}; \theta_G); \theta_D)) - \alpha L_S(\mathbf{L}, S(G(\mathbf{Z}, \mathbf{L}; \theta_G); \theta_S))\} \quad (\text{C.2})$$

$$\hat{\theta}_S = \arg \max_{\theta_S} \{L_S(\mathbf{L}, S(\mathbf{X}; \theta_S))\} \quad (\text{C.3})$$

where θ_D , θ_G , and θ_S are the sets of parameters of the discriminator, generator, and solver, respectively. D , G , and S denote the discriminator, generator, and solver, respectively. $\mathbf{X} \in \mathbb{R}^{n \times p}$ is the training dataset (vectors of auxetic metamaterials), $\mathbf{L} \in \mathbb{R}^{n \times l}$ are the labels of the dataset (i.e., Young's moduli and Poisson's ratios), and $\mathbf{Z} \in \mathbb{R}^{n \times l}$ are the latent variables from a multivariate normal distribution during each iteration. L_D is a loss function (binary cross-entropy function) for the discriminator. t_D and u_D are target labels and are generally set to 1 and 0, respectively. However, I applied the label smoothing technique for the target labels [263]: t_D was replaced by a random number between 0.7 and 1.2, and u_D was replaced by a random number between 0 and 0.3. The moderating weights, α , determined the extent to which the generator focused on the training of the input labels and was set to be 0.1 in our study.

Deep learning calculations were performed using TensorFlow [264]. An Adam optimizer with a learning rate of 0.0001 and β_1 of 0.5 was used to train the model. The batch size for the training was set to 32. The detailed network structures used in this study are listed in Tables C.1–C.3. In short, the layers used included a 2D convolutional layer, a 2D transposed convolutional layer, 2D max pooling, a fully connected

layer, batch normalization, and dropout, and the activation functions used included Leaky ReLU and tanh. Note that circular padding was used in the 2D convolutional layer and 2D transposed convolutional layer to maintain and identify the periodicity of the patterns. Examples of downsampling and upsampling with circular padding and zero padding are shown in Figure C.1. It demonstrates that compared to the commonly used zero padding, circular padding can more effectively help the output tensor retain its periodicity.

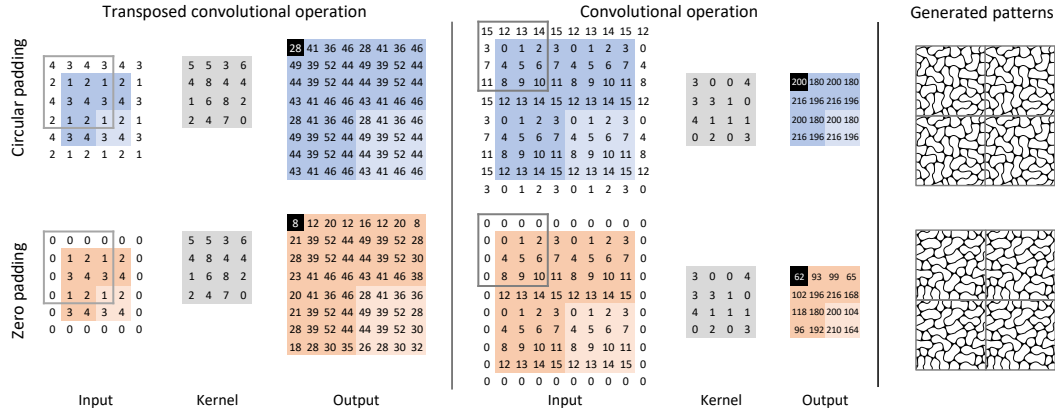


FIGURE C.1: Examples of use of circular padding and zero padding. Compared to the patterns generated using zero padding, those produced using circular padding remain more periodic.

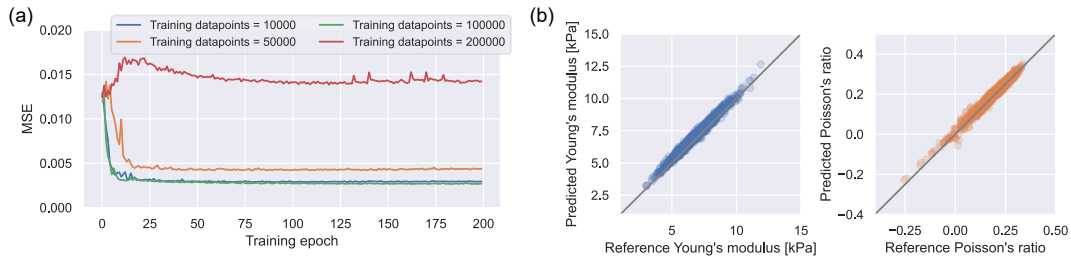


FIGURE C.2: (a) Performance of the solver of 2D-CGAN evaluated using the MSE between the predicted and reference elastic moduli for different numbers of datapoints. (b) Comparison between the solver-predicted and the reference elastic moduli. The reference elastic moduli are the elastic moduli of testing patterns calculated by the homogenization algorithm

Because the solver is independent of the generator and discriminator, I first trained the solver with supervised learning. The process takes about 23 hours for training 200 epochs with 100,000 datapoints on a single NVIDIA RTX A6000 graphic card. The solver is a type of linear regression model that can be used to predict the Young's modulus and Poisson's ratio (elastic moduli) of a given pattern. Figure C.2 shows the MSE between the predicted and reference elastic moduli for different numbers of datasets. A smaller MSE value represents a better performance of the trained solver. Each dataset was split as follows: 80% was used as the training set and 20% was

TABLE C.1: Network architecture of generator for 2D-CGAN.

Description	Kernel size	Resampling	Input shape	Output shape
Concatenate (Z, L)	-	-	128 + 2	130
Fully connected + Batch normalization + Reshape	-	-	130	4 × 4 × 512
2D transposed convolution + Batch normalization + Leaky ReLU	4 × 4	Up	4 × 4 × 512	8 × 8 × 256
2D transposed convolution + Batch normalization + Leaky ReLU	4 × 4	Up	8 × 8 × 256	16 × 16 × 128
2D transposed convolution + Batch normalization + Leaky ReLU	4 × 4	Up	16 × 16 × 128	32 × 32 × 64
2D transposed convolution + Batch normalization + Leaky ReLU	4 × 4	Up	32 × 32 × 64	64 × 64 × 32
2D transposed convolution + Batch normalization + Leaky ReLU	4 × 4	Up	64 × 64 × 32	128 × 128 × 16
2D transposed convolution	4 × 4	Up	128 × 128 × 16	256 × 256 × 1
Tanh	-	-	256 × 256 × 1	256 × 256 × 1

TABLE C.2: Network architecture of discriminator for 2D-CGAN.

Description	Kernel size	Resampling	Input shape	Output shape
2D convolution + Leaky ReLU + Dropout	4 × 4	Down	256 × 256 × 1	128 × 128 × 16
2D convolution + Leaky ReLU + Dropout	4 × 4	Down	128 × 128 × 16	64 × 64 × 32
2D convolution + Leaky ReLU + Dropout	4 × 4	Down	64 × 64 × 32	32 × 32 × 64
2D convolution + Leaky ReLU + Dropout	4 × 4	Down	32 × 32 × 64	16 × 16 × 128
2D convolution + Leaky ReLU + Dropout	4 × 4	Down	16 × 16 × 128	8 × 8 × 256
2D convolution + Leaky ReLU + Dropout	4 × 4	Down	8 × 8 × 256	4 × 4 × 512
Flatten	-	-	4 × 4 × 512	8192
Fully connected	-	-	8192	1
Tanh	-	-	256 × 256 × 1	256 × 256 × 1

used as the testing set. To prevent the solver from overfitting, early stopping was performed. As shown in Figure C.2a, the MSE reaches a very low value of 0.003 after 20 epochs when using 100,000 datapoints, and it becomes difficult to decrease the MSE further even when using a larger dataset (e.g., 200,000 datapoints). To be conservative, I chose 100,000 datapoints for the training process. Figure C.2b presents the predicted Young’s moduli and Poisson’s ratios of testing patterns, which shows the values predicted by the solver are quite close to the reference values and demonstrates the good performance of the solver. The linear relationship of the solver-predicted results is much better than that of the 2D-CGAN-generated results. After the solver had been well trained, the checkpoints of the solver were saved and the solver was used to train the generator and discriminator, in which the saved checkpoints were used to calculate the loss of the patterns produced by the generator. The process takes about 35 hours for training 200 epochs on a single NVIDIA RTX A6000 graphic card.

TABLE C.3: Network architecture of solver for 2D-CGAN.

	Description	Kernel size/pool size	Resampling	Input shape	Output shape
Unit 1	2D convolution	3×3	-	$256 \times 256 \times 1$	$256 \times 256 \times 16$
	2D convolution	3×3	-	$256 \times 256 \times 16$	$256 \times 256 \times 16$
	2D max pooling	2×2	Down	$256 \times 256 \times 1$	$128 \times 128 \times 16$
Unit 2	2D convolution	3×3	-	$128 \times 128 \times 16$	$128 \times 128 \times 32$
	2D convolution	3×3	-	$128 \times 128 \times 32$	$128 \times 128 \times 32$
	2D max pooling	2×2	Down	$128 \times 128 \times 32$	$64 \times 64 \times 32$
Unit 3	2D convolution	3×3	-	$64 \times 64 \times 32$	$64 \times 64 \times 64$
	2D convolution	3×3	-	$64 \times 64 \times 64$	$64 \times 64 \times 64$
	2D max pooling	2×2	Down	$64 \times 64 \times 64$	$32 \times 32 \times 64$
Unit 4	2D convolution	3×3	-	$32 \times 32 \times 64$	$32 \times 32 \times 128$
	2D convolution	3×3	-	$32 \times 32 \times 128$	$32 \times 32 \times 128$
	2D max pooling	2×2	Down	$32 \times 32 \times 128$	$16 \times 16 \times 128$
Unit 5	2D convolution	3×3	-	$16 \times 16 \times 128$	$16 \times 16 \times 256$
	2D convolution	3×3	-	$16 \times 16 \times 256$	$16 \times 16 \times 256$
	2D max pooling	2×2	Down	$16 \times 16 \times 256$	$8 \times 8 \times 256$
Unit 6	2D convolution	3×3	-	$8 \times 8 \times 256$	$8 \times 8 \times 384$
	2D convolution	3×3	-	$8 \times 8 \times 384$	$8 \times 8 \times 384$
	2D max pooling	2×2	Down	$8 \times 8 \times 384$	$4 \times 4 \times 384$
Unit 7	2D convolution	3×3	-	$4 \times 4 \times 384$	$4 \times 4 \times 512$
	2D convolution	3×3	-	$4 \times 4 \times 512$	$4 \times 4 \times 512$
	2D max pooling	2×2	Down	$4 \times 4 \times 512$	$2 \times 2 \times 512$
Unit 8	2D convolution	3×3	-	$2 \times 2 \times 512$	$2 \times 2 \times 512$
	2D convolution	3×3	-	$2 \times 2 \times 512$	$2 \times 2 \times 512$
	2D max pooling	2×2	Down	$2 \times 2 \times 512$	$1 \times 1 \times 512$
	Flatten + Fully connected	-	-	$1 \times 1 \times 512$	256
	Fully connected	-	-	256	128
	Fully connected	-	-	128	2

C.2 Patterns Generated by 2D-CGAN

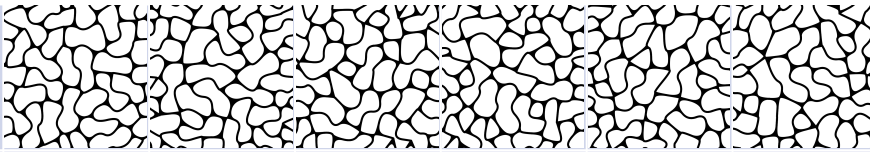
Patterns generated by CGAN						
ν_i (input)	-0.2	-0.1	0	0.1	0.2	0.3
ν_o (output)	-0.2029	-0.1004	0.0106	0.1091	0.2052	0.3028
ν_{xy} (FEM)	-0.1891	-0.0710	0.0121	0.0735	0.1701	0.3125
ν_{yz} (FEM)	-0.1312	-0.0975	0.0128	0.0896	0.1749	0.3483
E_i (input), [kPa]	4.0	4.5	5.0	5.5	6.0	8.5
E_o (output), [kPa]	3.9856	4.5753	4.9266	5.5892	5.8316	8.3386
E_{yy} (FEM), [kPa]	3.9046	5.1088	3.8596	4.7835	5.8519	8.1307
E_{xx} (FEM), [kPa]	3.8074	3.7126	5.5629	5.6258	5.8127	8.9898

FIGURE C.3: Patterns generated by the 2D-CGAN with different Young's moduli and Poisson's ratios.

The well-trained 2D-CGAN is capable of generating numerous patterns with a user-defined Young's modulus and Poisson's ratio. Figure C.3 shows some patterns produced by the 2D-CGAN with different Young's moduli and Poisson's ratios. The results show that the values of the input elastic moduli are very close to those of the output elastic moduli, which further demonstrates the good performance of the 2D-CGAN. Note that the differences between the elastic moduli calculated by the homogenization algorithm and the FEM simulation are caused by the algorithms themselves. The close agreement among the results of the 2D-CGAN predictions, FEM simulations, and experiments confirms that the proposed 2D-CGAN-based technique is a robust method for the inverse design of auxetic metamaterials.

I also investigated the deformation behaviors of different 2D-CGAN-generated patterns under uniaxial compression (Figure C.4). The good curve fitting of the stress-strain curves and Poisson's ratio curves along the x - and y -axes demonstrates the isotropic properties of this type of pattern. Furthermore, some patterns that initially have positive Poisson's ratios exhibit auxetic behavior during further compression, which due to the shrinking of interior concave pores.

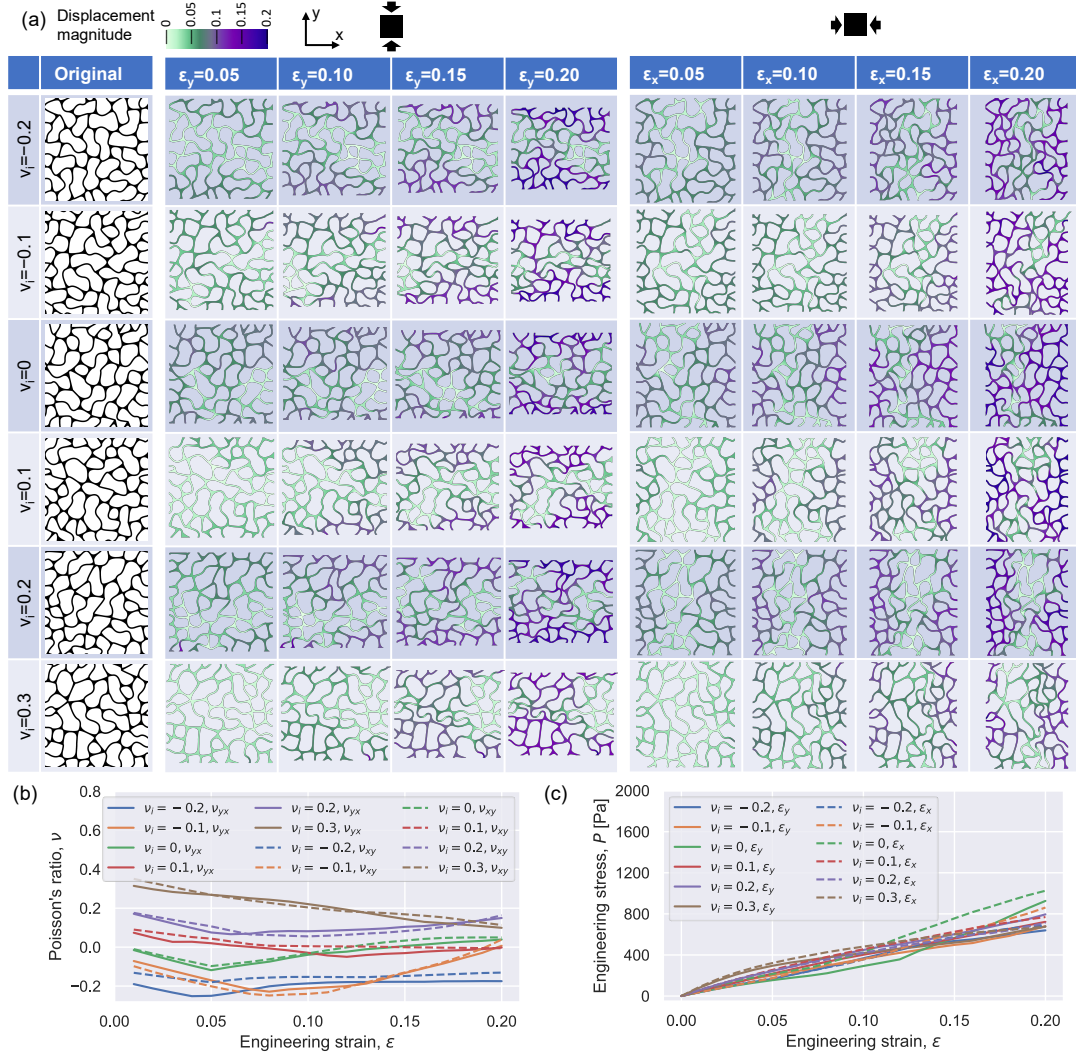


FIGURE C.4: Deformation behavior of patterns with different elastic moduli. (a) Progressively deformed configurations of FEM model under uniaxial compressive loading. (b) Poisson's ratio–strain curves and (c) stress–strain curves from FEM simulations.

Appendix D

Details of Deep Learning Framework for 3D Architected Materials

To train the 3D-CGAN, Adam optimization was implemented in the training process to optimize the parameters. The learning rates of the Adam optimizer were set to $\alpha = 0.0001$ and $\beta_1 = 0.5$. The Wasserstein distance was used to improve the quality of the generated samples. The gradient penalty regularized the discriminator in the 3D-CGAN to assist the convergence, and its parameter was set to 100. The batch size for training was set to 32, and the epoch for was set to 200. A dataset consisting of 10,000 datapoints was used to train the 3D-CGAN. The details of the three neural network structures are listed in Tables D.1–D.3. In summary, the generator consists of a fully connected layer, batch normalization, dropout, and a 3D transposed convolutional layer, and uses activation functions including Leaky ReLU and tanh; the discriminator consists of a fully connected layer, dropout, and 3D convolutional layer, and uses activation functions including Leaky ReLU and tanh; the solver consists of six 3D convolution blocks with a 3D max pooling layer in each of them, and ends up with three fully connected layers. As the architectures of these geometries are triply periodic, I applied circular padding in the convolutional layers for both up and down sampling processes.

The training process of 3D-CGAN was conducted using TensorFlow on a single NVIDIA RTX A6000 graphic card on Linux system. The solver was first trained using supervised learning. The solver was a linear regression model that used a 3D array of architectures as an input and yielded the predicted porosities and Young’s moduli as outputs. To investigate the effect of the number of datapoints on the performance of the solver, I trained the solver with different datasets. For each training dataset, 80% of the datapoints were used as the training set and 20% of the datapoints were used as the testing set. It required approximately 10 h to train 200 epochs using a dataset consisting of 10,000 datapoints. Figure D.1a compares the MSE of the testing set for different numbers of datapoints. It should be noted that it can be difficult for the solver to converge if the datapoints are less than 1000. However, with an increase in the number of datapoints, the solver converged and the MSE decreased, indicating that an increasing number of datapoints was beneficial for the training. The MSE converged to near 0.0001, though it is hard to reduce it further, even bigger datapoints were utilized.

To save training time and resources, I selected 10,000 datapoints for the training process. A more quantitative evaluation of the solver is shown in Figure D.1b, which compares the reference and predicted values in terms of relative density and Young’s modulus. The comparison between solver-predicted and reference values showed an excellent agreement, proving the accuracy of the trained solver. The well-trained

solver was saved as checkpoints and imported when training the generator and discriminator. Training the generator and discriminator was more time-consuming, and it cost approximately 32 h to train 10,000 datapoints for 200 epochs. After the three modules were trained, the 3D-CGAN was harnessed for the inverse design of the architected materials.

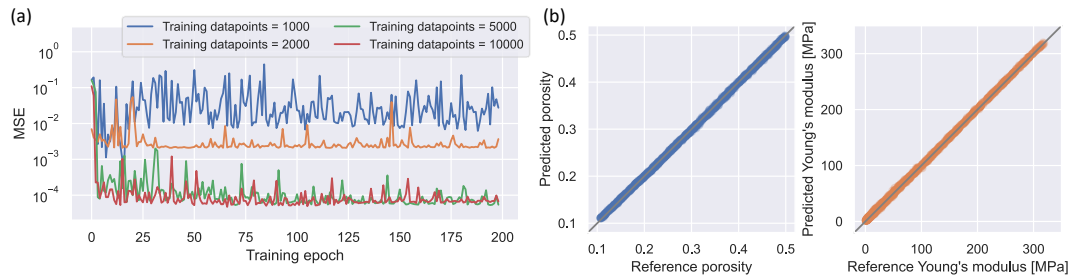


FIGURE D.1: Performance of the solver of 3D-CGAN. (a) MSE versus training epoch using different numbers of datapoints. (b) Reference against solver-predicted porosities and Young's modulus.

TABLE D.1: Neural network structure of generator for 3D-CGAN.

Neural network types	Kernel size	Resampling	Input array shape	Output array shape
Concatenate(Z, L)	-	-	128+2	130
Dense + BatchNormalization + Reshape	-	-	130	$2 \times 2 \times 2 \times 512$
3D transposed convolution + BatchNormalization + Leaky ReLU + Dropout (0.3)	4×4	Up	$2 \times 2 \times 2 \times 512$	$4 \times 4 \times 4 \times 256$
3D transposed convolution + BatchNormalization + Leaky ReLU + Dropout (0.3)	4×4	Up	$4 \times 4 \times 4 \times 256$	$8 \times 8 \times 8 \times 128$
3D transposed convolution + BatchNormalization + Leaky ReLU + Dropout (0.3)	4×4	Up	$8 \times 8 \times 8 \times 128$	$16 \times 16 \times 16 \times 64$
3D transposed convolution + BatchNormalization + Leaky ReLU + Dropout (0.3)	4×4	Up	$16 \times 16 \times 16 \times 64$	$32 \times 32 \times 32 \times 32$
3D transposed convolution	4×4	Up	$32 \times 32 \times 32 \times 32$	$64 \times 64 \times 64 \times 1$
Sigmoid	-	-	$64 \times 64 \times 64 \times 1$	$64 \times 64 \times 64 \times 1$

TABLE D.2: Neural network structure of discriminator for 3D-CGAN.

Neural network types	Kernel size	Resampling	Input array shape	Output array shape
Conv3D + LeakyReLU + Dropout (0.3)	4×4	Down	$64 \times 64 \times 64 \times 1$	$32 \times 32 \times 32 \times 16$
Conv3D + LeakyReLU + Dropout (0.3)	4×4	Down	$32 \times 32 \times 32 \times 16$	$16 \times 16 \times 16 \times 32$
Conv3D + LeakyReLU + Dropout (0.3)	4×4	Down	$16 \times 16 \times 16 \times 32$	$8 \times 8 \times 8 \times 64$
Conv3D + LeakyReLU + Dropout (0.3)	4×4	Down	$8 \times 8 \times 8 \times 64$	$4 \times 4 \times 4 \times 128$
Conv3D + LeakyReLU + Dropout (0.3)	4×4	Down	$4 \times 4 \times 4 \times 128$	$2 \times 2 \times 2 \times 256$
Conv3D + LeakyReLU + Dropout (0.3)	4×4	Down	$2 \times 2 \times 2 \times 256$	$1 \times 1 \times 1 \times 512$
Flatten	-	-	$1 \times 1 \times 1 \times 512$	512
Dense	-	-	512	1

TABLE D.3: Neural network structure of solver for 3D-CGAN.

	Neural network types	Kernel/pool size	Resampling	Input array shape	Output array shape
Unit 1	Conv3D	3×3	-	$64 \times 64 \times 64 \times 1$	$64 \times 64 \times 64 \times 16$
	Conv3D	3×3	-	$64 \times 64 \times 64 \times 16$	$64 \times 64 \times 64 \times 16$
	3D max pooling	2×2	Down	$64 \times 64 \times 64 \times 16$	$32 \times 32 \times 32 \times 16$
Unit 2	Conv3D	3×3	-	$32 \times 32 \times 32 \times 16$	$32 \times 32 \times 32 \times 32$
	Conv3D	3×3	-	$32 \times 32 \times 32 \times 32$	$32 \times 32 \times 32 \times 32$
Unit 3	3D max pooling	2×2	Down	$32 \times 32 \times 32 \times 32$	$16 \times 16 \times 16 \times 32$
	Conv3D	3×3	-	$16 \times 16 \times 16 \times 32$	$16 \times 16 \times 16 \times 64$
	Conv3D	3×3	-	$16 \times 16 \times 16 \times 64$	$16 \times 16 \times 16 \times 64$
Unit 4	3D max pooling	2×2	Down	$16 \times 16 \times 16 \times 64$	$8 \times 8 \times 8 \times 64$
	Conv3D	3×3	-	$8 \times 8 \times 8 \times 64$	$8 \times 8 \times 8 \times 128$
	Conv3D	3×3	-	$8 \times 8 \times 8 \times 128$	$8 \times 8 \times 8 \times 128$
Unit 5	3D max pooling	2×2	Down	$8 \times 8 \times 8 \times 128$	$4 \times 4 \times 4 \times 128$
	Conv3D	3×3	-	$4 \times 4 \times 4 \times 128$	$4 \times 4 \times 4 \times 256$
	Conv3D	3×3	-	$4 \times 4 \times 4 \times 256$	$4 \times 4 \times 4 \times 256$
Unit 6	3D max pooling	2×2	Down	$4 \times 4 \times 4 \times 256$	$2 \times 2 \times 2 \times 256$
	Conv3D	3×3	-	$2 \times 2 \times 2 \times 256$	$2 \times 2 \times 2 \times 512$
	Conv3D	3×3	-	$2 \times 2 \times 2 \times 512$	$2 \times 2 \times 2 \times 512$
	3D max pooling	2×2	Down	$2 \times 2 \times 2 \times 512$	$1 \times 1 \times 1 \times 512$
	Flatten + Dense	-	-	$1 \times 1 \times 1 \times 512$	256
	Dense	-	-	256	128
	Dense	-	-	128	2

Bibliography

- [1] Muamer Kadic et al. “3D metamaterials”. In: *Nature Reviews Physics* 1.3 (2019), pp. 198–210.
- [2] Xiaoxing Xia, Christopher M Spadaccini, and Julia R Greer. “Responsive materials architected in space and time”. In: *Nature Reviews Materials* 7.9 (2022), pp. 683–701.
- [3] Kebin Fan and Willie J Padilla. “Dynamic electromagnetic metamaterials”. In: *Materials Today* 18.1 (2015), pp. 39–50.
- [4] Costas M Soukoulis and Martin Wegener. “Past achievements and future challenges in the development of three-dimensional photonic metamaterials”. In: *Nature photonics* 5.9 (2011), pp. 523–530.
- [5] Steven A Cummer, Johan Christensen, and Andrea Alù. “Controlling sound with acoustic metamaterials”. In: *Nature Reviews Materials* 1.3 (2016), pp. 1–13.
- [6] Ying Li et al. “Transforming heat transfer with thermal metamaterials and devices”. In: *Nature Reviews Materials* 6.6 (2021), pp. 488–507.
- [7] Xianglong Yu et al. “Mechanical metamaterials associated with stiffness, rigidity and compressibility: A brief review”. In: *Progress in Materials Science* 94 (2018), pp. 114–173.
- [8] Katia Bertoldi et al. “Flexible mechanical metamaterials”. In: *Nature Reviews Materials* 2.11 (2017), pp. 1–11.
- [9] Pingqiang Cai et al. “Mechanomaterials: a rational deployment of forces and geometries in programming functional materials”. In: *Advanced Materials* 33.46 (2021), p. 2007977.
- [10] Johan Christensen et al. “Vibrant times for mechanical metamaterials”. In: *Mrs Communications* 5.3 (2015), pp. 453–462.
- [11] Sahab Babae et al. “3D soft metamaterials with negative Poisson’s ratio”. In: *Advanced Materials* 25.36 (2013), pp. 5044–5049.
- [12] H MA Kolken and AA Zadpoor. “Auxetic mechanical metamaterials”. In: *RSC advances* 7.9 (2017), pp. 5111–5129.
- [13] Jens Bauer et al. “Nanolattices: an emerging class of mechanical metamaterials”. In: *Advanced Materials* 29.40 (2017), p. 1701850.
- [14] Xiaoyu Zheng et al. “Ultralight, ultrastiff mechanical metamaterials”. In: *Science* 344.6190 (2014), pp. 1373–1377.
- [15] Tobias A Schaedler et al. “Ultralight metallic microlattices”. In: *Science* 334.6058 (2011), pp. 962–965.
- [16] Xiao-Ning Liu et al. “An elastic metamaterial with simultaneously negative mass density and bulk modulus”. In: *Applied physics letters* 98.25 (2011), p. 251907.
- [17] Sheng Sang, Anwer Mhannawee, and Ziping Wang. “A design of active elastic metamaterials with negative mass density and tunable bulk modulus”. In: *Acta Mechanica* 230.3 (2019), pp. 1003–1008.

- [18] Kai Wang et al. "Low-frequency band gaps in a metamaterial rod by negative-stiffness mechanisms: Design and experimental validation". In: *Applied Physics Letters* 114.25 (2019), p. 251902.
- [19] Tiemo Bückmann et al. "An elasto-mechanical unfeelability cloak made of pentamode metamaterials". In: *Nature communications* 5.1 (2014), pp. 1–6.
- [20] Muamer Kadic et al. "On the practicability of pentamode mechanical metamaterials". In: *Applied Physics Letters* 100.19 (2012), p. 191901.
- [21] Jesse L Silverberg et al. "Using origami design principles to fold reprogrammable mechanical metamaterials". In: *science* 345.6197 (2014), pp. 647–650.
- [22] Johannes TB Overvelde et al. "A three-dimensional actuated origami-inspired transformable metamaterial with multiple degrees of freedom". In: *Nature communications* 7.1 (2016), pp. 1–8.
- [23] Roberto Stefano Naboni, Stefano Sartori Pezzi, et al. "Embedding auxetic properties in designing active-bending gridshells". In: *SIGraDi 2016*. BRA. 2016, pp. 720–726.
- [24] Ying Jiang et al. "Auxetic mechanical metamaterials to enhance sensitivity of stretchable strain sensors". In: *Advanced Materials* 30.12 (2018), p. 1706589.
- [25] Faisal Amin et al. "Auxetic coronary stent endoprosthesis: Fabrication and structural analysis". In: *Journal of Applied Biomaterials & Functional Materials* 13.2 (2015), pp. 127–135.
- [26] Helena MA Kolken et al. "Rationally designed meta-implants: a combination of auxetic and conventional meta-biomaterials". In: *Materials Horizons* 5.1 (2018), pp. 28–35.
- [27] Shangqin Yuan et al. "3D soft auxetic lattice structures fabricated by selective laser sintering: TPU powder evaluation and process optimization". In: *Materials & Design* 120 (2017), pp. 317–327.
- [28] Dinh Hai Le et al. "Transformation from 2D meta-pixel to 3D meta-pixel using auxetic kirigami for programmable multifunctional electromagnetic response". In: *Extreme Mechanics Letters* 36 (2020), p. 100670.
- [29] Young-Joo Lee et al. "Auxetic elastomers: mechanically programmable meta-elastomers with an unusual Poisson's ratio overcome the gauge limit of a capacitive type strain sensor". In: *Extreme Mechanics Letters* 31 (2019), p. 100516.
- [30] Wenwang Wu et al. "Mechanical properties of anti-tetrachiral auxetic stents". In: *Composite Structures* 185 (2018), pp. 381–392.
- [31] Jeffrey Ian Lipton et al. "Handedness in shearing auxetics creates rigid and compliant structures". In: *Science* 360.6389 (2018), pp. 632–635.
- [32] Krzysztof K Dudek, Ruben Gatt, and Joseph N Grima. "3D composite metamaterial with magnetic inclusions exhibiting negative stiffness and auxetic behaviour". In: *Materials & Design* 187 (2020), p. 108403.
- [33] Athina Papadopoulou, Jared Laucks, and Skylar Tibbits. "Auxetic materials in design and architecture". In: *Nature Reviews Materials* 2.12 (2017), pp. 1–3.
- [34] Bharath R Krishnan et al. "Auxetic structure metamaterial for crash safety of sports helmet". In: *Materials Today: Proceedings* 56 (2022), pp. 1043–1049.
- [35] Olly Duncan et al. "Review of auxetic materials for sports applications: Expanding options in comfort and protection". In: *Applied Sciences* 8.6 (2018), p. 941.

- [36] Pengcheng Jiao and Amir H Alavi. "Artificial intelligence-enabled smart mechanical metamaterials: advent and future trends". In: *International Materials Reviews* 66.6 (2021), pp. 365–393.
- [37] Farzad Zangeneh-Nejad et al. "Analogue computing with metamaterials". In: *Nature Reviews Materials* 6.3 (2021), pp. 207–225.
- [38] S Macrae Montgomery et al. "Recent advances in additive manufacturing of active mechanical metamaterials". In: *Current Opinion in Solid State and Materials Science* 24.5 (2020), p. 100869.
- [39] Katsuyuki Suzuki and Noboru Kikuchi. "A homogenization method for shape and topology optimization". In: *Computer methods in applied mechanics and engineering* 93.3 (1991), pp. 291–318.
- [40] Erik Andreassen and Casper Schousboe Andreassen. "How to determine composite material properties using numerical homogenization". In: *Computational Materials Science* 83 (2014), pp. 488–495.
- [41] BM Said et al. "On the homogenization of 2d porous material with determination of rve". In: *International Journal of Mechanical and Mechatronics Engineering* 16.1 (2016), pp. 81–86.
- [42] Guoying Dong, Yunlong Tang, and Yaoyao Fiona Zhao. "A 149 line homogenization code for three-dimensional cellular materials written in matlab". In: *Journal of Engineering Materials and Technology* 141.1 (2019).
- [43] Norbert Huber et al. "Scaling laws of nanoporous metals under uniaxial compression". In: *Acta materialia* 67 (2014), pp. 252–265.
- [44] Xiaoyang Zheng et al. "Minimal surface designs for porous materials: from microstructures to mechanical properties". In: *Journal of materials science* 53.14 (2018), pp. 10194–10208.
- [45] A Azzam and W Li. "An experimental investigation on the three-point bending behavior of composite laminate". In: *IOP Conference Series: Materials Science and Engineering*. Vol. 62. 1. IOP Publishing. 2014, p. 012016.
- [46] Yifan Wang et al. "Structured fabrics with tunable mechanical properties". In: *Nature* 596.7871 (2021), pp. 238–243.
- [47] Luonan Zhou et al. "Parametric and experiment studies of 3D auxetic lattices based on hollow shell cuboctahedron". In: *Smart Materials and Structures* 30.2 (2021), p. 025042.
- [48] S Janbaz et al. "Strain rate-dependent mechanical metamaterials". In: *Science advances* 6.25 (2020), eaba0616.
- [49] Yixin Chen, Bin Ai, and Zi Jing Wong. "Soft optical metamaterials". In: *Nano Convergence* 7.1 (2020), pp. 1–17.
- [50] Hajun Lee et al. "3D-printed programmable tensegrity for soft robotics". In: *Science Robotics* 5.45 (2020), eaay9024.
- [51] Shuai Wu et al. "Evolutionary algorithm-guided voxel-encoding printing of functional hard-magnetic soft active materials". In: *Advanced Intelligent Systems* 2.8 (2020), p. 2000060.
- [52] Tianqi Xu et al. "Millimeter-scale flexible robots with programmable three-dimensional magnetization and motions". In: *Science Robotics* 4.29 (2019), eaav4494.

- [53] Jochen Mueller, Jennifer A Lewis, and Katia Bertoldi. "Architected Multimaterial Lattices with Thermally Programmable Mechanical Response". In: *Advanced Functional Materials* 32.1 (2022), p. 2105128.
- [54] Diab W Abueidda et al. "Mechanical properties of 3D printed polymeric cellular materials with triply periodic minimal surface architectures". In: *Materials & Design* 122 (2017), pp. 255–267.
- [55] Shangqin Yuan, Chee Kai Chua, and Kun Zhou. "3D-printed mechanical metamaterials with high energy absorption". In: *Advanced Materials Technologies* 4.3 (2019), p. 1800419.
- [56] Mehrdad Mohsenizadeh et al. "Additively-manufactured lightweight Metamaterials for energy absorption". In: *Materials & Design* 139 (2018), pp. 521–530.
- [57] Zefeng Xiao et al. "Evaluation of topology-optimized lattice structures manufactured via selective laser melting". In: *Materials & Design* 143 (2018), pp. 27–37.
- [58] Carlos M Portela et al. "Extreme mechanical resilience of self-assembled nanolabyrinthine materials". In: *Proceedings of the National Academy of Sciences* 117.11 (2020), pp. 5686–5693.
- [59] Georges Voronoi. "Nouvelles applications des paramètres continus à la théorie des formes quadratiques. Premier mémoire. Sur quelques propriétés des formes quadratiques positives parfaites." In: *Journal für die reine und angewandte Mathematik (Crelles Journal)* 133 (1908), pp. 97–102.
- [60] Dong Li et al. "Negative Poisson's ratio in 2D Voronoi cellular solids by biaxial compression: a numerical study". In: *Journal of materials science* 51.14 (2016), pp. 7029–7037.
- [61] Mustapha Bouakba, Abderrezak Bezazi, and Fabrizio Scarpa. "FE analysis of the in-plane mechanical properties of a novel Voronoi-type lattice with positive and negative Poisson's ratio configurations". In: *International Journal of Solids and Structures* 49.18 (2012), pp. 2450–2459.
- [62] Xiaoyang Zheng et al. "Controllable inverse design of auxetic metamaterials using deep learning". In: *Materials & Design* 211 (2021), p. 110178.
- [63] Xiaoyang Zheng et al. "Structure-dependent analysis of nanoporous metals: clues from mechanical, conduction, and flow properties". In: *The Journal of Physical Chemistry C* 122.29 (2018), pp. 16803–16809.
- [64] Shiwei Zhao, T Matthew Evans, and Xiaowen Zhou. "Three-dimensional Voronoi analysis of monodisperse ellipsoids during triaxial shear". In: *Powder Technology* 323 (2018), pp. 323–336.
- [65] Changhui Zhang et al. "Three-dimensional Voronoi analysis of realistic grain packing: An XCT assisted set Voronoi tessellation framework". In: *Powder Technology* 379 (2021), pp. 251–264.
- [66] Yong Yi et al. "Multi-scale modeling for predicting the stiffness and strength of hollow-structured metal foams with structural hierarchy". In: *Materials* 11.3 (2018), p. 380.
- [67] Hao Ma et al. "Simulation and analysis of mechanical properties of silica aerogels: From rationalization to prediction". In: *Materials* 11.2 (2018), p. 214.

- [68] Kenneth A Hart and Julian J Rimoli. "Generation of statistically representative microstructures with direct grain geometry control". In: *Computer Methods in Applied Mechanics and Engineering* 370 (2020), p. 113242.
- [69] Jiaxin Zhou, Ikumu Watanabe, and Takayuki Yamada. "Computational morphology design of duplex structure considering interface debonding". In: *Composite Structures* (2022), p. 116200.
- [70] Jinglai Wu et al. "Level-set topology optimization for mechanical metamaterials under hybrid uncertainties". In: *Computer Methods in Applied Mechanics and Engineering* 319 (2017), pp. 414–441.
- [71] Yongfeng Zheng et al. "Evolutionary topology optimization for mechanical metamaterials with auxetic property". In: *International Journal of Mechanical Sciences* 179 (2020), p. 105638.
- [72] Hunter T Kollmann et al. "Deep learning for topology optimization of 2D metamaterials". In: *Materials & Design* 196 (2020), p. 109098.
- [73] Mengli Ye, Liang Gao, and Hao Li. "A design framework for gradually stiffer mechanical metamaterial induced by negative Poisson's ratio property". In: *Materials & Design* 192 (2020), p. 108751.
- [74] Erik Andreassen, Boyan S Lazarov, and Ole Sigmund. "Design of manufacturable 3D extremal elastic microstructure". In: *Mechanics of Materials* 69.1 (2014), pp. 1–10.
- [75] William J Boettinger et al. "Phase-field simulation of solidification". In: *Annual review of materials research* 32.1 (2002), pp. 163–194.
- [76] John W Cahn. "On spinodal decomposition". In: *Acta metallurgica* 9.9 (1961), pp. 795–801.
- [77] Ananthan Vidyasagar, Sebastian Krödel, and Dennis M Kochmann. "Microstructural patterns with tunable mechanical anisotropy obtained by simulating anisotropic spinodal decomposition". In: *Proceedings of the Royal Society A: Mathematical, Physical and Engineering Sciences* 474.2218 (2018), p. 20180535.
- [78] Meng-Ting Hsieh et al. "The mechanical response of cellular materials with spinodal topologies". In: *Journal of the Mechanics and Physics of Solids* 125 (2019), pp. 401–419.
- [79] Celal Soyarslan et al. "3D stochastic bicontinuous microstructures: Generation, topology and elasticity". In: *Acta materialia* 149 (2018), pp. 326–340.
- [80] Siddhant Kumar et al. "Inverse-designed spinodoid metamaterials". In: *npj Computational Materials* 6.1 (2020), pp. 1–10.
- [81] Dongdong Gu et al. "Material-structure-performance integrated laser-metal additive manufacturing". In: *Science* 372.6545 (2021), eabg1487.
- [82] Meisam Askari et al. "Additive manufacturing of metamaterials: A review". In: *Additive Manufacturing* 36 (2020), p. 101562.
- [83] Junxiang Fan et al. "A review of additive manufacturing of metamaterials and developing trends". In: *Materials Today* (2021).
- [84] Ryan L Truby and Jennifer A Lewis. "Printing soft matter in three dimensions". In: *Nature* 540.7633 (2016), pp. 371–378.
- [85] Amin Farzaneh et al. "Sequential metamaterials with alternating Poisson's ratios". In: *Nature communications* 13.1 (2022), pp. 1–9.

- [86] Luke Mizzi et al. "Highly stretchable two-dimensional auxetic metamaterial sheets fabricated via direct-laser cutting". In: *International Journal of Mechanical Sciences* 167 (2020), p. 105242.
- [87] Seung Chul Han, Dae Seung Kang, and Kiju Kang. "Two nature-mimicking auxetic materials with potential for high energy absorption". In: *Materials Today* 26 (2019), pp. 30–39.
- [88] Ki-Ju Kang. "Wire-woven cellular metals: The present and future". In: *Progress in Materials Science* 69 (2015), pp. 213–307.
- [89] Farhang Momeni, Xun Liu, Jun Ni, et al. "A review of 4D printing". In: *Materials & design* 122 (2017), pp. 42–79.
- [90] Xiao Kuang et al. "Advances in 4D printing: materials and applications". In: *Advanced Functional Materials* 29.2 (2019), p. 1805290.
- [91] Aamir Ahmed et al. "4D printing: Fundamentals, materials, applications and challenges". In: *Polymer* 228 (2021), p. 123926.
- [92] MJ Mirzaali et al. "Shape-matching soft mechanical metamaterials". In: *Scientific reports* 8.1 (2018), pp. 1–7.
- [93] Lucas R Meza et al. "Resilient 3D hierarchical architected metamaterials". In: *Proceedings of the National Academy of Sciences* 112.37 (2015), pp. 11502–11507.
- [94] Mark A Skylar-Scott et al. "Voxelated soft matter via multimaterial multinozzle 3D printing". In: *Nature* 575.7782 (2019), pp. 330–335.
- [95] Brian H Cumpston et al. "Two-photon polymerization initiators for three-dimensional optical data storage and microfabrication". In: *Nature* 398.6722 (1999), pp. 51–54.
- [96] C Sun et al. "Projection micro-stereolithography using digital micro-mirror dynamic mask". In: *Sensors and Actuators A: Physical* 121.1 (2005), pp. 113–120.
- [97] John R Tumbleston et al. "Continuous liquid interface production of 3D objects". In: *Science* 347.6228 (2015), pp. 1349–1352.
- [98] Christopher J Hansen et al. "High-throughput printing via microvascular multi-nozzle arrays". In: *Advanced Materials* 25.1 (2013), pp. 96–102.
- [99] James O Hardin et al. "Microfluidic printheads for multimaterial 3D printing of viscoelastic inks". In: *Advanced materials* 27.21 (2015), pp. 3279–3284.
- [100] Omar A Mohamed, Syed H Masood, and Jahar L Bhowmik. "Optimization of fused deposition modeling process parameters: a review of current research and future prospects". In: *Advances in manufacturing* 3.1 (2015), pp. 42–53.
- [101] Olga S Carneiro, AF Silva, and Rui Gomes. "Fused deposition modeling with polypropylene". In: *Materials & Design* 83 (2015), pp. 768–776.
- [102] Wenfeng Liu et al. "Improving mechanical performance of fused deposition modeling lattice structures by a snap-fitting method". In: *Materials & Design* 181 (2019), p. 108065.
- [103] Ferdinando Auricchio et al. "A novel layered topology of auxetic materials based on the tetrachiral honeycomb microstructure". In: *Materials & Design* 179 (2019), p. 107883.
- [104] M Bhuvanesh Kumar, P Sathiya, and M Varatharajulu. "Selective Laser Sintering". In: *Advances in Additive Manufacturing Processes* (2021), p. 28.

- [105] Paulo Jorge Bártolo. *Stereolithography: materials, processes and applications*. Springer Science & Business Media, 2011.
- [106] Xiaoyu Zheng et al. "Multiscale metallic metamaterials". In: *Nature materials* 15.10 (2016), pp. 1100–1106.
- [107] Tobias Frenzel, Muamer Kadic, and Martin Wegener. "Three-dimensional mechanical metamaterials with a twist". In: *Science* 358.6366 (2017), pp. 1072–1074.
- [108] Victoria G Rocha et al. "Direct ink writing advances in multi-material structures for a sustainable future". In: *Journal of Materials Chemistry A* 8.31 (2020), pp. 15646–15657.
- [109] Chen Yang et al. "4D printing reconfigurable, deployable and mechanically tunable metamaterials". In: *Materials Horizons* 6.6 (2019), pp. 1244–1250.
- [110] Teunis van Manen et al. "4D printing of reconfigurable metamaterials and devices". In: *Communications Materials* 2.1 (2021), pp. 1–8.
- [111] Xiaozhou Xin et al. "4D printing auxetic metamaterials with tunable, programmable, and reconfigurable mechanical properties". In: *Advanced Functional Materials* 30.43 (2020), p. 2004226.
- [112] Biao Zhang et al. "Mechanically robust and UV-curable shape-memory polymers for digital light processing based 4D printing". In: *Advanced Materials* 33.27 (2021), p. 2101298.
- [113] Xiaonan Huang et al. "Shape memory materials for electrically-powered soft machines". In: *Journal of Materials Chemistry B* 8.21 (2020), pp. 4539–4551.
- [114] Qian Zhao et al. "Shape memory polymer network with thermally distinct elasticity and plasticity". In: *Science advances* 2.1 (2016), e1501297.
- [115] TJ Wallin, James Pikul, and RF Shepherd. "3D printing of soft robotic systems". In: *Nature Reviews Materials* 3.6 (2018), pp. 84–100.
- [116] Yoonho Kim et al. "Printing ferromagnetic domains for untethered fast-transforming soft materials". In: *Nature* 558.7709 (2018), pp. 274–279.
- [117] Qingkun Liu et al. "Micrometer-sized electrically programmable shape-memory actuators for low-power microrobotics". In: *Science Robotics* 6.52 (2021), eabe6663.
- [118] Binjie Jin et al. "Programming a crystalline shape memory polymer network with thermo-and photo-reversible bonds toward a single-component soft robot". In: *Science advances* 4.1 (2018), eaao3865.
- [119] Mitsuhiro Ebara et al. "Shape-memory surface with dynamically tunable nano-geometry activated by body heat". In: *Advanced Materials* 24.2 (2012), pp. 273–278.
- [120] H Yasuda and Jinkyu Yang. "Reentrant origami-based metamaterials with negative Poisson's ratio and bistability". In: *Physical Review Letters* 114.18 (2015), p. 185502.
- [121] Zeyao Chen et al. "Re-entrant Auxetic Lattices with Enhanced Stiffness: A Numerical Study". In: *International Journal of Mechanical Sciences* 178 (2020), p. 105619.
- [122] Xiang Li et al. "Directions dependence of the elastic properties of a 3D augmented re-entrant cellular structure". In: *Materials & Design* 134 (2017), pp. 151–162.
- [123] Xin-Tao Wang et al. "Mechanical properties of 3D re-entrant auxetic cellular structures". In: *International Journal of Mechanical Sciences* 131 (2017), pp. 396–407.

- [124] Qiang Gao et al. "Theoretical, numerical and experimental analysis of three-dimensional double-V honeycomb". In: *Materials & Design* 139 (2018), pp. 380–391.
- [125] Qiang Gao et al. "Geometrically nonlinear mechanical properties of auxetic double-V microstructures with negative Poisson's ratio". In: *European Journal of Mechanics-A/Solids* 80 (2020), p. 103933.
- [126] Juan Carlos Álvarez Elipe and Andrés Díaz Lantada. "Comparative study of auxetic geometries by means of computer-aided design and engineering". In: *Smart Materials and Structures* 21.10 (2012), p. 105004.
- [127] Yunyao Jiang and Yaning Li. "3D printed chiral cellular solids with amplified auxetic effects due to elevated internal rotation". In: *Advanced Engineering Materials* 19.2 (2017), p. 1600609.
- [128] Luke Mizzi et al. "Mechanical metamaterials with star-shaped pores exhibiting negative and zero Poisson's ratio". In: *Materials & Design* 146 (2018), pp. 28–37.
- [129] Hamid Ebrahimi et al. "3D cellular metamaterials with planar anti-chiral topology". In: *Materials & design* 145 (2018), pp. 226–231.
- [130] Minghui Fu, Fengming Liu, and Lingling Hu. "A novel category of 3D chiral material with negative Poisson's ratio". In: *Composites Science and Technology* 160 (2018), pp. 111–118.
- [131] Zixing Lu et al. "Elastic properties of two novel auxetic 3D cellular structures". In: *International Journal of Solids and Structures* 124 (2017), pp. 46–56.
- [132] Dongdong Ye et al. "Deformation drives alignment of nanofibers in framework for inducing anisotropic cellulose hydrogels with high toughness". In: *ACS applied materials & interfaces* 9.49 (2017), pp. 43154–43162.
- [133] Johannes Tesse Bastiaan Overvelde, Sicong Shan, and Katia Bertoldi. "Compaction through buckling in 2D periodic, soft and porous structures: effect of pore shape". In: *Advanced Materials* 24.17 (2012), pp. 2337–2342.
- [134] Jianhu Shen et al. "Simple cubic three-dimensional auxetic metamaterials". In: *physica status solidi (b)* 251.8 (2014), pp. 1515–1522.
- [135] Xin Ren et al. "Design and characterisation of a tuneable 3D buckling-induced auxetic metamaterial". In: *Materials & Design* 139 (2018), pp. 336–342.
- [136] Jifang Zeng, Hong Hu, and Lin Zhou. "A study on negative Poisson's ratio effect of 3D auxetic orthogonal textile composites under compression". In: *Smart Materials and Structures* 26.6 (2017), p. 065014.
- [137] Lin Zhou, Lili Jiang, and Hong Hu. "Auxetic composites made of 3D textile structure and polyurethane foam". In: *physica status solidi (b)* 253.7 (2016), pp. 1331–1341.
- [138] Graeme W Milton. "Composite materials with Poisson's ratios close to -1". In: *Journal of the Mechanics and Physics of Solids* 40.5 (1992), pp. 1105–1137.
- [139] Oraib Al-Ketan and Rashid K Abu Al-Rub. "Multifunctional mechanical metamaterials based on triply periodic minimal surface lattices". In: *Advanced Engineering Materials* 21.10 (2019), p. 1900524.
- [140] Lu Han and Shunai Che. "An overview of materials with triply periodic minimal surfaces and related geometry: from biological structures to self-assembled systems". In: *Advanced Materials* 30.17 (2018), p. 1705708.

- [141] Xiaofeng Guo et al. "Mechanical behavior of TPMS-based scaffolds: a comparison between minimal surfaces and their lattice structures". In: *SN Applied Sciences* 1.10 (2019), pp. 1–11.
- [142] Fei Liu et al. "Functionally graded porous scaffolds in multiple patterns: New design method, physical and mechanical properties". In: *Materials & Design* 160 (2018), pp. 849–860.
- [143] Nan Yang et al. "Multi-morphology transition hybridization CAD design of minimal surface porous structures for use in tissue engineering". In: *Computer-Aided Design* 56 (2014), pp. 11–21.
- [144] Dong-Jin Yoo and Kwang-Hyuk Kim. "An advanced multi-morphology porous scaffold design method using volumetric distance field and beta growth function". In: *International Journal of Precision Engineering and Manufacturing* 16.9 (2015), pp. 2021–2032.
- [145] Celal Soyarslan, Vincent Blümer, and Swantje Bargmann. "Tunable auxeticity and elastomechanical symmetry in a class of very low density core-shell cubic crystals". In: *Acta Materialia* 177 (2019), pp. 280–292.
- [146] Levi C Felix, Cristiano F Woellner, and Douglas S Galvao. "Mechanical and energy-absorption properties of schwarzites". In: *Carbon* 157 (2020), pp. 670–680.
- [147] Ramin Hamzehei et al. "Octagonal auxetic metamaterials with hyperelastic properties for large compressive deformation". In: *International Journal of Mechanical Sciences* 145 (2018), pp. 96–105.
- [148] Qingqing Cheng et al. "3D printing-directed auxetic Kevlar aerogel architectures with multiple functionalization options". In: *Journal of Materials Chemistry A* 8.28 (2020), pp. 14243–14253.
- [149] Li Yang et al. "Compressive properties of Ti–6Al–4V auxetic mesh structures made by electron beam melting". In: *Acta Materialia* 60.8 (2012), pp. 3370–3379.
- [150] Li Yang et al. "Mechanical properties of 3D re-entrant honeycomb auxetic structures realized via additive manufacturing". In: *International Journal of Solids and Structures* 69 (2015), pp. 475–490.
- [151] Alan Hugh Schoen. *Infinite periodic minimal surfaces without self-intersections*. National Aeronautics and Space Administration, 1970.
- [152] Hermann Amandus Schwarz. *Gesammelte mathematische abhandlungen*. Vol. 260. American Mathematical Soc., 1972.
- [153] I Watanabe et al. "Multiscale prediction of mechanical behavior of ferrite–pearlite steel with numerical material testing". In: *International journal for numerical methods in engineering* 89.7 (2012), pp. 829–845.
- [154] Ikumu Watanabe and Akinori Yamanaka. "Voxel coarsening approach on image-based finite element modeling of representative volume element". In: *International Journal of Mechanical Sciences* 150 (2019), pp. 314–321.
- [155] Ahmad Rafsanjani, Katia Bertoldi, and André R Studart. "Programming soft robots with flexible mechanical metamaterials". In: *Science Robotics* 4.29 (2019), eaav7874.
- [156] Nazek El-Atab et al. "Soft actuators for soft robotic applications: a review". In: *Advanced Intelligent Systems* 2.10 (2020), p. 2000128.

- [157] François Schmitt et al. "Soft robots manufacturing: A review". In: *Frontiers in Robotics and AI* 5 (2018), p. 84.
- [158] Dian Yang et al. "Buckling of elastomeric beams enables actuation of soft machines". In: *Advanced Materials* 27.41 (2015), pp. 6323–6327.
- [159] Debkalpa Goswami et al. "3D-architected soft machines with topologically encoded motion". In: *Advanced Functional Materials* 29.24 (2019), p. 1808713.
- [160] Aniket Pal et al. "Exploiting mechanical instabilities in soft robotics: control, sensing, and actuation". In: *Advanced Materials* 33.19 (2021), p. 2006939.
- [161] Tian Chen et al. "Harnessing bistability for directional propulsion of soft, untethered robots". In: *Proceedings of the National Academy of Sciences* 115.22 (2018), pp. 5698–5702.
- [162] Robert F Shepherd et al. "Multigait soft robot". In: *Proceedings of the national academy of sciences* 108.51 (2011), pp. 20400–20403.
- [163] Xiaoyang Zheng, Xiaofeng Guo, and Ikumu Watanabe. "A mathematically defined 3D auxetic metamaterial with tunable mechanical and conduction properties". In: *Materials & Design* 198 (2021), p. 109313.
- [164] Scott Waitukaitis et al. "Origami multistability: From single vertices to metasheets". In: *Physical review letters* 114.5 (2015), p. 055503.
- [165] Tie Jun Cui et al. "Coding metamaterials, digital metamaterials and programmable metamaterials". In: *Light: science & applications* 3.10 (2014), e218–e218.
- [166] Hai-Feng Zhang et al. "A band enhanced plasma metamaterial absorber based on triangular ring-shaped resonators". In: *IEEE Photonics Journal* 10.4 (2018), pp. 1–10.
- [167] Haifeng Zhang et al. "Design of an ultra-broadband absorber based on plasma metamaterial and lumped resistors". In: *Optical Materials Express* 8.8 (2018), pp. 2103–2113.
- [168] Xin Fang et al. "Programmable gear-based mechanical metamaterials". In: *Nature Materials* (2022), pp. 1–8.
- [169] Bastiaan Florijn, Corentin Coulais, and Martin van Hecke. "Programmable mechanical metamaterials". In: *Physical review letters* 113.17 (2014), p. 175503.
- [170] Yisong Bai et al. "Programmable Mechanical Metamaterials with Tailorable Negative Poisson's Ratio and Arbitrary Thermal Expansion in Multiple Thermal Deformation Modes". In: *ACS Applied Materials & Interfaces* 14.31 (2022), pp. 35905–35916.
- [171] Zhiqiang Meng et al. "Deployable mechanical metamaterials with multistep programmable transformation". In: *Science Advances* 8.23 (2022), eabn5460.
- [172] Corentin Coulais et al. "Combinatorial design of textured mechanical metamaterials". In: *Nature* 535.7613 (2016), pp. 529–532.
- [173] Benjamin Jenett et al. "Discretely assembled mechanical metamaterials". In: *Science advances* 6.47 (2020), eabc9943.
- [174] Aleks Bossart et al. "Oligomodal metamaterials with multifunctional mechanics". In: *Proceedings of the National Academy of Sciences* 118.21 (2021), e2018610118.
- [175] Fei Pan et al. "3D pixel mechanical metamaterials". In: *Advanced Materials* 31.25 (2019), p. 1900548.

- [176] Tian Chen, Mark Pauly, and Pedro M Reis. "A reprogrammable mechanical metamaterial with stable memory". In: *Nature* 589.7842 (2021), pp. 386–390.
- [177] Julie A Jackson et al. "Field responsive mechanical metamaterials". In: *Science advances* 4.12 (2018), eaau6419.
- [178] Shucong Li et al. "Liquid-induced topological transformations of cellular microstructures". In: *Nature* 592.7854 (2021), pp. 386–391.
- [179] Shucong Li et al. "Controlling Liquid Crystal Orientations for Programmable Anisotropic Transformations in Cellular Microstructures". In: *Advanced Materials* 33.42 (2021), p. 2105024.
- [180] Satoshi Ishii et al. "Hybridizing poly (ϵ -caprolactone) and plasmonic titanium nitride nanoparticles for broadband photoresponsive shape memory films". In: *ACS applied materials & interfaces* 8.8 (2016), pp. 5634–5640.
- [181] Zhengtong Han and Kai Wei. "Multi-material topology optimization and additive manufacturing for metamaterials incorporating double negative indexes of Poisson's ratio and thermal expansion". In: *Additive Manufacturing* 54 (2022), p. 102742.
- [182] Abderrezak Bezazi, Fabrizio Scarpa, and Chrystel Remillat. "A novel centresymmetric honeycomb composite structure". In: *Composite Structures* 71.3-4 (2005), pp. 356–364.
- [183] Fuang-Yuan Huang, Biing-Hwa Yan, and Der-Uei Yang. "The effects of material constants on the micropolar elastic honeycomb structure with negative Poisson's ratio using the finite element method". In: *Engineering Computations* (2002).
- [184] Jongmin Shim et al. "Harnessing instabilities for design of soft reconfigurable auxetic/chiral materials". In: *Soft Matter* 9.34 (2013), pp. 8198–8202.
- [185] Andrew Alderson et al. "Elastic constants of 3-, 4- and 6-connected chiral and anti-chiral honeycombs subject to uniaxial in-plane loading". In: *Composites Science and Technology* 70.7 (2010), pp. 1042–1048.
- [186] Andrew Alderson et al. "The in-plane linear elastic constants and out-of-plane bending of 3-coordinated ligament and cylinder-ligament honeycombs". In: *Composites Science and Technology* 70.7 (2010), pp. 1034–1041.
- [187] YJ Chen et al. "Elasticity of anti-tetrachiral anisotropic lattices". In: *International Journal of Solids and Structures* 50.6 (2013), pp. 996–1004.
- [188] Patrick Ziemke et al. "Tailoring the characteristic length scale of 3D chiral mechanical metamaterials". In: *Extreme Mechanics Letters* 32 (2019), p. 100553.
- [189] Xin Ren et al. "A simple auxetic tubular structure with tuneable mechanical properties". In: *Smart Materials and Structures* 25.6 (2016), p. 065012.
- [190] Wenwang Wu et al. "Mechanical design and multifunctional applications of chiral mechanical metamaterials: A review". In: *Materials & design* 180 (2019), p. 107950.
- [191] Tobias Frenzel et al. "Ultrasound experiments on acoustical activity in chiral mechanical metamaterials". In: *Nature communications* 10.1 (2019), pp. 1–6.
- [192] Melanie F Simons et al. "Tiled auxetic cylinders for soft robots". In: *2019 2nd IEEE International Conference on Soft Robotics (RoboSoft)*. IEEE. 2019, pp. 62–67.
- [193] Randall M Erb et al. "Self-shaping composites with programmable bioinspired microstructures". In: *Nature communications* 4.1 (2013), pp. 1–8.

- [194] Corentin Coulais. "As the extension, so the twist". In: *Science* 358.6366 (2017), pp. 994–995.
- [195] Anne Helene Gelebart et al. "A Rewritable, Reprogrammable, Dual Light-Responsive Polymer Actuator". In: *Angewandte Chemie International Edition* 56.43 (2017), pp. 13436–13439.
- [196] *Standard Test Methods for Vulcanized Rubber and Thermoplastic Elastomers—Tension*. Standard. West Conshohocken, Pennsylvania, US: ASTM International, June 2021.
- [197] Pengxuan Fan et al. "Formulation and numerical implementation of tensile shape memory process of shape memory polymers". In: *Polymer* 148 (2018), pp. 370–381.
- [198] Yi-Chao Chen and Dimitris C Lagoudas. "A constitutive theory for shape memory polymers. Part I: large deformations". In: *Journal of the Mechanics and Physics of Solids* 56.5 (2008), pp. 1752–1765.
- [199] Yi-Chao Chen and Dimitris C Lagoudas. "A constitutive theory for shape memory polymers. Part II: a linearized model for small deformations". In: *Journal of the Mechanics and Physics of Solids* 56.5 (2008), pp. 1766–1778.
- [200] Oon H Yeoh. "Some forms of the strain energy function for rubber". In: *Rubber Chemistry and technology* 66.5 (1993), pp. 754–771.
- [201] Haoyu Chu et al. "Measuring the absorption of TiN metallic films using cathodoluminescence of GaN films". In: *Optical Materials Express* 7.4 (2017), pp. 1302–1309.
- [202] Akira Ishimaru. *Wave propagation and scattering in random media*. Vol. 2. Academic press New York, 1978.
- [203] Michael F Modest and Sandip Mazumder. *Radiative heat transfer*. Academic press, 2021.
- [204] Babak Haghpanah et al. "Multistable shape-reconfigurable architected materials". In: *Advanced Materials* 28.36 (2016), pp. 7915–7920.
- [205] Xiaoxing Xia et al. "Electrochemically reconfigurable architected materials". In: *Nature* 573.7773 (2019), pp. 205–213.
- [206] Corentin Coulais, Dimitrios Sounas, and Andrea Alu. "Static non-reciprocity in mechanical metamaterials". In: *Nature* 542.7642 (2017), pp. 461–464.
- [207] JB Berger, HNG Wadley, and RM McMeeking. "Mechanical metamaterials at the theoretical limit of isotropic elastic stiffness". In: *Nature* 543.7646 (2017), pp. 533–537.
- [208] Fernando V Senhora, Emily D Sanders, and Glaucio H Paulino. "Optimally-Tailored Spinodal Architected Materials for Multiscale Design and Manufacturing". In: *Advanced Materials* (2022), p. 2109304.
- [209] Meng-Ting Hsieh, Matthew R Begley, and Lorenzo Valdevit. "Architected implant designs for long bones: Advantages of minimal surface-based topologies". In: *Materials & Design* 207 (2021), p. 109838.
- [210] Mikhail Osanov and James K Guest. "Topology optimization for architected materials design". In: *Annual Review of Materials Research* 46 (2016), pp. 211–233.

- [211] Fengwen Wang. "Systematic design of 3D auxetic lattice materials with programmable Poisson's ratio for finite strains". In: *Journal of the Mechanics and Physics of Solids* 114 (2018), pp. 303–318.
- [212] Evangelos Daskalakis et al. "Bone Bricks: The Effect of Architecture and Material Composition on the Mechanical and Biological Performance of Bone Scaffolds". In: *ACS omega* 7.9 (2022), pp. 7515–7530.
- [213] Maria I Echeverria Molina, Katerina G Malollari, and Kyriakos Komvopoulos. "Design challenges in polymeric scaffolds for tissue engineering". In: *Frontiers in Bioengineering and Biotechnology* (2021), p. 231.
- [214] Chunping Ma et al. "Accelerated design and characterization of non-uniform cellular materials via a machine-learning based framework". In: *npj Computational Materials* 6.1 (2020), pp. 1–8.
- [215] Baekjun Kim, Sangwon Lee, and Jihan Kim. "Inverse design of porous materials using artificial neural networks". In: *Science advances* 6.1 (2020), eaax9324.
- [216] Yunwei Mao, Qi He, and Xuanhe Zhao. "Designing complex architected materials with generative adversarial networks". In: *Science advances* 6.17 (2020), eaaz4169.
- [217] Jackson K Wilt, Charles Yang, and Grace X Gu. "Accelerating auxetic metamaterial design with deep learning". In: *Advanced Engineering Materials* 22.5 (2020), p. 1901266.
- [218] Jiaqi Jiang, Mingkun Chen, and Jonathan A Fan. "Deep neural networks for the evaluation and design of photonic devices". In: *Nature Reviews Materials* 6.8 (2021), pp. 679–700.
- [219] Sang Ye et al. "Deep neural network method for predicting the mechanical properties of composites". In: *Applied Physics Letters* 115.16 (2019), p. 161901.
- [220] Jinbo Pan et al. "Auxetic two-dimensional transition metal selenides and halides". In: *npj Computational Materials* 6.1 (2020), pp. 1–6.
- [221] Akinori Yamanaka et al. "Deep neural network approach to estimate biaxial stress-strain curves of sheet metals". In: *Materials & Design* 195 (2020), p. 108970.
- [222] Kohta Koenuma et al. "Estimation of texture-dependent stress-strain curve and r-value of aluminum alloy sheet using deep learning". In: *Materials Transactions* 61.12 (2020), pp. 2276–2283.
- [223] Gabriele M Coli et al. "Inverse design of soft materials via a deep learning-based evolutionary strategy". In: *Science advances* 8.3 (2022), eabj6731.
- [224] Jan-Hendrik Bastek et al. "Inverting the structure–property map of truss metamaterials by deep learning". In: *Proceedings of the National Academy of Sciences* 119.1 (2022), e2111505119.
- [225] Liwei Wang et al. "Deep generative modeling for mechanistic-based learning and design of metamaterial systems". In: *Computer Methods in Applied Mechanics and Engineering* 372 (2020), p. 113377.
- [226] Zihan Wang et al. "Design of Phononic Bandgap Metamaterials Based on Gaussian Mixture Beta Variational Autoencoder and Iterative Model Updating". In: *Journal of Mechanical Design* 144.4 (2022), p. 041705.
- [227] Nikolaos Karathanasopoulos and Dimitrios C Rodopoulos. "Enhanced Cellular Materials through Multiscale, Variable-Section Inner Designs: Mechanical Attributes and Neural Network Modeling". In: *Materials* 15.10 (2022), p. 3581.

- [228] Tero Karras, Samuli Laine, and Timo Aila. "A style-based generator architecture for generative adversarial networks". In: *Proceedings of the IEEE/CVF conference on computer vision and pattern recognition*. 2019, pp. 4401–4410.
- [229] Phillip Isola et al. "Image-to-image translation with conditional adversarial networks". In: *Proceedings of the IEEE conference on computer vision and pattern recognition*. 2017, pp. 1125–1134.
- [230] Ian Goodfellow et al. "Generative adversarial networks". In: *Communications of the ACM* 63.11 (2020), pp. 139–144.
- [231] Minhyeok Lee and Junhee Seok. "Controllable generative adversarial network". In: *Ieee Access* 7 (2019), pp. 28158–28169.
- [232] Jiajun Wu et al. "Learning a probabilistic latent space of object shapes via 3d generative-adversarial modeling". In: *Advances in neural information processing systems* 29 (2016).
- [233] Fausto Milletari, Nassir Navab, and Seyed-Ahmad Ahmadi. "V-net: Fully convolutional neural networks for volumetric medical image segmentation". In: *2016 fourth international conference on 3D vision (3DV)*. IEEE. 2016, pp. 565–571.
- [234] Toby J Mitchell. "An algorithm for the construction of "D-optimal" experimental designs". In: *Technometrics* 42.1 (2000), pp. 48–54.
- [235] Dong Li, Liang Dong, and Roderic S Lakes. "The properties of copper foams with negative Poisson's ratio via resonant ultrasound spectroscopy". In: *physica status solidi (b)* 250.10 (2013), pp. 1983–1987.
- [236] George Merrill Chaikin. "An algorithm for high-speed curve generation". In: *Computer graphics and image processing* 3.4 (1974), pp. 346–349.
- [237] Dewen Li et al. "Bioinspired multifunctional cellular plastics with a negative Poisson's ratio for high energy dissipation". In: *Advanced Materials* 32.33 (2020), p. 2001222.
- [238] Chan Soo Ha, Michael E Plesha, and Roderic S Lakes. "Chiral three-dimensional isotropic lattices with negative Poisson's ratio". In: *physica status solidi (b)* 253.7 (2016), pp. 1243–1251.
- [239] Tiantian Li et al. "Exploiting negative Poisson's ratio to design 3D-printed composites with enhanced mechanical properties". In: *Materials & design* 142 (2018), pp. 247–258.
- [240] Xiaoyang Zheng et al. "Reprogrammable flexible mechanical metamaterials". In: *Applied Materials Today* 29 (2022), p. 101662.
- [241] Kenneth A Hart and Julian J Rimoli. "MicroStructPy: A statistical microstructure mesh generator in Python". In: *SoftwareX* 12 (2020), p. 100595.
- [242] Konstantinos-Iason Ypsilantis, George Kazakis, and Nikos D Lagaros. "An efficient 3D homogenization-based topology optimization methodology". In: *Computational Mechanics* 67.2 (2021), pp. 481–496.
- [243] Anders Clausen et al. "Topology optimized architectures with programmable Poisson's ratio over large deformations". In: *Adv. Mater* 27.37 (2015), pp. 5523–5527.
- [244] Ikumu Watanabe et al. "Maximization of strengthening effect of microscopic morphology in duplex steels". In: *Advanced Structured Materials: From Creep Damage Mechanics to Homogenization Methods*. Ed. by Holm Altembach, Tetsuya Matsuda, and Dai Okumura. Cham: Springer International Publishing, 2015. Chap. 24, pp. 541–555.

- [245] Indranath Mitra et al. "3D Printing in alloy design to improve biocompatibility in metallic implants". In: *Materials Today* 45 (2021), pp. 20–34.
- [246] Gerry L Koons, Mani Diba, and Antonios G Mikos. "Materials design for bone-tissue engineering". In: *Nature Reviews Materials* 5.8 (2020), pp. 584–603.
- [247] Vladimir Egorov and Colm O'Dwyer. "Architected porous metals in electrochemical energy storage". In: *Current Opinion in Electrochemistry* 21 (2020), pp. 201–208. ISSN: 2451-9103.
- [248] JG Werner et al. "Block copolymer derived 3D interpenetrating multifunctional gyroidal nanohybrids for electrical energy storage". In: *Energy & Environmental Science* 11.5 (2018), pp. 1261–1270.
- [249] Lorna J. Gibson and Michael F. Ashby. *Cellular Solids: Structure and Properties*. 2nd ed. Cambridge Solid State Science Series. Cambridge University Press, 1997.
- [250] Zachary Zguris. "How mechanical properties of stereolithography 3D prints are affected by UV curing". In: *Formlabs White Paper* (2016), pp. 1–11.
- [251] Hiromi Yasuda et al. "Mechanical computing". In: *Nature* 598.7879 (2021), pp. 39–48.
- [252] Yuanping Song et al. "Additively manufacturable micro-mechanical logic gates". In: *Nature communications* 10.1 (2019), pp. 1–6.
- [253] Hang Zhang et al. "Hierarchical mechanical metamaterials built with scalable tristable elements for ternary logic operation and amplitude modulation". In: *Science Advances* 7.9 (2021), eabf1966.
- [254] Yijie Jiang, Lucia M Korpas, and Jordan R Raney. "Bifurcation-based embodied logic and autonomous actuation". In: *Nature communications* 10.1 (2019), pp. 1–10.
- [255] Charles El Helou et al. "Digital logic gates in soft, conductive mechanical metamaterials". In: *Nature communications* 12.1 (2021), pp. 1–8.
- [256] Daniel J Preston et al. "Digital logic for soft devices". In: *Proceedings of the National Academy of Sciences* 116.16 (2019), pp. 7750–7759.
- [257] Nima Dehmamy, Soodabeh Milanlouei, and Albert-László Barabási. "A structural transition in physical networks". In: *Nature* 563.7733 (2018), pp. 676–680.
- [258] Laurie C Doering. *Protocols for neural cell culture*. Vol. 20. Springer, 2010.
- [259] Johnny Moughames et al. "Three-dimensional waveguide interconnects for scalable integration of photonic neural networks". In: *Optica* 7.6 (2020), pp. 640–646.
- [260] Miklós Hetényi and Miklós Imre Hetbenyi. *Beams on elastic foundation: theory with applications in the fields of civil and mechanical engineering*. Vol. 16. University of Michigan press Ann Arbor, MI, 1946.
- [261] Bikramjit Mukherjee and David A Dillard. "On buckling of a thin plate on an elastomeric foundation". In: *International Journal of Mechanical Sciences* 149 (2018), pp. 429–435.
- [262] L Zhang, GT Wu, and J Wu. "A Kerr-type elastic foundation model for the buckling analysis of a beam bonded on an elastic layer". In: *ZAMM-Journal of Applied Mathematics and Mechanics/Zeitschrift für Angewandte Mathematik und Mechanik* 99.10 (2019), e201900162.

-
- [263] Tim Salimans et al. “Improved techniques for training gans”. In: *Advances in neural information processing systems* 29 (2016).
- [264] Martín Abadi et al. “TensorFlow: a system for Large-Scale machine learning”. In: *12th USENIX symposium on operating systems design and implementation (OSDI 16)*. 2016, pp. 265–283.